Dipl.-Ing. Stojan Vujić

Microstructural investigation of 25Cr-20Ni-Nb-N austenitic steel for USC and A-USC coal power plants

DISSERTATION

Submitted for the Degree of

Doctor of Technical Science

Graz University of Technology

Supervisor

Univ.-Prof. Dipl.-Ing. Dr. techn. Christof Sommitsch

Institute of Material Science and Welding

Faculty of Mechanical Engineering and Economic Sciences

Graz, November 2015

AFFIDAVIT

I declare that I have authored this thesis independently, that I have not used other than the declared sources/resources, and that I have explicitly indicated all material which has been quoted either literally or by content from the sources used. The text document uploaded to TUGRAZonline is identical to the present doctoral dissertation.

______________________________ ______________________________

Datum / Date Signature

PREFACE

This dissertation has been carried out at the Institute of Material Science and Welding and has been submitted for the degree of Doctor of Technical Science at the Faculty of Mechanical Engineering at the Graz University of Technology. The research described in this thesis has been conducted under the supervision of Prof. Christof Sommitsch and Dr. Coline Béal from the Institute of Material Science and Welding, Graz University of Technology, between March 2011 and November 2015.

The financial support for this thesis is provided by the European Union within the project MACPLUS (Material-Component Performance-driven Solutions for Long-Term Efficiency Increase in Ultra Supercritical Power Plants) in the framework of the Clean Coal Technologies. A part of this dissertation is carried out at the Department of Materials Science and Engineering at the Royal Institute of Technology (KTH) in Stockholm.

Results obtained during this PhD in the field of austenitic steels and nickel-based alloys have been published in journals and conference proceedings. The references of these publications are shown below.

1) S. Vujic, R. Sandström, and C. Sommitsch, "Precipitation evolution and creep strength modelling of 25Cr20NiNbN austenitic steel," Mater. High Temp., DOI: 10.1179/1878641315Y.0000000007, pp. 1–12, 2015, in print.

2) E. Plesiutschnig, S. Vujic, and C. Sommitsch, "Investigations on the precipitation evolution of MarBN steels for microstructure based Life-Time assessments," Sapporo, Japan, in Proc.: Advanced High-Temperature Materials Technology for Sustainable and Reliable Power Engineering (123HIMAT), 2015.

3) S. Vujic, F. Di Martino, S. Matera, O. Tassa, S. C. Hogg, J. Zurek, C. Beal, and C. Sommitsch, "Microstructure Evolution and Precipitation Modeling in Ni-Based Alloy C-263," Las Vegas, USA, in Proc.: Processing & Manufacturing of Advanced Materials (THERMEC), 2013, vol. 783–786.

4) S. F. Di Martino, R. G. Faulkner, S. C. Hogg, S. Vujic, and O. Tassa, “Characterisation of microstructure and creep properties of alloy 617 for high-temperature applications,” Mater. Sci. Eng. A, vol. 619, pp. 77–86, 2014.

5) S. Vujic, C. Beal, C. Sommitsch, F. Muhammad, R. Sandström, and J. Zurek, “Modelling and optimizing precipitation in creep resistant austenitic steel 25Cr-20Ni-Nb-N,” Waikoloa, Hawaii, in Proc.: Advances in Materials Technology for Fossil Power Plants, 2013.

6) E. Povoden-Karadeniz, S. Vujic, and E. Kozeschnik, “Thermodynamic modeling and simulation of time-temperature-precipitation diagrams in stainless steel,” San Sebastian, Spain, in Proc.: CALPHAD XLII, 2013.

7) S. Vujic, M. Farooq, B. Sonderegger, R. Sandström, and C. Sommitsch, “Numerical Modelling and Validation of Precipitation Kinetics in Advanced Creep Resistant Austenitic Steel,” Comput. METHODS Mater. Sci., vol. 12, no. 3, pp. 175–182, 2012.

Stojan Vujić

November 2015

ACKNOWLEDGEMENTS

This thesis has been carried out within the EU-project MACPLUS. Therefore, many thanks to the European Union which provided the financial support.

I would like to thank Prof. Christof Sommitsch for acting as reviewer of this dissertation, for supervising this thesis and who gave me the chance to visit numerous of conferences and project meetings around the world. It was a great experience for me! Vielen Dank! I want to express many thanks to Dr. Coline Béal who supervised this thesis. Merci beaucoup! Further thanks goes to my colleagues from the Institute of Material Science and Welding at the TU Graz. Special thanks to Christian, Johannes, Ozan, Ernst, Claudia, and Coline from the Material Development group. Vielen Dank!

Many thanks are owned to Prof. Rolf Sandström who performs the creep strength calculations in the present thesis and for the invitation to the KTH Stockholm as well as for the grateful work which is done at the KTH. It was an interesting time in Sweden. Tack så mycket! I would like to thank Forschungszentrum Jülich and KTH Stockholm for providing the samples and for performing the SEM and TEM investigations.

I would like to thank Prof. Ernst Kozeschnik from TU Vienna for acting as reviewer of this dissertation and for the grateful support of MatCalc. Vielen Dank! A special thanks goes to Dr. Erwin Povoden Karadeniz from TU Vienna who spent a lot of time for numerous interesting discussions, MatCalc support and database development. Vielen Dank!

Last but not least, I would like to thank my spouse Jelena, my parents Ljiljana and Dragoljub as well as my friends for their huge support during my time as a PhD student. Mnogo vam hvala!

ABSTRACT

Advanced austenitic steels, such as 25Cr-20Ni-Nb-N are complex systems which have more than eight alloying elements. They provide high corrosion resistance and have high creep strength, which make them suitable for superheater applications in power plants.

The present thesis deals with the investigation of microstructure, especially precipitation evolution in an advanced 25Cr-20Ni-Nb-N austenitic steel after solution annealing and thermal ageing. The investigations are carried out by light optical microscopy, scanning electron microscopy, as well as transmission electron microscopy. The investigations reveal the presence of five different precipitates: σ-phase, $M_{23}C_6$, Nb(C,N), η ($Cr_3Ni_2Si(C,N)$), and Z-phase. The fraction of σ-phase is found to increase rapidly with increasing ageing time.

The investigations are expanded by additional equilibrium-, Scheil- and precipitation-kinetics-calculations using the software MatCalc. Thereby, the amount and evolution of primary as well as secondary precipitates during a solution annealing and isothermal ageing for 100,000h at 650 and 750°C have been calculated. Good agreement with experimental investigation has been achieved.

Further on, the results of the precipitation evolution calculations are used for the modelling of the creep strength. In total, three main contributions to the creep strength are considered: from dislocations, from precipitates and from elements in solid solution. The contribution from the dislocation is found to be the highest one.

Using the results of precipitation evolution calculation and creep strength modelling, a modified chemical composition has been proposed, with the purpose of suppressing the σ-phase precipitation.

Superheater tubes out of the modified composition are manufactured and short-term creep tests as well as ageing treatments are performed. As expected, analyses of tested specimens reveal no σ-phase precipitates.

Finally, this thesis presents a whole material development process, which contains an investigation of a conventional 25Cr-20Ni-Nb-N austenitic steel, calculation of precipitation evolution and creep strength, modification of chemical composition and manufacturing of modified superheater tubes for power plants.

Symbols and Units

a	m	Lattice parameter
A	m^2	Area surrounding the dislocation
b	m	Burger's vector (=2.58E-10)
c_i^0	m^{-3}	Concentration of solute i in solid solution
c_i^{dyn}	m^{-3}	Concentration of solute i around moving dislocations
c_i^{stat}	m^{-3}	Concentration of solute i around non-moving (static) dislocations
c_{ki}	mol m^{-3}	Concentration of component i
D_i^{sol}	m^2 s^{-1}	Diffusion coefficient for the solute i
D_{ki}	m^2 s^{-1}	Diffusion coefficient
D_{S0}	m^2 s^{-1}	Coefficient for self diffusion
d_{sub}	m	Subgrain diameter
F	N	Force
f_{sol}	-	Creep rate factor
f_{vol}	-	Volume fraction of particles
G	N m^{-2}	Shear modulus
G*	J	Critical nucleation energy
$I(z_0)$	-	Drag stress function
J_{ki}	mol m^{-2} s^{-1}	Flux coefficient
J	s^{-1}	Transient nucleation rate
K	-	Constant (=20 for austenitic steels)
k_B	kg m^2 s^{-2} K^{-1}	Boltzmann's constant (=1.3806488 × 10^{-23})
L	m	Spurt distance
L_{part}	m	Average distance between the particles
$L_{part\ tot}$	m	Total interparticle spacing
L_{rcrit}	m	Interparticle spacing of particles larger than critical radius
m	-	Taylor factor (=3.06)
M	m^2 N^{-1} s^{-1}	Dislocation mobility
M_{climb}	m^2 N^{-1} s^{-1}	Dislocation mobility for dislocation climb
M_k	m^3 N^{-1} s^{-1}	Interface mobility
N_A	m^{-2}	Total number of particles per unit area
N_o	-	Number of potential nucleation sites
N_{oi}	mol	Number of moles of component i
$n_A(r)$	m^{-2}	Number of particles larger than radius r
$n_A(r_{crit})$	m^{-2}	Number of particles larger than critical radius
Q	J	Activation energy
Q_1	J s^{-1}	Dissipation rate by interface movement
Q_2	J s^{-1}	Dissipation rate by diffusion inside the precipitate
Q_3	J s^{-1}	Dissipation rate by diffusion inside the matrix
R	J K^{-1} mol^{-1}	Gas constant (=8.31)
r	m	Particle radius
r_{crit}	m	Critical particle radius for dislocation climb
r_{sol}	m	Distance from the solute to the centre of the dislocation
T	K	Temperature
t	s	Time
t_{climb}	s	Time for climb

U_i	J	Interaction energy between a solute and an edge dislocation
U_i^{max}	J mol^{-1}	Maximum interaction energy between a solute and an edge dislocation
y	m	y-coordinate of solute relative to an edge dislocation
z_0	-	Drag stress parameter
Z	-	Zeldovich factor
α	-	Constant ($\alpha=(1-\nu/2)/2\pi(1-\nu)$ where Poisson’s ratio $\nu=0.3$)
β	J m	Drag stress parameter ($=2/3*U_{max}*b$)
β^*	s^{-1}	Atomic attachment rate
γ_k	J m^{-2}	Precipitate/matrix interface energy
ε	%	Strain
ε_i	-	Linear atomic size misfit parameter of solute i
$\dot{\varepsilon}$	s^{-1}	Creep rate
$\dot{\varepsilon}_{min}$	s^{-1}	Creep rate during stationary creep
λ_k	J m^{-3}	Contribution of the elastic energy and plastic work
μ_{0i}	J mol^{-1}	Chemical potential
ν	-	Poisson’s ratio (=0.3)
ν_{disl}	m s^{-1}	Climb velocity
ρ	m^{-2}	Dislocation density
ρ_K	m	Radius of the precipitate with index k
$\dot{\rho}_k$	m s^{-1}	Growth rate of precipitate k
σ	N m^{-2}	Stress
σ_{break}	N m^{-2}	Break stress
σ_{disl}	N m^{-2}	Dislocation stress
σ_{disl}	N m^{-2}	Dislocation hardening
σ_i^{drag}	N m^{-2}	Drag stress from solute i
σ_{max}	N m^{-2}	Maximum strength (tensile strength)
σ_{part}	N m^{-2}	Orowan strength
$\sigma_{part\ tot}$	N m^{-2}	Total orowan strength of all particles
σ_{ph}	N m^{-2}	Particle hardening
σ_{sol}	N m^{-2}	Solid solution hardening
σ_{solN}	N m^{-2}	Solid solution hardening by N
τ_L	N	Dislocation line tension
τ_i	s	Incubation time
υ	m s^{-1}	Velocity of the dislocation
Ω_0	m^3 mol^{-1}	Atomic volume in the host alloy

Abbreviations

USC	Ultra-Supercritical
A-USC	Advanced Ultra-Supercritical
TCP	Topologically Closed Packed
LOM	Light Optical Microscopy
SEM	Scanning Electron Microscopy
TEM	Transmission Electron Microscopy
EDS	Energy Dispersive Spectroscopy
TED	Transmission Electron diffraction
SAED	Selected Area Electron Diffraction
AISI	American Iron and Steel Institute
VIM	Vacuum Induction Melting
BSD	Back-Scatter Detector
ASTM	American Society for Testing and Materials
METI	Ministry of Economy, Trade and Industry

Content

1 Introduction

The primary energy sources for world electricity generation are coal (41%), gas (22%), hydro (16%), nuclear (12%), oil (5%), and renewable (4%)[1]. The world electricity demand has doubled between 1990 and 2011 and it is expected to increase up to the year 2035 between 1.7 and 2.5% per year[1]. One possible way to meet this increasing demand is to increase the efficiency of the present and future coal power plants.

The coal power plants are generally classified into three categories: Supercritical (SC), Ultra-supercritical (USC) and advanced ultra-supercritical (A-USC). SC power plants operate with steam temperature up to 590°C and steam pressure of 250 bar, the USC with 590-620°C and 250 bar, and the A-USC with 700-760°C and 345bar [2]. The world mean efficiency of coal power plants is approximately 36% [1]. This efficiency is achieved by steam temperature lower than 600°C. An increase of the steam temperature to 700-750°C would increase the efficiency up to 50% or more and correspondingly lead to a drop in CO_2 emissions that is of utmost importance to reduce global warming [3]. Such conditions require materials with enhanced toughness, creep strength and corrosion resistance. Potential materials for these conditions are ferritic-, austenitic-steels and nickel-base alloys. Considering the fireside corrosion, the ferritic steels are used up to 620°C and it is expected that in the future these steels will be used up to 650°C [4]. Above these temperatures, the austenitic steels and nickel base alloys have to be used. The main brake in the use of the nickel-base alloys is, that they are three times more expensive compared to the austenitic steels. Therefore, the austenitic steels are an optional choice for power plant applications above 650°C.

In general, the austenitic steels for power plant applications can be split up into four categories according to their chromium content: <18% Cr, 18% Cr, 20-25% Cr and >25% Cr. For USC and A-USC power plants, the high chromium (20-25% Cr and >25% Cr) austenitic steels are more suitable because of their higher corrosion resistance. However, they are more sensitive to sigma phase precipitation [5], [6], which can cause a loss of toughness [7]–[9] and further on to material failure.

The challenge in developing advanced austenitic steels is to provide high corrosion resistance (by high chromium content) and high creep strength but to avoid undesirable phases such as sigma phase. This thesis deals with the microstructure evolution under manufacturing route and service conditions of a high chromium (25%Cr) austenitic steel. Experimental investigations as well as modelling of precipitation and evaluation of hardening mechanisms have been carried out. Finally, superheater tubes with modified composition are produced where σ-phase formation is suppressed.

2 Objectives

The main goal of this thesis is to investigate and describe the microstructure evolution of a 25Cr-20Ni-Nb-N austenitic steel at 650 and 750°C in order to develop a new steel with optimised microstructure. Therefore, the thesis has been divided into three sections: (i) experimental microstructure investigations, (ii) modelling of microstructure evolution and hardening mechanisms and (iii) evaluation as well as investigation of the modified composition.

The main objective of the first section (i) is to experimentally investigate the precipitation evolution at 650 and 750°C in the 25Cr-20Ni-Nb-N austenitic steel. For the investigation, LOM, SEM, TEM and EDS techniques should be used. The microstructure and especially the precipitation evolution (e.g. precipitates -size, -fraction, -shape etc.) should be investigated and compared with the literature.

The main objective of the second part (ii) is the modelling of the precipitation evolution in the 25Cr-20Ni-Nb-N austenitic steel at 650 and 750°C. In this section, the phase fraction and mean radius evolution of the different precipitates at 650 and 750°C should be predicted by using the thermo-kinetic software MatCalc [10]–[12]. Using the results of the thermo-kinetic simulations by MatCalc and the creep strength modelling approach of Sandström et al. [13]–[18] the hardening mechanisms should be evaluated. The terms and objectives for the modification of the chemical composition of the 25Cr-20Ni-Nb-N steel should be defined in order to obtain the best mechanical properties. Afterwards additional thermo-kinetic calculation should be applied to define a modified composition for the 25Cr-20Ni-Nb-N austenitic steel.

The main objective of the third part (iii) is the microstructure investigation by LOM and SEM of the modified composition of the 25Cr-20Ni-Nb-N austenitic steel. Finally, the results should be discussed in regards to the defined objectives.

3 Literature Review

This chapter will give an overview of the application of austenitic steels for USC and A-USC power plants. After a short introduction about superheater operation and materials for superheater/reheater in power plants, the microstructure of the 25Cr-20Ni-Nb-N austenitic steel with emphasis on the precipitation evolution as well as creep strength will be discussed.

3.1 Superheater and Reheater in Power Plants

Thermal power station are mainly steam driven: the steam turns into a steam turbine which drives a generator, which then produces electrical energy.

The water in the power plant has to pass several stages until the steam is generated. A general overview of the steam flow and selected materials in an A-USC power plant is shown in Figure 1. First, the water is heated up in the feed heaters, by extracting small amounts of hot steam out of the turbine. Afterwards, the heated water passes the economizer and evaporator where the water is brought to the temperature of boiling and evaporation. Before the steam is brought to the turbine, it is heated up by the superheater, where the moisture content of the steam is removed [19] and the final steam service temperature is achieved. After the steam is leaving the turbine, it is reheated by the reheater and fed back to the turbine. A double reheating process in an A-USC power plant increases the efficiency by +0.7% [20]. The last stages of the steam flow are the condenser and boiler feed where the steam is condensed and pumped back to the boiler.

The superheater and reheater are located in the flue gas duct, after the furnace, and are made of a set of tubes (placed across the duct) to pick up the heat. The diameter of the seamless tubes is about 45mm and the thickness is about 10mm. Starr [21] reports that the superheater “coil” is not continuous, it consists of several banks which varies from plant to plant. Generally, a typical superheater consists of three banks: the primary, secondary and final superheaters. For advanced power plants more than three superheater banks are necessary. A-USC power plant which operates at a steam temperature of ≈700°C contains four superheater banks, as can be seen in Figure 1 (superheaters are marked with "SH"). The steam temperature of the primary superheater (1SH) is quite low, around 350-450°C. This primary superheater is made of ferritic steels. The secondary superheater (2SH, 3SH) takes the steam from the primary one which is located close to the exit of the furnace, directly receiving the hot flue gases which are in the range of 1250-1550°C. These secondary superheaters are made of austenitic and nickel-base alloys. The final superheater (4SH) brings the steam to the turbine inlet steam condition, which is for the A-USC, 700°C and 35MPa, see Figure 1. This final superheater is made of nickel-base alloys. The steam pressure in the reheater is clearly lower compared to the superheater: for SC power plant the relationship superheater/reheater is 250/45 bar, for USC 250/50 and for A-USC it is 345/76 bar [2].

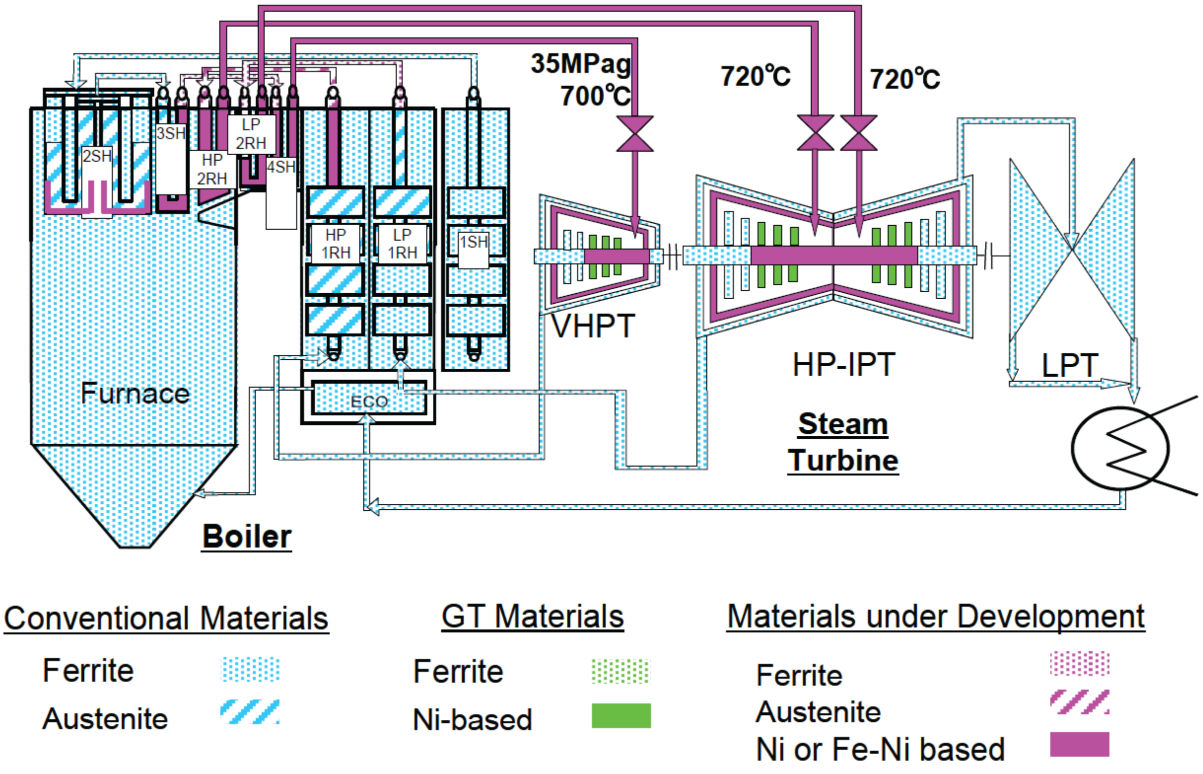

Figure 1: Main stages of the steam flow of a A-USC power plant and selected materials [22]. VHPT: Very high pressure turbine; HP-IPT: High pressure-intermediate pressure turbine; LPT: Low pressure turbine; SH: Super heater; RH: Reheater; GT: Gas turbine; ECO: Economizer.

3.2 Austenitic steels for Superheater and Reheater

During the last decades many materials for superheater and reheater in coal power plants have been developed. In general the materials can be split up into three groups: ferritic-, austenitic-steels and nickel-base alloys, as shown in Figure 1. Superheater materials for USC and A-USC power plants require a high creep strength, high thermal fatigue strength, good weldability, high resistance to fireside corrosion and steam side oxidation. Viswanathan et al. [4] mention that from creep strength point of view the ferritic steels can be used up to a metal temperature of 620°C (corresponds to a steam temperature of 592°C). Furthermore, considering the fireside corrosion, the metal temperature is still limited to 593°C. However, it is expected that the ferritic steels in future will be used up to 650°C [23]. Above these temperatures, in the finishing stage of superheater and reheater tubing, austenitic steels and nickel-base alloys have to be used.

Wheeldon et al. [2] mention that the current advanced austenitic steels have the required creep strength for more than 650°C, but they have two physical challenges:

- Low conductivity and high thermal expansion may lead to high thermal stresses and fatigue cracking in the thick-walled pipe sections.
- Iron-alkali sulfates, which are present in the coal-ash deposits, promote the fireside corrosion. The corrosion attack increases with increasing temperature (up to 700°C) and increasing coal chlorine content. Above of 540°C the alkali sulfate becomes molten and attacks the tube. The corrosion attack reaches a maximum at 700°C and decreases for higher temperatures [9]. Since the austenitic steels are operating in this temperature range, a strong corrosion attack is expected.

In general the austenitic steels can be split up into four categories according to their Cr content: <18% Cr, 18% Cr, 20-25% Cr and >25% Cr. The 25Cr-20Ni-Nb-N steel (also known as TP310HNbN, HR3C, DMV310N), which is investigated in this thesis, is an advancement of the 20Cr-20Ni (AISI 310) steel with additional amount of Nb and N, as can be seen in Figure 2.

The chemical composition of the 25Cr-20Ni-Nb-N austenitic steel is presented in Table 1. The high chromium-content of 25% gives an excellent fireside corrosion resistance, while the addition of niobium and nitrogen promotes both, the formation of fine NbCrN (Z-phase) precipitates and solid solution hardening improving the creep strength. The nickel content of 20% provides a full austenite matrix within the whole temperature range. The carbon is an important carbide former. Silicon improves the oxidation resistance. Manganese acts as deoxidation element and absorbs the sulphur during manufacturing.

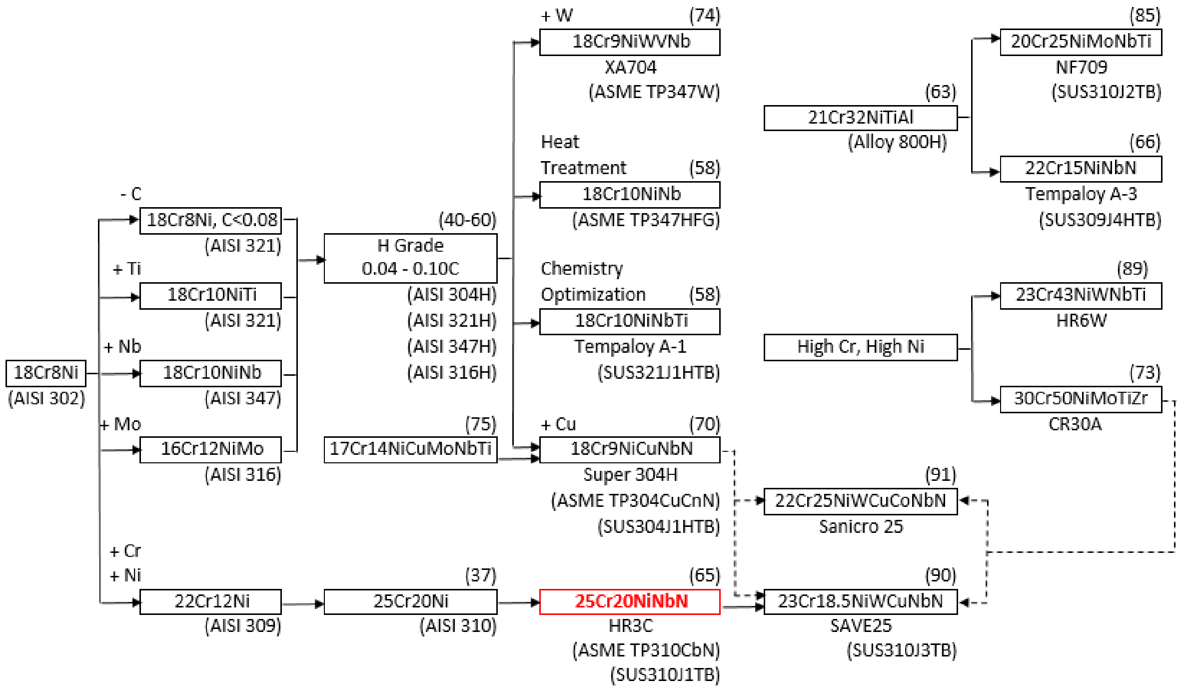

( ) designates 10^5h Creep Rupture Strength (MPa) at 700°C

Figure 2: Development progress of austenitic steels for boiler [23].

Table 1: Chemical composition (wt.%) of 25Cr-20Ni-Nb-N by the standards [24].

Designation	C	Cr	Si	P	Ni	Nb	Mn	N	S
METI	≤	23.0	≤	≤	17.0	0.20	≤	0.15	≤
KASUS310J1TB	0.10	27.0	1.50	0.03	23.0	0.60	2.00	0.35	0.03
ASTM	0.04	24.0	≤	≤	17.0	0.20	≤	0.15	≤
TP310HCbN	0.10	26.0	0.75	0.03	23.0	0.60	2.00	0.35	0.03
EN	≤	23.0	≤	≤	17.0	0.20	≤	0.15	≤
TP310HCbN	0.10	27.0	1.50	0.03	23.0	0.60	2.00	0.35	0.03

Generally the tubes can be produced by mill-rolling or by extrusion. The last one is applied for stainless steels and special metal tubes [25]. The ingot for the extrusion process is usually produced by vacuum induction melting (VIM). The VIM produced ingot is then hot forged at a temperature above 1000°C, whereas the temperature is decreasing during the forging to 800-900°C. Afterwards, the semi-finished product is machined to the desired dimensions for further extrusion process. Before extrusion, the semi-finished product is heated up by induction heating and piercing is applied, where a hole in the part is created, as presented in Figure 3. After that the tube is manufactured by extruding, followed by straightening, cold pilgering (or cold drawing) and final heat treatment (usually a solution treatment at around 1200°C for the 25Cr-20Ni-Nb-N steel). Before the tubes are shipped to the customer, a non-destructive testing (NDT) of the tubes is performed.

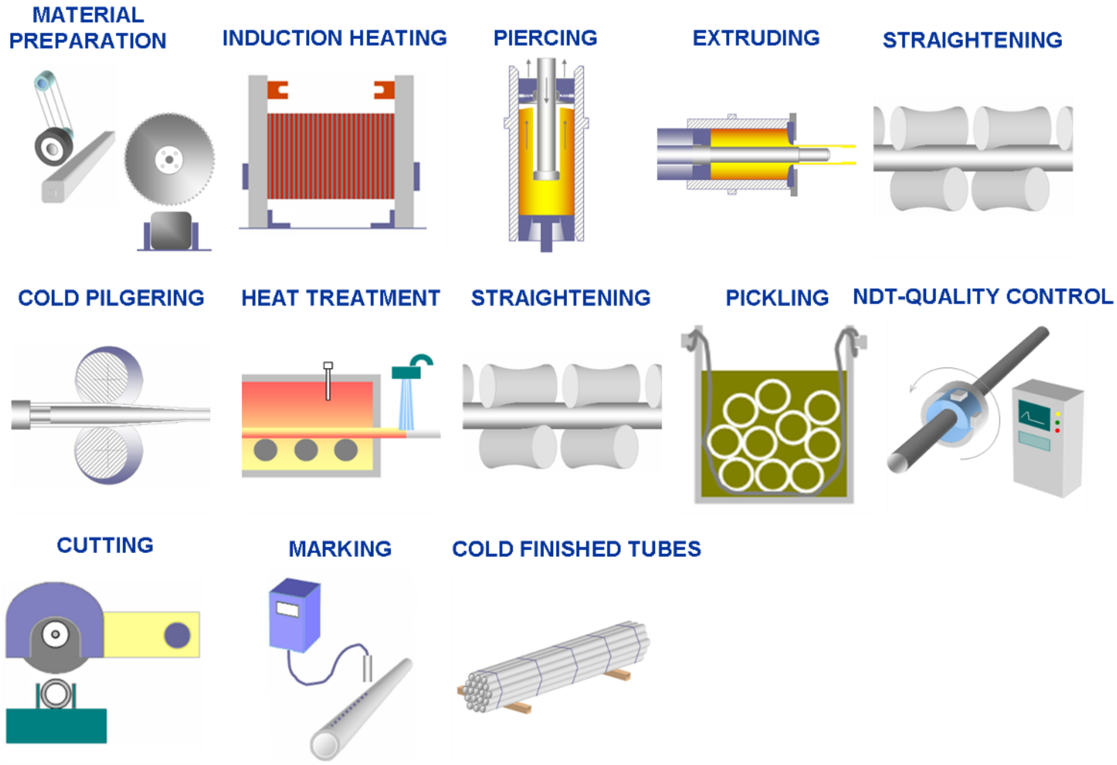

Figure 3: Manufactoring process of cold finished superheater tubes [26].

3.2.1 Precipitates in 25Cr-20Ni-Nb-N austenitic steel

Newest austenitic steels e.g. HR3C or Sanicro25 contain usually a lot of alloying elements (as shown in Table 1) in order to get the required properties. Since these properties are dependent on the microstructure stability, such as formation, dissolution and coarsening of precipitates, it is important to properly describe the evolution of the microstructure during thermo-mechanical processes and subsequent in service condition.

Different input parameters and experimental values are necessary for precipitation evolution simulations. Typical input parameters are precipitation nucleation-sites and shape-factors. Experimentally observed values are precipitates phase fractions and mean diameters. In order to obtain these parameters and values, extensive experimental investigations are necessary which are cost and time consuming. Thus, a literature review about the precipitates forming in the 25Cr-20Ni-Nb-N steel (mainly based on [27]) is described here. The present chapter explains the main precipitates characteristics such as precipitates structure, composition, shape, nucleation-site, stability and precipitates effects on the mechanical properties in austenitic steels. At the end of each chapter a table is presented which summarizes the main precipitates characteristics related to the 25Cr-20Ni-Nb-N austenitic steel.

3.2.1.1 MX

In [27] it is reported that MX precipitates form when carbide/nitride formers (Ti, Nb, V, Zr, Ta etc.) are added to the alloy. Further on, MX precipitates have two purposes. The first one is to stabilize the alloy against intergranular corrosion: MC precipitates bind the carbon and therefore supress the precipitation of chromium-rich precipitates such $M_{23}C_6$ leading to local depletion of chromium. The second one is to enhance the creep resistance, after a solution treatment of 30-60min between 1100 and 1250°C, MX will precipitate during creep and act as obstacles against movement of dislocations.

Generally the MX precipitates form during high temperature exposure (heat treatment as well as service conditions) on twin and grain boundaries, dislocations within the matrix and on stacking faults [27]. Formation of MX during the solidification is also possible, as reported in [28] where TiN, NbN and (Nb,Ti)C precipitates with a size between 1 and 5µm in a 20Cr-20Ni austenitic steel are found. It is assumed that these several micrometer large MX precipitates are detrimental. In [29], [30] it is reported that MX precipitates having a size of ≈3µm act as void initiation and can decrease significantly the fracture resistance in type 347 austenitic steel with 18%Cr.

The dissolution of the MX precipitates is partially controlled by the $M_{23}C_6$ precipitates. In [31] it is assumed that the MC to $M_{23}C_6$ transformation can take place in several austenitic steels after long time exposure. From the literature alone, it is not possible to clarify if $M_{23}C_6$ or MC is more stable during long-term exposure. More studies are required to explain the interactions between MC and $M_{23}C_6$ precipitates.

Table 2 presents the main characteristics of the MX precipitates in the 25Cr-20Ni-Nb-N steel analysed after solution annealing at 1200-1250°C and after 500h at 750°C as well as after long term exposure at 650°C for 72,075h. The shape of the MX is typically round or cubic. The nucleation sites are grain interior. The main chemical element in MX is niobium and the size is found to be up to ≈300nm.

Table 2: MX precipitates in 25Cr-20Ni-Nb-N austenitic steel.

Temp. [°C]	Time [h]	Shape	Nucleation sites	Main chem. elements	Size [nm]	Investigation method	Reference
≈650	72,075	-	GI	Nb	-	TEM, EDS	[32]
750	500	RD	GI	Nb	-	TEM, SAED	[33]
1200-1250	-	CU	GI	Nb	≈300	TEM, EDS	[34]

GI: Grain interior; RD: Round; CU: Cubic

3.2.1.2 Z-phase

Sourmail [27] reports that Z-phase has a tetragonal unit cell and comprises chromium, niobium, nitrogen; the formula being $Cr_2Nb_2N_2$. Furthermore, the requirement for Z-phase (=complex carbonitride) precipitation are niobium-stabilizing steels with high nitrogen level. During thermal exposure, Z-Phase appears basically on grain boundaries, twin boundaries and within the matrix [27]. In [28] a NF709R austenitic steel with (wt.%) 22Cr and 25Ni is investigated. Two different kinds of Z-phase populations could be found: a large one with a size of ≈1µm and a small one with a size of up to 100nm. The larger one is assumed to form during solidification, whereas the smaller one is formed on dislocations during the thermal exposure. The small fine dispersed Z-phase is assumed to be important for the creep strength [27], acting as obstacles against movement of dislocations. The coarse Z-phase accelerates the initiation of fatigue and especially corrosion-fatigue cracks in ISO 5832-9 austenitic steel with 22%Cr [35]. As reported in [27], [28], the Z-phase grows at the expense of MX precipitates in 20-25Cr austenitic steels. This indicates that the Z-phase is a stable niobium containing phase in 20-25Cr austenitic steels.

In Table 3 the main properties of the Z-phase precipitates in the 25Cr-20Ni-Nb-N are presented. The Z-phase is already found after 500h at 650 and 750°C and is even stable after 88,363h at 700°C. The shape is most whiskers-like, but also a cubic shape is reported. The nucleation sites are grain interior and partially on grain boundaries. The main chemical elements in Z-phase are niobium and chromium. An investigation of long term creep samples (700°C/69MPa/88,363h) of 25Cr-20Ni-Nb-N steel reveals Z-phase inside grains having a chemical composition (wt%) of 54.7Cr-42Nb-1.8Ni-1.5Fe [36].

Table 3: Z-phase precipitates in 25Cr-20Ni-Nb-N austenitic steel.

Temp. [°C]	Time [h]	Shape	Nucleation sites	Main chem. elements	Investigation method	Reference
605	5,400	-	GB, GI	Nb, Cr	TEM, EDS	[37]
605	25,000	-	GB, GI	Nb, Cr	TEM, EDS	[37]
650	500	-	GI	Nb, Cr	TEM, EDS	[34]
650	3,000	-	GI	Nb, Cr	TEM, EDS	[34]
≈650	72,075	WH	GI	Nb, Cr	TEM, EDS	[32], [38]
700	88,363	WH	GI	Nb, Cr	TEM, EDS	[36]
750	500	CU, WH	GI	Nb, Cr	TEM, SAED, EDS	[33]

GI: Grain interior; GB: Grain boundary; CU: Cubic; WH: Whiskers

3.2.1.3 $M_{23}C_6$

According to Sourmail [27], the $M_{23}C_6$ is the most found carbide in the austenitic steels. $M_{23}C_6$ is a general notation for $Cr_{23}C_6$, instead of chromium, there can be nickel, molybdenum and iron. The $M_{23}C_6$ precipitates firstly form at grain boundaries, with increasing time on incoherent twin boundaries, coherent twin boundaries and intragranular (e.g. undissolved NbCN, dislocations) sites. After long ageing times, an interlocked structure of $M_{23}C_6$ precipitates is observed.

The influence of $M_{23}C_6$ on the mechanical properties seems to be dependent on the type of nucleation. $M_{23}C_6$, which form on serrated grain boundaries, tend to be planar and lower in quantity, whereas $M_{23}C_6$ that form on planar grain boundaries tend to be triangular in shape [39]. The triangular ones are more likely to lead to cavity nucleation and further on to failure in austenitic steel AISI304 with 18%Cr [29].

The formation of the $M_{23}C_6$ can be particularly controlled by the steel chemistry. The molybdenum accelerates the formation of the $M_{23}C_6$ whereas the nitrogen retards both the formation and coarsening [27]. A higher content of nitrogen accelerates the formation of Cr_2N and as a consequence the $M_{23}C_6$ formation is retarded [40].

In Table 4 the main properties of the $M_{23}C_6$ precipitates in the 25Cr-20Ni-Nb-N are presented. It shows that the $M_{23}C_6$ are already found after 500h at 650 and 750°C and are even stable after 75,075h at 650°C. The shape is mostly cubic- and rod-like. The nucleation sites are mostly grain boundaries and also intragranular at longer exposure time. The main chemical elements in $M_{23}C_6$ are chromium and particularly nickel. An investigation of 25Cr-20Ni-Nb-N creep samples (650°C/149MPa/17,237.4h) reveal $M_{23}C_6$ precipitates on grain boundaries and inside grains having a chemical composition (wt%) of 74.5Cr-16.5Ni-6.5-Fe-1.8Nb [36].

Table 4: $M_{23}C_6$ precipitates in 25Cr-20Ni-Nb-N austenitic steel.

Temp. [°C]	Time [h]	Shape	Nucleation sites	Main chem. elements	Investigation method	Reference
605	5,400	-	GB	Cr	TEM, EDS	[37]
605	25,000	-	GB	Cr	TEM, EDS	[37]
650	500	-	GB	Cr	TEM, EDS	[34]
650	3,000	CU	GB, GI	Cr	TEM, EDS	[34]
650	17,237	-	GB, GI	Cr, Ni	TEM, EDS	[36]
≈650	75,075	-	GB, GI	-	TEM, EDS	[32], [38]
750	500	CU, RO	GI, GB	Cr	TEM, SAED, EDS	[33]

GI: Grain interior; GB: Grain boundary; Shape: CU: Cubic; RO: Rod

3.2.1.4 σ-phase

The σ-phase has a tetragonal unit cell and its main chemical elements are iron and chromium [27]. Additional compositions are Fe(Cr, Mo) or $(Fe, Ni, Co)_x(Cr, Mo, W)_y$ with $x \approx y$ [7]. In chromium-nickel austenitic steels, the σ-phase forms at first on triple points then on grain boundaries and afterwards, after long term ageing on incoherent twin boundaries and intragranular inclusions [27]. Barcik [41] reports that σ-phase in unstabilised 25Cr-20Ni steels forms at the expense of $M_{23}C_6$, but also independently (directly from the austenite matrix). Unstabilised refers to austenitic steels without carbide former elements such as niobium and titanium which prevents intergranular corrosion. In the case of an independent σ-phase formation, a chromium content in solid solution higher than 18% is necessary. In extra-low-carbon 25Cr-20Ni steels such as 310L, σ-phase forms on the $M_{23}C_6$/austenite surface, with increased free energy. A further investigation of Barcik [42] reveals that the solution conditions influence the kinetics of σ-phase: In fine-grained austenitic steel (AISI 314) the precipitation of σ is faster than in coarse-grained. This effect is also supported by Farooq et al. in [43].

The σ-phase precipitates have very slow kinetics and the precipitate formation can take several hundreds or thousands of hours. There are at least three reasons for the slow kinetics [31]: (i) σ-phase starts to form after the carbides and nitrides are formed; (ii) the complex crystal structure (TCP) which is very different from the parent austenite matrix; (iii) σ-phase contains a lot of substitutional elements which have a slow diffusion. Furthermore, it is reported in [31] that cold forming accelerates the σ-phase formation if there is recrystallization during annealing treatment.

Typical chemical elements which promote the σ-phase are chromium, molybdenum and silicon, while elements such as carbon and nitrogen suppress the σ-phase formation by formation of carbides and nitrides [7].

The influence of σ-phase on the creep strength depends on the σ-phase distribution. Li et al. [44] present that finely dispersed σ-phase mainly along grain boundaries and partially inside grains increases the creep strength of a 25Cr-20Ni austenitic steel, whereas it is expected that σ-phase in lumpy form, for example in commercial stainless steels, does not increase the creep strength. The influence of σ-phase to the toughness is expected to be detrimental. Minami et al. [45] reveal that a formation of σ-phase leads to reduction of toughness. It is assumed that the precipitation of σ in 304H steel contributes mostly to a reduction of impact value after ageing at 700°C up to 50,000h. Similar effects are obtained by Sandström et al. [8] for a 310 austenitic steel. In [31] it is reported that σ-phase precipitation depletes the parent matrix in chromium and molybdenum and thereby causes a dissolution of carbides in this region. Since the chromium is most important for the corrosion resistance, it is assumed that the depletion of chromium in the matrix (caused by σ-phase formation) has a detrimental effect on the corrosion resistance.

In Table 5 the main properties of the σ-phase precipitates in the 25Cr-20Ni-Nb-N are presented. An investigation of creep sample (700°C/69MPa/88,362.7h) reveals σ precipitates on grain boundaries having a chemical composition (wt%) of 47.5Cr-42.7Fe-9.5Ni.

Table 5: σ-phase precipitates in 25Cr-20Ni-Nb-N austenitic steel.

Temp. [°C]	**Time [h]**	**Shape**	**Nucleation sites**	**Main chem. elements**	**Investigation method**	**Reference**
700	88,363	-	GB	Cr, Fe	TEM, EDS	[36]

GB: Grain boundary

3.2.1.5 η-phase

In the literature less information is available about the η-phase. A detailed study about the η-phase in 20Cr-25Ni-4.5Mo austenitic steel is done by Jargelius-Pettersson [46]. After ageing at 850°C for 5 and 3,000h intra as well as intergranular η-phase (fcc structure) could be found. The composition (wt%), is found to be 25-28Cr, 25-35Ni, 25-31Mo, 6-8Fe, 4.2-7.4Si. For η-phase it is often given a composition of Cr_3Ni_2SiN or Cr_3Ni_2SiC. If the nickel content in η-phase is larger than the chromium content, it is better to give the composition as M_5SiN [46]. The high silicon-content, fcc structure and lattice spacing of η-phase are similar to G-phase. These makes it difficult to distinguish between η- and G-phase. However, the silicon-content (14 wt%) in G-phase is higher compared to η-phase and distinguishes the η-phase from the G-phase [46].

3.2.1.6 G-Phase

The general notation of G-phase (fcc structure) is $A_{16}B_6C_7$, where A and B are transition elements and C a Group IV element such as silicon or germanium [47]. A detailed study about the G-phase is done by Powell et al. [48]. They showed that in 20Cr-25Ni stabilized austenitic steels component A is nickel, component B is mostly niobium with small amounts of iron and chromium, and component C is silicon. Carbon is found to be not present in the G-phase. Powell et al. [48] showed that the G-phase forms between 500 and 850°C, initially on grain boundary Nb(C,N) and after longer ageing at Nb(C,N) inside the grains. This investigation suggests that the presence of Nb(C,N) is required for formation of G-phase. It is reported that the transformation from Nb(C,N) to G-phase is faster when the Nb(C,N) are located on the grain boundaries, as a consequence of a higher diffusion along the grain boundaries.

In Table 6 the main properties of the G-phase precipitates in the 25Cr-20Ni-Nb-N are presented. The G-phase is found after 17,237h and even after 75,075h at 650°C. This indicates that G-phase is a very stable phase in the 25Cr-20Ni-Nb-N steel. The G-phase nucleates mainly on grain boundaries and it consists mainly of chromium, nickel and silicon. The exact chemical composition (wt%) of G-phase at ≈650°C/75,075h is found to be 58Cr-28Ni-5Si-4Fe-5others [38] and at 650°C/149MPa/17,237h it is 54.9Cr-38.5Ni-3.1Si-2.2Fe [36].

Table 6: G-phase precipitates in 25Cr-20Ni-Nb-N austenitic steel.

Temp. [°C]	Time [h]	Shape	Nucleation sites	Main chem. elements	Investigation method	Reference
650	17,237	-	GB	Cr, Ni, Si	TEM, EDS	[36]
≈650	75,075	-	GB	Cr, Ni, Si	TEM, EDS	[32], [38]

GB: Grain boundary

3.2.1.7 Precipitation kinetics model in MatCalc

MatCalc [10]–[12] has been used to model the nucleation, growth and coarsening of precipitates in a multi-component and multi-phase system. The nucleation process in MatCalc is based on the Classical Nucleation Theory (CNT) where the input quantities are given from experiments or from theoretical models. The number of newly formed precipitates in MatCalc is defined as the transient nucleation rate [10]:

$$J = N_o Z \beta^* exp\left(-\frac{G^*}{k_B T}\right) exp\left(-\frac{\tau_i}{t}\right) \quad (1)$$

where the N_o is the number of potential nucleation sites, Z is the Zeldovich factor, β^* is the atomic attachment, G^* is the critical nucleation energy, k_B is the Boltzmann constant, T is the absolute temperature, τ_i is the incubation time and t is the time.

The growth and coarsening process is treated separately for randomly distributed [10] and grain boundary arranged [49] precipitates in MatCalc. For randomly distributed precipitates it is assumed that the spherical precipitates are surrounded by spherical diffusion fields and the Gibbs free energy for this system with *n* components and *m* precipitates can be written as [10]:

$$G=\sum_{i=1}^{n}N_{0i}\mu_{0i}+\sum_{k=1}^{m}\frac{4\pi\rho_k^3}{3}\left(\lambda_k+\sum_{i=1}^{n}c_{ki}\mu_{ki}\right)+\sum_{k=1}^{m}4\pi\rho_k^2\gamma_k \tag{2}$$

where N_{0i} is the number of moles of component i in the matrix phase, μ_{0i} is the corresponding chemical potential, ρ_k is the radius of the precipitate with index k, λ_k is the contribution of the elastic energy and plastic work due to the volume expansion of precipitates, c_{ki} is the concentration of component i, μ_{ki} the corresponding chemical potential and γ_k is the precipitate/matrix interface energy. The Gibbs energy is well known to be minimum at thermodynamic equilibrium. A real system is often in a non-equilibrated state; driving forces for precipitation evolution exist which leads to a system where G is gradually reduced. Each change of the microstructure process leads to a dissipation of free energy. In MatCalc, three types of dissipations are considered [10]: dissipation by interface movement Q_1, dissipation by diffusion inside the precipitate Q_2 and dissipation by diffusion inside the matrix Q_3. The dissipation due to interface movement can be written as:

$$Q_1=\sum_{k=1}^{m}\frac{4\pi\rho_k^2}{M_k}\dot{\rho}_k^2 \tag{3}$$

where M_k is the interface mobility and $\dot{\rho_k}$ is the growth rate of the precipitate k. The dissipation by diffusion inside the precipitate can be expressed as:

$$Q_2=\sum_{k=1}^{m}\sum_{i=1}^{n}\int_0^{\rho_k}\frac{RT}{c_{ki}D_{ki}}4\pi r^2 j_{ki}^2\,dr \tag{4}$$

where R is the universal gas constant, c_{ki} the concentration, r is the particle radius ($0 < r < \rho_k$), j_{ki} is the flux- and D_{ki} is the diffusion- coefficient of component i in the precipitate k. The dissipation by diffusion inside the matrix Q_3 can be written as:

$$Q_3=\sum_{k=1}^{m}\sum_{i=1}^{n}\int_{\rho_k}^{Z}\frac{RT}{c_{0i}D_{0i}}4\pi r^2 J_{ki}^2\,dr \tag{5}$$

where Z is the mean distance between two precipitates, c_{0i} is the concentration and D_{0i} is the diffusivity of element i in the matrix. Finally, the total dissipation is defined as $Q = Q_1+Q_2+Q_3$. According to the thermodynamic extremum principle [10], the growth rate and the rate of change of chemical composition $\dot{c_{ki}}$ of the precipitate can be obtained.

In case that precipitates nucleate on the grain boundaries, the assumption with the spherical diffusion field is not valid anymore. For the grain boundaries precipitates, two different dissipation mechanisms are considered: dissipation due to diffusion in the grain boundary Q^g and dissipation due to diffusion in the grain Q^b. The corresponding equations can be found in [49].

3.2.2 Creep strength of austenitic steels

The creep rupture time of the 25Cr-20Ni-Nb-N steel (HR3C) is shown in Figure 4. The temperatures of 650 and 750°C which are relevant for the present thesis are marked with blue- and red-colour. The average creep rupture strength after 1,000h at 650°C is ≈250MPa and at 750°C it is ≈110MPa.

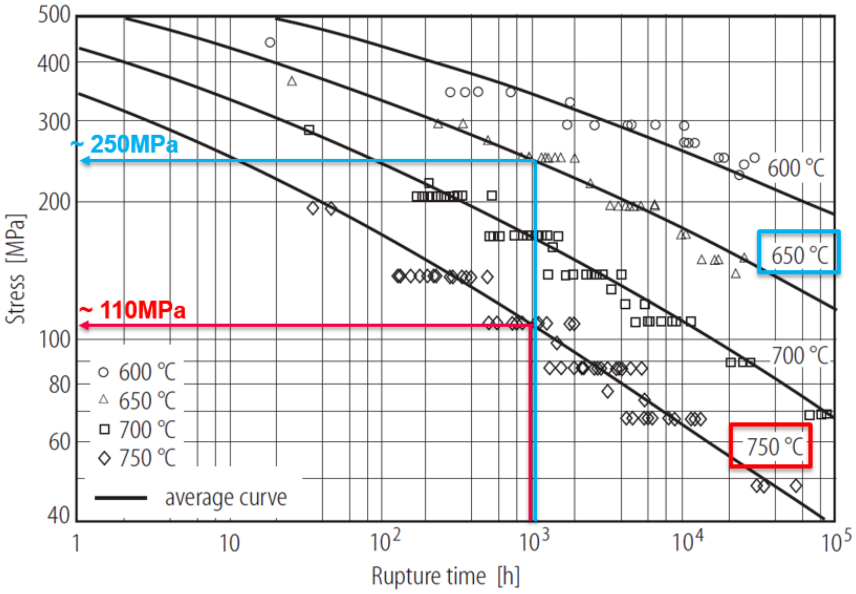

Figure 4: Creep rupture times of HR3C austenitic steel (25Cr-20Ni-Nb-N) [24].

Figure 5 shows the influence of nickel, niobium and nitrogen on the creep strength of 25Cr-20Ni-Nb-N. As it can be seen, the rupture strength is significantly increased with higher nitrogen content. Niobium has the same effect. Samples without niobium have the lowest rupture strength, when adding niobium the rupture strength is increased. The influence of nickel on the rupture strength seems to be low compared to nitrogen and niobium.

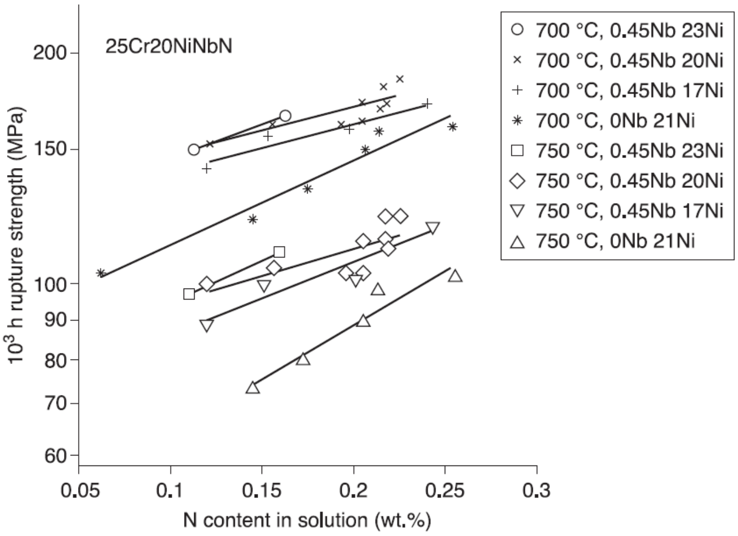

Figure 5: Influence of nickel, niobium and nitrogen on the 1000 h creep rupture strength of 25Cr-20Ni-Nb-N (HR3C) [50].

Creep means a plastic deformation of material, at constant load and as a function of time. Depending on the material, creep can take place at low and high temperature. Generally for steels, temperatures higher than 0.4 solvus temperature are relevant for creep [7].

Creep strength means resistance against plastic deformation. Several hardening mechanisms exist in the steels which contribute to the creep strength. It is reported by Bürgel et al. [7] that at low temperature (below 0.4 solvus temperature) four hardening mechanisms contribute to the strength: dislocation, fine grain, solid solution and precipitation strengthening. At high temperature during creep (above of 0.4 solvus temperature) these hardening mechanisms are particularly promised: the contribution from dislocation is decreasing for long time exposure due to the recovery; contribution from fine grains is not promising, a coarse grain is desirable; contribution from solid solution is decreasing with increasing temperature; contribution from precipitates is most promising.

For the 25Cr-20Ni-Nb-N steel three main contributions to the creep strength are expected: from dislocations, from precipitates and from elements in solid solution. These three contributions are analysed by the creep strength modelling approach of Sandström et al. [13]–[18] and are summarized in this chapter.

3.2.2.1 Dislocation hardening

Dislocations represent an effective barrier to the motion of other dislocations. To represent this contribution to the strength, the development of the dislocation density have to be understood. New dislocations are generated during work hardening at the same time as other dislocations are annihilated due to recovery. According to the classical recovery model for creep, there is a balance between work hardening and recovery during secondary creep. The work hardening and the recovery can be modelled by the following equation for the strain dependence of dislocation density ρ [14]:

$$\frac{d\rho}{d\varepsilon} = \frac{m}{bL} - 2\tau_L M(T,\sigma)\rho^2/\dot{\varepsilon} \tag{6}$$

where ε is the strain, b is Burger's vector, L is the "spurt" distance, which the dislocation moves when it is released during deformation. m is the Taylor factor (3.06 for fcc materials), τ_L the dislocation line tension, M the dislocation mobility, and $\dot{\varepsilon}$ the strain rate. The two terms on the right hand side of the equation are the Orowan expression for the work hardening, and the static recovery term. The spurt distance L can be assumed to be of the order of the subgrain size, i.e. after a dislocation link has been released, it is primarily stopped by the subgrain boundaries. In fact, for single crystals it has been demonstrated that the spurt distance is controlled by the subgrain size [51], [52]. The subgrain diameter (d_{sub}) can in turn be related to the stress and dislocation density [14].

$$L = d_{sub} = \frac{KGb}{\sigma} = \frac{K}{\alpha m \rho^{1/2}} \tag{7}$$

where α is a constant and G the shear modulus. The constant K is about 20 for austenitic stainless steels [53]. In deriving eq. (7), the Taylor equation is used.

$$\sigma_{disl} = m\alpha Gb\sqrt{\rho} \tag{8}$$

In the relation for the subgrain size in eq. (7), it is usually assumed that the total creep stress should be applied. However, as it will be seen below, the total and the dislocation stresses are of the same order of magnitude, so no distinction is made between them in the expression for the spurt distance.

For stationary conditions where dρ/dε=0, eq. (6)-(8) gives

$$\dot{\varepsilon}_{min} = \frac{2bK\tau_L}{\alpha m^2} M(T,\sigma_{disl}) \left(\frac{\sigma_{disl}}{\alpha m G b}\right)^3 \tag{9}$$

If the stress dependence of the mobility M is not considered, eq. (9) is a Norton equation with a creep exponent of 3. At very high temperatures this might be a satisfactory approximation. If only climb is considered, Hirth and Lothe give the following expression for the mobility [54]

$$M_{climb}(T,\sigma) = \frac{D_{s0}b}{k_B T} exp\left(\frac{\sigma b^3}{k_B T}\right) exp\left(-\frac{Q}{RT}\right) \tag{10}$$

where T is the temperature, D_{s0} the pre-exponential coefficient for self diffusion, Q the activation energy for self diffusion, b the Burgers vector, k_B the Boltzmann's constant, and R the gas constant. The lattice diffusion coefficient is used. It has been shown that pipe diffusion is negligible for 20Cr-25Ni-Nb-N at investigated temperatures [55]. The stress dependence in (10) is small. It is well established that the creep exponent can be much higher than three to five at lower temperatures, which is referred to as the power-law break down regime. By taking glide into account a strongly stress dependent dislocation mobility is obtained that is applicable also in the power-law break down regime [16], [18]:

$$M(T,\sigma) = \frac{D_{s0}b}{k_B T} exp\left(\frac{\sigma b^3}{k_B T}\right) exp\left(-\frac{Q}{RT}\left[1-\left(\frac{\sigma}{\sigma_{max}}\right)^2\right]\right)/f_{sol} \tag{11}$$

σ_{max} is taken as the tensile strength at ambient temperatures and f_{sol} a constant that takes the influence of elements in solid solution into account. All the other parameters are readily available. By combining eq. (9) and (11) an expression for the secondary creep rate as a function of stress is obtained. By solving this expression for the stress at a given strain rate by iteration, the dislocation contribution to the creep strength is obtained.

3.2.2.2 Precipitation hardening

Traditionally, the contribution from precipitation hardening to the creep strength is estimated based on Orowan bowing of dislocations around the particles. In Figure 6(A) a schematic dislocation bypassing of non-scherable precipitate is shown. Driven by shear stress the dislocation moves against two precipitates (1). The bowing of dislocation starts after the contact between dislocation and precipitates (2), see also Figure 6(B). This bowing is present until the dislocation loops around the precipitates (3). After bypassing, dislocation loops remain around the precipitates (4).

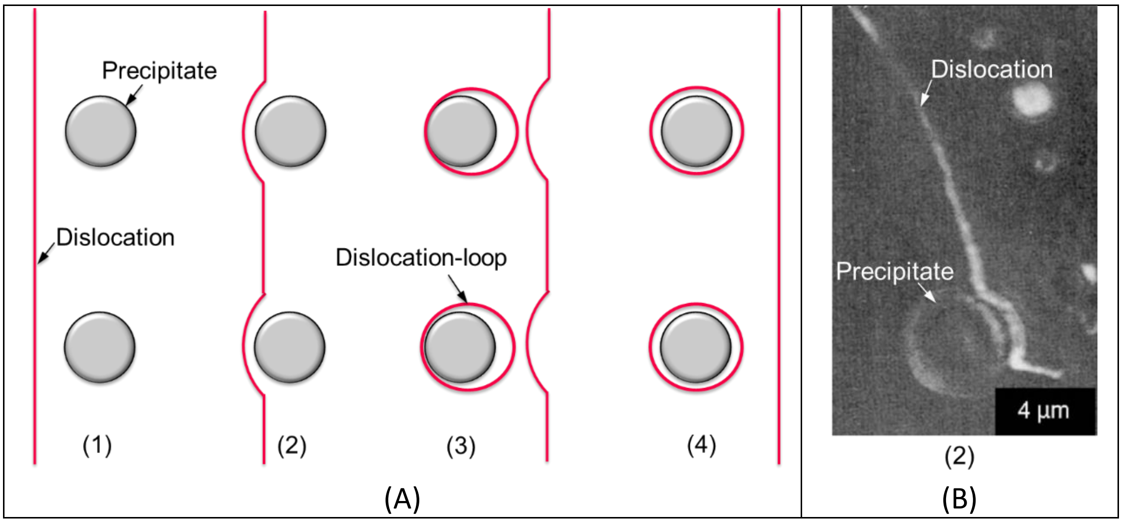

Figure 6: Orowan bowing (A) and interaction between dislocation and precipitates in nickel alloy (B) [56].

A number of different types of particles are present in 25Cr-20Ni-Nb-N. For each particle type marked with an index i, the Orowan strength contribution has the following simple mathematical form [57]:

$$\sigma_{part_i} = 0.8\frac{2\tau_L m}{bL_{part_i}} \qquad (12)$$

where L_{parti} is the average distance between the particles of type *i* (in a square network) and can be determined from the precipitation calculations:

$$L_{part_i} = \sqrt{1/N_{A_i}} \qquad (13)$$

where N_{Ai} is the total number of particles of type *i* per unit area

$$N_{A_i} = \frac{3}{2\pi f_{vol_i} R_i^2} \qquad (14)$$

where f_{voli} is their volume fraction and R_i the 3D-radius of the particle of type *i*. Eq. (12) is essentially temperature independent except for the weak temperature dependence of the line tension τ_L or if L_{parti} shows a pronounced temperature variation. In contrast, the creep strength decreases approximately exponentially with increasing temperature for a given rupture time. At high temperatures, dislocations can climb across the particles and as a consequence, eq. (12) strongly overestimates the contribution to the creep strength.

In the past, many attempts were made to compute the stress required for dislocation to climb across the particles. If the dislocations are attached to the particles when they pass them (local climb), the stress has been estimated to about half the Orowan strength [58]. However, when the dislocations are only in contact with the particles at single points (general climb), the stress is negligibly small [59]. It has been convincingly shown that general climb is the energetically favourable case [60]. It can be concluded that there is no stress barrier for dislocations to climb across particles.

The solution to this dilemma is to assume that it is the time it takes for the dislocation to climb across the particles that decides whether a particle will be climbed or not. More specifically the following assumptions have to be made [61], [62]:

- The controlling mechanism is the time it takes for a dislocation to climb across a particle.
- A critical radius r_{crit} is introduced, which is the maximum particle size where there is sufficient time for dislocations to climb across particles during the design life.
- For smaller particles ($r< r_{crit}$) there is sufficient time for the dislocation to climb across them. These particles will not contribute to the strength.
- Larger particles have to be passed by Orowan bowing.

Figure 7 shows a schematic illustration of particle passing mechanisms at high temperature. Most of the particles in the present austenitic steel are incoherent (due to large size and/or different crystal structure compared to the austenite matrix) and will be therefore passed by climbing and Orowan bowing. In the present creep strength modelling approach it is assumed that precipitates smaller than the critical radius r_{crit} do not contribute to the creep strength, whereas precipitates larger than r_{crit} contribute to the creep strength by Orowan bowing. The critical radius r_{crit} increases with decreasing applied stress, increasing temperature and increasing creep time.

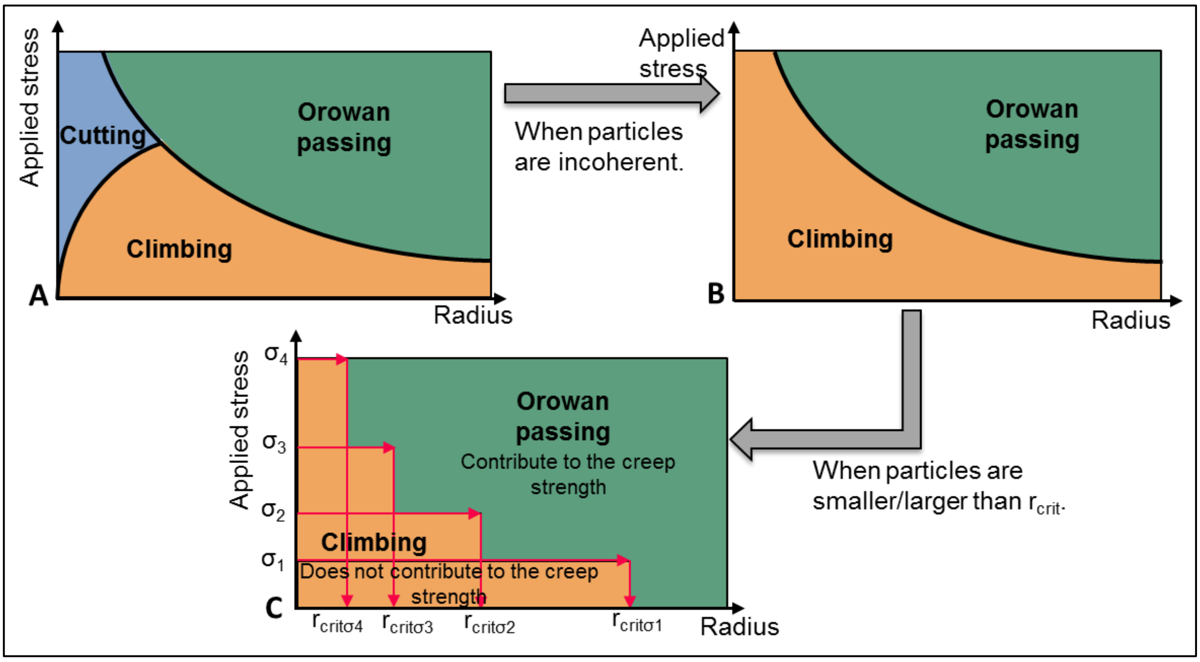

Figure 7: Particles passing mechanisms at high temperature for (A) coherent and incoherent particles, (B) only incoherent particles and (C) incoherent particles with radius smaller/larger than critical radius r_{crit}. Compiled by author and based on [61], [62].

The contribution of larger particles (larger than r_{crit}) to the strength is obtained with the Orowan mechanism

$$\sigma_{part_i} = 0.8\frac{2\tau_L m}{bL_{rcrit_i}} \tag{15}$$

where L_{rcriti} is the average interparticle distance for particles larger than r_{criti} for particle type *i*. For 25Cr-20Ni-Nb-N and other materials, the size distributions often have an exponential form [13].

$$n_{A_i}(r) = N_{A_i}exp\left(-\beta_i(r - r_{0i})\right) \tag{16}$$

where N_{Ai} is the total number of particles of type *i* per unit area, and $n_{Ai}(r)$ the number of particles larger than *r*. *r* is the particle size, r_0 the smallest accurately recorded particle size, and β_i a constant, that is taken as the inverse (average) particle radius.

The critical radius can be computed as the available time for climb t_{climb} multiplied by the climb velocity v_{disl} of the dislocations, which can in turn be expressed with the help of the climb mobility.

$$2r_{crit} = t_{climb}v_{disl} = t_{climb}bM_{climb}\sigma \tag{17}$$

The available climb time can be taken as half the design life. The interparticle spacing L_{rcriti} can then be determined with the help of eqs. (16) and (17). For a square network of particles we find that

$$L_{rcrit_i} = \sqrt{1/n_{A_i}\left(r_{crit_i}\right)} \tag{18}$$

To sum the strength contributions from different particles types, σ_{parti}, the squares of the individual contributions are added [63]. The total contribution is then given by

$$L_{part_{tot}} = 1\Bigg/\sqrt{\sum_i 1/L_{part_i}{}^2} \qquad \sigma_{part_{tot}} = \sqrt{\sum_i \sigma_{part_i}{}^2} \tag{19}$$

3.2.2.3 Solid solution hardening

3.2.2.3.1 Substitutional elements

Due to lattice misfit, elements in solid solution give rise to a hardening effect that increases the creep strength. This section gives a summary of models that are presented in detail elsewhere [13], [15]. The maximum interaction energy between a solute and an edge dislocation can be expressed as

$$U_i^{max} = \frac{1}{\pi}\frac{(1+\nu)}{(1-\nu)} G\Omega_0\varepsilon_i \frac{b}{r_{sol}} \tag{20}$$

where G is the shear modulus, ν is the Poisson’s ratio, b is Burgers' vector, Ω_0 is the atomic volume in the host alloy, r_{sol} is the distance from the solute to the centre of the dislocation, and ε_i is the linear atomic size misfit parameter of solute *i*

$$\varepsilon_i = \frac{\partial a}{a\partial c_i} \tag{21}$$

a is the lattice parameter, and c_i the concentration of the solute element *i*. For the austenitic stainless steel 23Cr-25Ni-W-Cu-Co, the lattice misfit parameters ε_i have been computed with first-principles methods [15]. The solute is believed to be quite close to the centre of the dislocation and a value of $r_{sol} = 2b/3$ has been assumed. This might somewhat overestimate the interaction energy, since this distance is smaller than what is typically found for the core radius of the dislocations in first-principles calculations [64]. The resulting value for the misfit parameter for Nb is $\varepsilon_i = 0.253$. With a Poisson's ratio $\nu = 0.3$, the shear modulus $G = 52.5$ MPa, and the atomic volume $\Omega_0 = 1.21 \times 10^{-29}$ m^3, we find that

$$U_i^{max} = 339\varepsilon_i(kJ/mol) \tag{22}$$

This gives an interaction energy of 85.8 kJ/mol. The concentration of solutes around non-moving (static) dislocations c_i^{stat} can be formulated as [54].

$$c_i^{stat} = c_i^0 exp(-U_i(x,y)/k_BT) \tag{23}$$

where c_i^0 is the concentration of solute *i* in solid solution, k_B Boltzmann's constant and *T* the absolute temperature. (x,y) are the Cartesian coordinates of the position of the solute relative to an edge dislocation, which is climbing in the y-direction. The concentration of solutes around a moving dislocation c_i^{dyn} gives a slightly more complicated formula [54]

$$c_i^{dyn} = \frac{v_{disl} c_i^0}{D_i^{sol}} exp\left(-\frac{U_i(x,y)}{kT} - \frac{v_{disl} y}{D_i^{sol}}\right) \int_{-\infty}^{y} exp\left(\frac{U_i(x,y')}{kT} + \frac{v_{disl} y'}{D_i^{sol}}\right) dy' \qquad (24)$$

where v_{disl} is the velocity of the dislocation, and D_i^{sol} the diffusion coefficient for the solute *i*. v_{disl} is given by eq. (17). The presence of solutes gives rise to a drag stress on the dislocations, which reduces the climb rate and increases the creep strength. The drag stress can be expressed as [54]

$$\sigma_i^{drag} = \frac{F}{bL} = \frac{kTv}{bD_i} \int_A \frac{(c_i - c_i^0)^2}{c_i} dA \qquad (25)$$

where σ_i^{drag} is the drag stress from solute *i*, *F* the force per unit length *L* of the dislocation and *A* the area surrounding the dislocation. It has been shown that the static solution in eq. (23) can be used to compute the integral in (25) [15], [54]. The solution is

$$\sigma_i^{drag} = \frac{v c_o \beta^2}{b D_i k_B T} I(z_0) \qquad (26)$$

where $z_0=\beta/r_0 k_B T$ and the integral $I(z_0)$ is

$$I(z_0) = \int_1^{z_0} \frac{2\sqrt{2\pi}}{3} z^{-5/2} e^z dz \qquad (27)$$

$I(z_0)$ can be computed numerically.

It is evident from Figure 30 on page 64 that the distribution of solutes is sharply peaked around the dislocations. When the dislocations move, the solutes have to jump in and out of the cloud. This requires an activation energy in addition to that for the self-diffusion during climb. As an effect, the creep rate is lowered by the factor

$$f_{sol} = \exp(-Q_{sol}/kT) \qquad (28)$$

Consequently, solid solution hardening raises the activation energy for creep. This explains why the activation energy for creep of austenitic stainless steels is considerably larger than that for self-diffusion. Q_{sol} is chosen as the maximum interaction energy U_i^{max} from eq. (20).

3.2.2.3.2 Interstitial elements

It is well-known that nitrogen raises the creep strength, see for example [65]. As it will be demonstrated in section 5.3.1, nitrogen-containing precipitates significantly contribute to the creep strength. However, a contribution from solid solution hardening from nitrogen can also be expected. In this case, eq. (26) cannot be applied. In fact, it gives a negligible contribution for interstitial elements due to their fast diffusion. In spite of this, fast diffusion elements can give a significant contribution to the creep strength. This has been demonstrated for phosphorus in copper, where only 50 wt. ppm P gives a large increase in the creep strength [15], [18]. It appears that the small elements are locked to the dislocation, and that a break stress is needed to make the dislocations move, which gives the solid solution hardening. The break stress σ_{break} was derived in ref. [18]

$$\sigma_{break} = \frac{U_i^{max}}{b^3} \int_{y_l}^{y_r} c_i^{dyn} \, dy \tag{29}$$

The integral in (29) (*L* and *R* stand for left and right) is performed over the solute distribution such as the one in Figure 30 on page 64. It is the dynamic content according to eq. (24) that should be applied in eq. (29). For nitrogen, it is possible to estimate the lattice misfit parameter from how the element affects the lattice parameter. Data for very large nitrogen contents [66] have been used. The resulting value for the linear misfit parameter is $\varepsilon_l = 0.025$.

3.2.2.4 Total creep strength

The total creep strength of 25Cr-20Ni-Nb-N steel is obtained by adding the contributions from the different mechanisms. The predicted total creep strength is called σ_{appl}

$$\sigma_{appl} = \sigma_{disl} + \sigma_{PH} + \sigma_{sol} + \sigma_{solN} \tag{30}$$

where the σ_{disl} is the contribution from dislocation, σ_{PH} from precipitates, σ_{sol} solid solution and σ_{solN} solid solution from N. The σ_{appl} should be directly comparable with the measured creep rupture strength σ_{exp}.

4 Material and Experimental

4.1 The 25Cr-20Ni-Nb-N austenitic steel

For the investigations six samples are used. The samples (10x10x2mm) were extracted from a solution treated (at 1230°C) and cold finished seamless tube produced by extrusion. An ageing treatment at 650 and 750°C for 1,000, 3,000 and 10,000h is applied by Forschungszentrum Jülich. A grain size of 22µm is measured by the KTH Stockholm. The chemical composition is presented in Table 7.

Table 7: Chemical composition (wt%) of 25Cr-20Ni-Nb-N steel.

Fe	C	Cr	Si	P	Ni	Nb	Mn	N	S	O
51.9	0.062	24.7	0.38	0.017	20.6	0.44	1.2	0.1819	<0.0005	0.0162

4.2 Microstructure Investigation Methods

4.2.1 Scanning Electron Microscope (SEM)

The scanning electron microscope (SEM) is mainly used for the investigation of the precipitates composition, distribution as well as nucleation sites of large precipitates like $M_{23}C_6$ and σ-phase. The samples for the SEM investigations are mechanically grinded, polished and electrolytically etched. The electrolytic etching is performed with a 10% solution of oxalic acid in distilled water at 3 volts for 10 to 60s. The chemical composition of the precipitates is measured by EDS. In order to compare the precipitation evolution calculation with experimental data, the experimental mean radii and phase fractions of the precipitates are the most convenient data. For the comparison it is necessary to convert the measured area fraction of the precipitates into phase fractions. This is done by the standard method described in [67]. The SEM investigations are performed by the KTH Stockholm with a JEOL 7000F SEM equipped with EDS system.

The investigation of the modified 25Cr-20Ni-Nb-N steel (see chapter 6.4 on page 87) is performed at the Institute of Material Science and Welding (IWS). The samples of the modified steel are mechanically grinded and afterwards vibration polished using Bühler Vibromet 2 with an OP-AA (Acidic Alumina) suspension for high-alloy steels. Furthermore, the samples are investigated using a LEO 1450 VP scanning electron microscope. Due to the low resolution of this SEM, the observation was restricted to the phase fraction and radius of primary Z-phase precipitates and the presence of grain boundary precipitates.

4.2.2 Transmission Electron Microscope (TEM)

The transmission electron microscope (TEM) is mainly used for the investigation of the precipitates composition of smaller precipitates such as secondary Z-phase and MX precipitates. The TEM investigations are performed with carbon replicas. The TEM samples are mechanically grinded, polished and chemically etched in a solution of 40% HCl, 20% HNO_3 in distilled water at 60°C for 10s. The carbon replicas are evaporated with carbon onto chemically etched specimens followed by the dissolution of the metallic matrix in a solution of 40% HCl, 20% HNO_3 in distilled water at 60°C. The chemical composition of the precipitates is measured by EDS. The TEM investigations are performed by the KTH Stockholm with a JEOL-TEM (200kV) equipped with EDS system. It has to be mentioned that the phases have been identified with the help of the SEM- and TEM- EDS system. No electron diffraction has been performed. The uncertainties with EDS for smaller precipitates are particularly significant, therefore the results should be interpreted with some caution.

4.3 Thermodynamic and Thermokinetic Calculations

The calculation of the precipitation evolution is a quite complex process with several steps. A general overview of a procedure for a precipitation calculation is given in Figure 8. The first step is an equilibrium calculation where the thermodynamic equilibrium phase fractions versus temperature, solvus temperatures and transformation points are calculated. The second step is a Scheil-calculation [68]–[70] where the effect of the segregation processes during solidification on the formation of the precipitates is calculated. The main output of the Scheil calculation is the phase fraction of primary precipitate phases versus temperature during cooling down after melting. The third step is the precipitation kinetic calculation. Since precipitation kinetic simulations are generally restricted to the formation of particles due to diffusional processes in solid materials, primarily formed precipitates have to be considered separately. For this reason, the calculated data on the primary precipitates (from Scheil calculation) have to be used as input data for the precipitation calculation. Additionally to the primarily formed precipitates, the heat treatment, grain size, nucleation sites, dislocations density and precipitates shape factor have to be known. These additional input data can be obtained by experimental investigation or literature research.

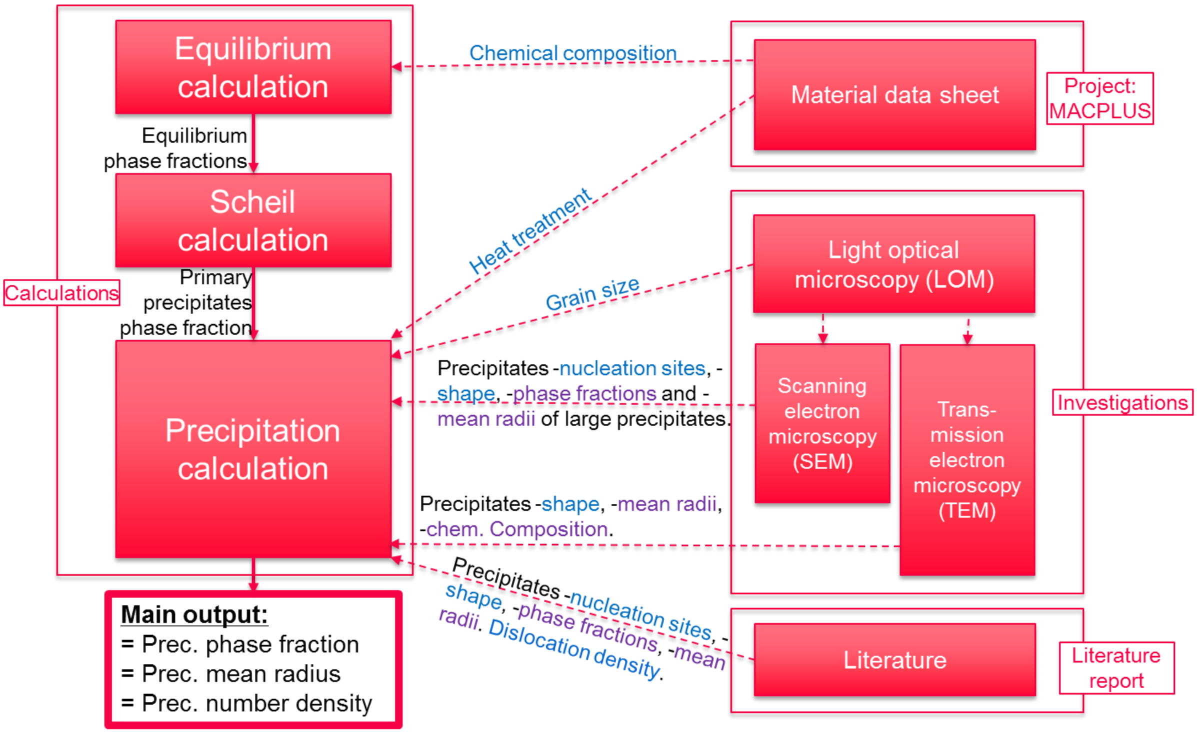

Figure 8: General procedure for precipitation calculation (input parameters are marked in blue and evaluation parameters in purple).

4.3.1 Setup for Equilibrium and Scheil Calculations

The equilibrium and Scheil [68]–[70] calculations are performed with the MatCalc version 5.52 (rel 1.010) and the thermodynamic database mc_fe_v2.016. The N(bC,N) and Cr_2N phases are not defined as a separate phase in the MatCalc database, only their parent phase can be selected. As consequence, the elements for Nb(C,N) and Cr_2N have to be defined by the command “composition set”. Niobium, carbon and nitrogen are defined for Nb(C,N), whereas chromium and nitrogen are defined for Cr_2N.

For the Scheil calculation, only back diffusion of carbon and nitrogen was allowed, all other elements were assumed not diffusing during cooling. These conditions meet the situation for a broad bandwidth of medium cooling rates.

4.3.2 Setup for Precipitation Calculations

The precipitation kinetics calculations are performed with the MatCalc version 5.52 (rel 1.010), the thermodynamic database mc_fe_v2.016 and the diffusion database mc_fe_v2.005. The precipitation evolution calculation is performed by MatCalc script which is shown in the Appendix on page 113.

For the precipitation kinetics calculations, eight precipitates are considered: $M_{23}C_6$, σ-phase, primary Z-phase, secondary Z-phase, primary Nb(C,N), secondary Nb(C,N), η (Cr_3Ni_2SiN) and G-phase. Since precipitation kinetic simulations are generally restricted to the formation of particles due to diffusional processes in solid materials, primarily formed precipitates have to be considered separately. For this reason, the calculated data on the primarily formed precipitates (from Scheil calculation) have to be used as input data for the precipitation calculation. By analysing micrographs, the nucleation sites for different types of precipitates are partly identified as described in Table 8 on page 42. Grain boundaries are defined as nucleation sites for $M_{23}C_6$, Cr_3Ni_2SiN and G-phase, see Figure 9. It has to be mentioned that G-phase was not found experimentally, but it was reported in [32], [38] to nucleate on grain boundaries. The nucleation of $M_{23}C_6$ at grain-, twin-boundaries and slip bands is taken into account in the following way: since twin boundaries and slip bands as nucleation sites are not available in MatCalc, subgrain boundary corners which are expected to have a similar density, are selected as a substitute. σ-phase is considered to nucleate at grain boundary corners which is in agreement with the observations. The nucleation sites of secondary Nb(C,N) and Z-phase are defined to be at dislocations.

It is reported in [32], [38] that the Z phase has an elongated shape, so that a shape factor (relation length/width) of 3 is defined for Z phase. The same applies to $M_{23}C_6$ where also a shape factor of 3 is used.

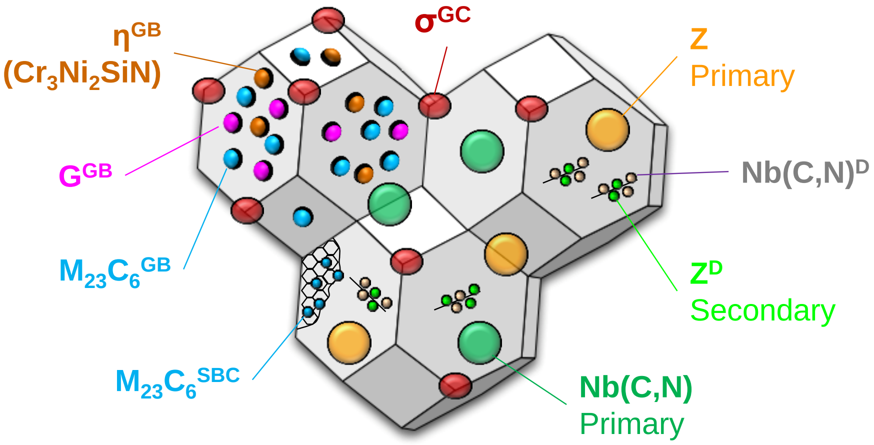

Figure 9: Nucleation sites of precipitates. GB: Grain boundary; D: Dislocation; GC: Grain corner; SBC: Subgrain boundary corner. Compiled by author and based on [71].

The interfacial energies for the particles are calculated automatically by the GBB (General Broken-Bond) model [72]. Since the ageing temperatures of 750°C is close to the σ-phase solution temperature (800°C according to equilibrium calculation), it is assumed that the σ-phase interface becomes diffuse [73] and therefore an interface energy correction of 0.45 for 750°C was applied. No correction of σ-phase interface energy for 650°C is applied.

The experimentally measured value of 22µm is used for the grain size. Since the extrusion process causes a strong plastic deformation, a dislocation density for the austenite matrix is set to $1x10^{12}m^{-2}$.

The investigated austenitic steel passed several different temperature cycles during the manufacturing process of the tube. When the precipitation evolution is simulated, only the solution annealing is considered, but not the previous applied temperature cycles from the manufacturing process. There are several reasons why the manufacturing process is not considered, some of them are (i) process parameters such as heating-, cooling-rates and holding times are not given by the manufacturer, (ii) no records of temperature profile were found. Only the solution annealing heat treatment is known, and thus is considered for the precipitation evolution. However, by discussion with some manufacturers it was tried to estimate the temperature profile during the manufacturing route. When this estimated temperature cycle was applied, no significant differences in precipitation evolution during service were observed. The main reason for that was that most of the precipitates (except Nb(C,N) and primary precipitates) are dissolved during the solution annealing and thus the previous applied temperature cycle becomes unimportant. Only the Nb(C,N) precipitates became a bit larger, but this was not significant. Due to the low influence of the estimated temperature cycle and significant higher calculation time it was decided to not consider the manufacturing process.

The studied heat treatment is shown in Figure 10 and consists of five segments: heating to solution temperature, solution annealing at 1230°C for 10min, quenching, heating to service temperature and ageing at 650 and 750°C for 100,000h.

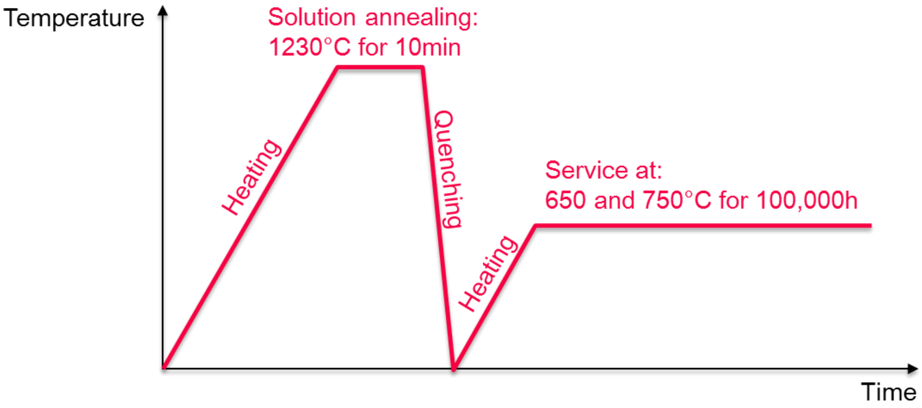

Figure 10: Applied heat- and service- treatment for the precipitation calculation.

4.4 Creep strength modelling

A basic overview of the applied creep strength modelling procedure for austenitic steels at e.g. 650°C is shown in Figure 11. Three main contributions to the creep strength are expected: from dislocations, from precipitates and from elements in solid solution. The rupture elongation has to be known in order to calculate the dislocation hardening. In the case of the HR3C a rupture elongation of ε_r=20% is assumed, which is a typical value for austenitic stainless steels. This value does not have a large influence on the results as long as the stress exponent is high. So a typical ε_r can be assumed and kept constant for different stresses and temperatures such as 650 and 750°C. The precipitation and solid solution hardening were calculated using the results from the precipitation and equilibrium calculations.

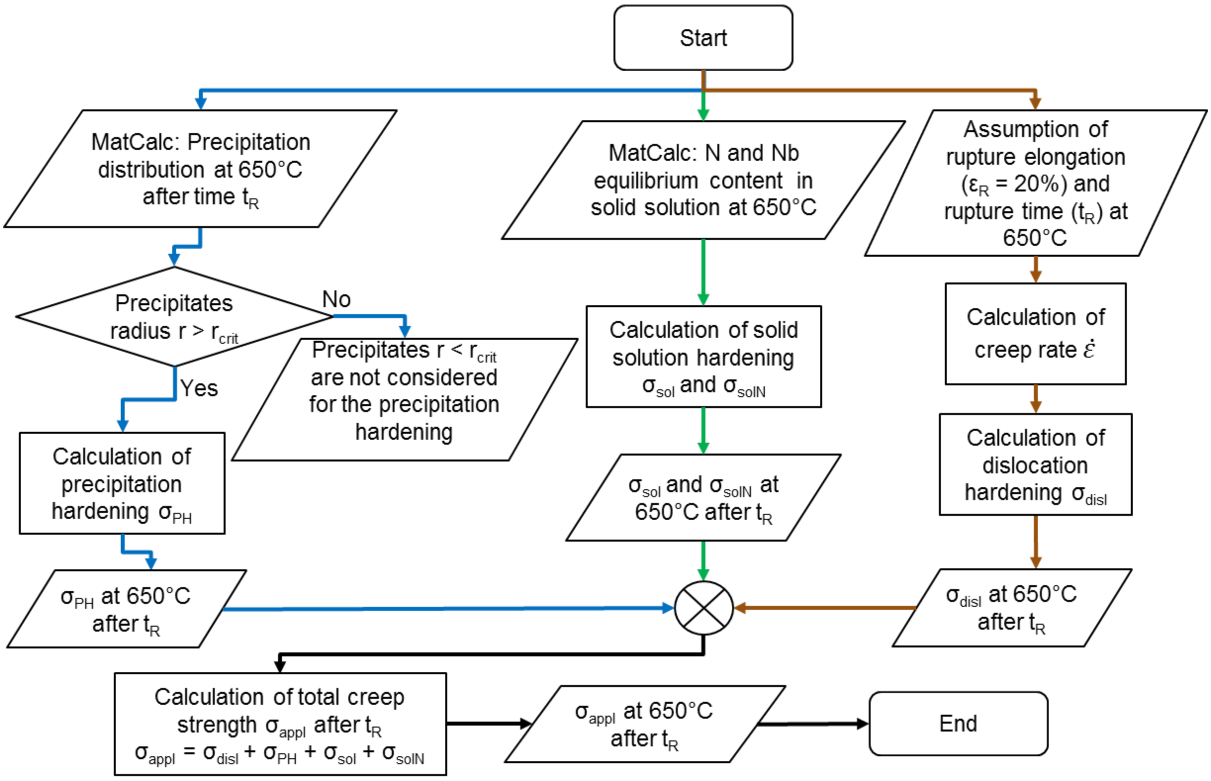

Figure 11: Overview of creep strength modelling procedure for austenitic steels at e.g. 650°C. ε_R refers to the rupture elongation of austenitic steels and t_r to the creep rupture time.

5 Results and Discussion

5.1 Microstructure

5.1.1 Microstructure at 650°C

Samples aged at 650°C for 1,000, 3,000 and 10,000h reveal five different precipitates: Z-phase, $M_{23}C_6$, Nb(C,N), η ($Cr_3Ni_2Si(C,N)$) and σ-phase. Additionally, two different oxides are found: Al- and Si-oxide.

Considering the **Z-phase**, two different populations of Z-phase are observed: a primary one with a mean diameter of up to 3.5µm, see Figure 12(A), and a secondary one with a diameter of several nanometres. The shape of the primary one is irregular, it varies between round- and square-shape. An elongated cluster of primary Z-phase precipitates is often observed. The **Nb(C,N)** precipitates are mainly round shaped. Its diameter varies from several nanometres up to ≈380nm, see Figure 12(B). The **$M_{23}C_6$** are mainly observed at grain boundaries, but at longer ageing times also at twin boundaries and slip bands. The shape of the $M_{23}C_6$ is sometimes found to be cubic, but mainly elongated as can be seen in Figure 13(Spectrum1, 2).

The nucleation sites and shape of the **η-phase** is found to be similar to $M_{23}C_6$. Significant amounts of **σ-phase** are only found after longer ageing times (after 5,000h). The σ-phase is found mainly on triple points of grain boundaries having a mean diameter of ≈2.8µm after 10,000h at 650°C. Only fiew oxides are found, in Figure 12(A) an Al-oxide (1) and in Figure 12(B) two Si-oxides (Spectrum 1, 3) are shown.

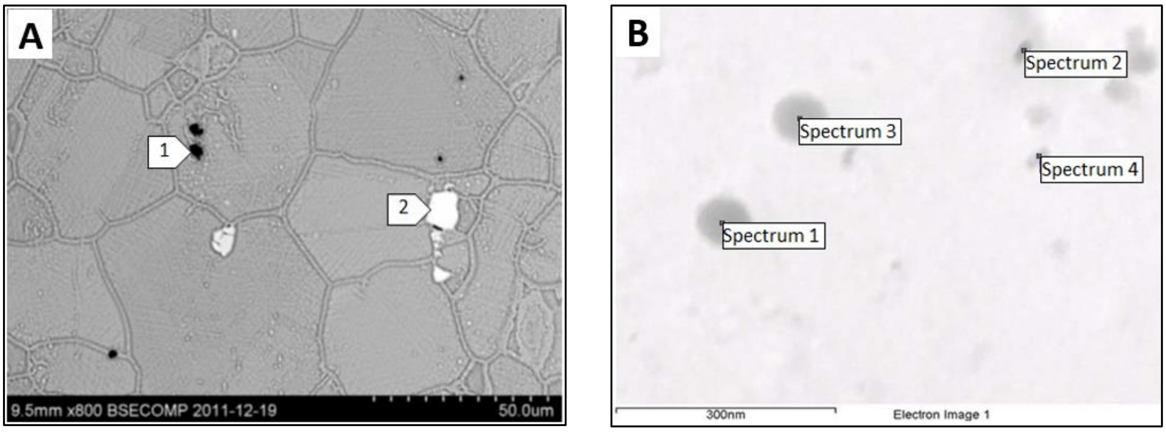

Figure 12: SEM image of 650°C/1,000h (A) and TEM image of 650°C/3,000h (B) aged sample. A-1: Al-oxide; A-2: primary Z-phase; Spectrum 1, 3: Si-oxide; Spectrum: 2, 4: Nb(C,N).

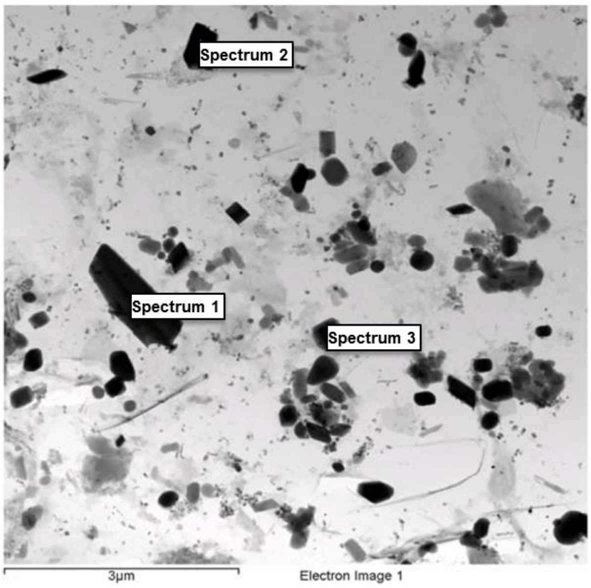

Figure 13: TEM replica of 650°C/10,000h aged sample. Spectrum 1-2: $M_{23}C_6$; Spectrum 3: Nb(C,N).

The phase fractions and mean radii of precipitates are the most convenient data to evaluate the precipitation calculation. The SEM investigations are used to obtain these parameters for the $M_{23}C_6$ and σ-phase precipitates. Unfortunately, due to time constraints and resolution limit of the SEM, other precipitates could not be evaluated. As shown in Figure 14, the phase fractions and mean radii of $M_{23}C_6$ and σ-phase precipitates are increasing with increasing ageing time.

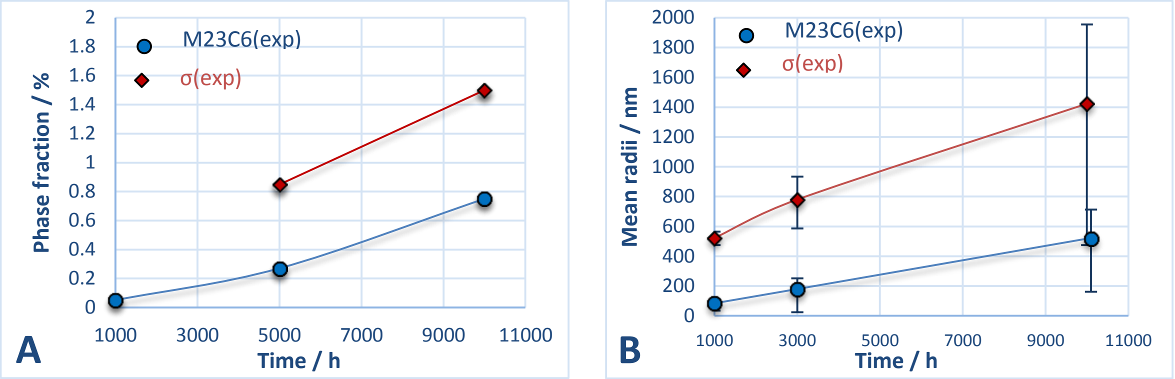

Figure 14: Measured phase fractions (A) and mean radii (B) of $M_{23}C_6$ and σ-phase at 650°C.

5.1.2 Microstructure at 750°C

Samples aged at 750°C for 1,000, 3,000 and 10,000h reveal five different precipitates: Z-phase, $M_{23}C_6$, Nb(C,N), η ($Cr_3Ni_2Si(C,N)$), σ-phase. Additionally, two different oxides are found: Al- and Si-oxide.

The nucleation sites and shapes of the precipitates at 750°C are found to be similar to 650°C. Only a difference in the precipitates size is found, which is significantly larger at 750°C compared to 650°C. Especially the presence of **σ-phase** is more significant at 750°C compared to 650°C. In Figure 15 (A) a significant amount of σ-phase is observed in steel aged at 750°C for 1,000h. Its mean size is 1.73µm. Similar to the 650°C aged samples, also in 750°C samples an elongated cluster of primary **Z-phase** precipitates is often observed, as shown in Figure 15(A-2). A TEM micrograph of the specimen aged for 1000h at 750°C taken from a carbon extraction replica is shown in Figure 15 (B). The large precipitates in Figure 15(B-1) are **Nb(C,N)** with a diameter of 145nm.

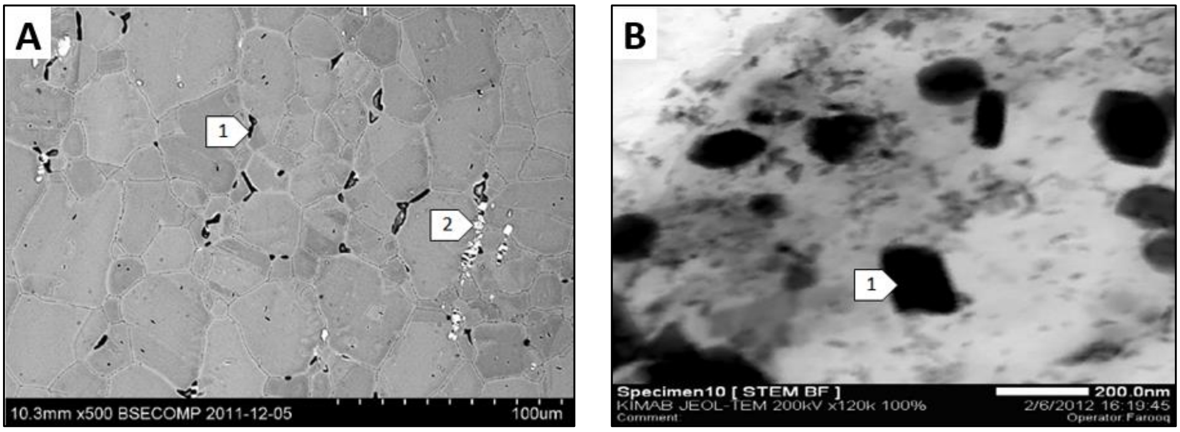

Figure 15: SEM image of 750°C/1,000h (A) and TEM image of 750°C/1,000h (B) aged sample. A-1: σ; A-2: primary Z-phase; B-1: Nb(C,N).

After 10,000h at 750°C, a $M_{23}C_6$ film along the grain boundaries is observed, as it can be seen in Figure 16.

The evolution of the phase fraction and mean radii of the $M_{23}C_6$ and σ-phase precipitates is shown in Figure 17. Both precipitates show an increase of phase fraction with increasing ageing time until 10,000h. Similar observations are made for the evolution of the mean radii of σ-phase, but not for $M_{23}C_6$ where the mean radii remain constant between 3,000 and 10,000h.

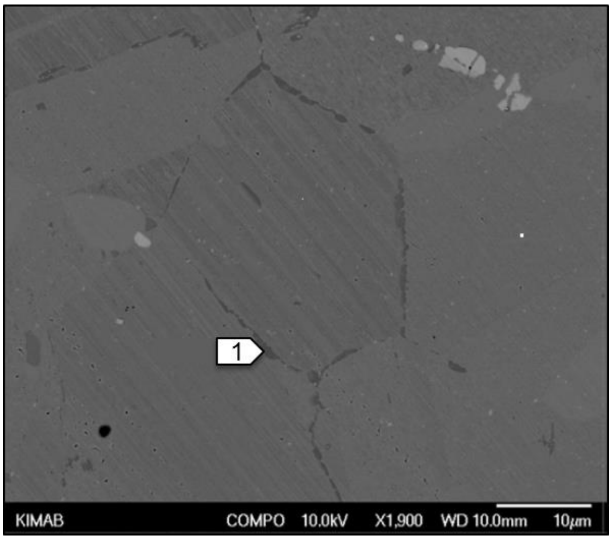

Figure 16: $M_{23}C_6$ (1) precipitates at grain boundaries at 750°C after 10,000h.

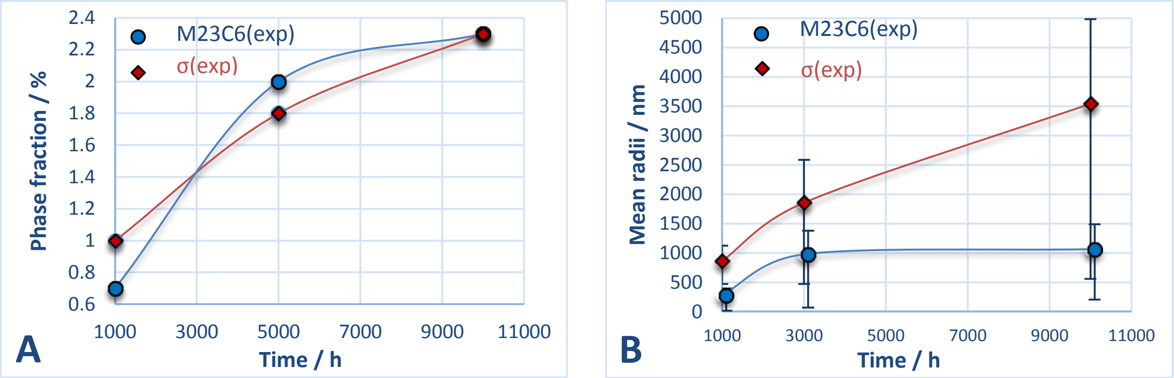

Figure 17: Phase fraction (A) and mean radii (B) of $M_{23}C_6$ and σ-phase at 750°C.

5.1.3 Precipitates composition

The chemical compositions of the precipitates are investigated by TEM-EDS and SEM-EDS. It has to be mentioned that the TEM-EDS measurements are performed on carbon replicas where the accuracy is higher compared to SEM-EDS. The SEM-EDS technique is more suitable for larger precipitates like primary Z-Phase and σ-phase where the influence of the surrounding matrix is lower. The SEM-EDS investigation of smaller precipitates like $M_{23}C_6$ and η-phase have to be treated with caution.

The TEM-EDS and SEM-EDS analyses, as shown in Figure 18 and Figure 19 respectively, depict a strong scattering of the precipitates composition as well as differences in the composition between 650°C and 750°C aging temperatures. However, some observations can be made. Looking at the TEM-EDS results of $M_{23}C_6$ in Figure 18, it can be seen that chromium (≈80%) is the main element and that niobium content decrease (from ≈15% to almost 0%) with increasing ageing time. When Nb(C,N) is analysed, it can be seen that niobium (≈60%) is the main element and that chromium content is decreasing (from ≈30% to smaller than 10%) with increasing ageing time. The main elements of the Z-phase (secondary) are niobium (50 – 60%) and nickel (20-30%). The main elements of the η-phase are chromium (40-50%) and nickel (30-40%).

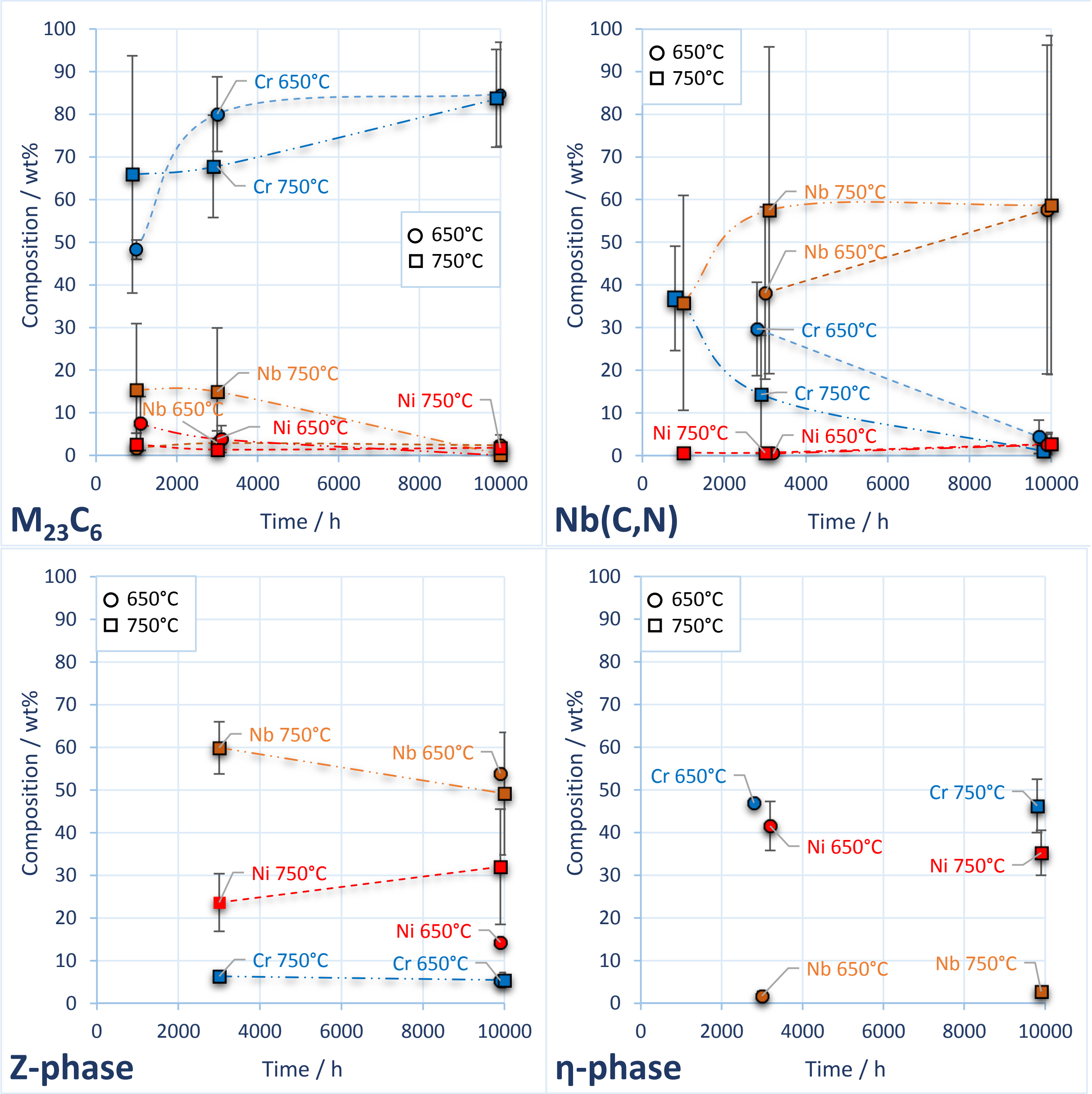

Figure 18: Chemical composition (wt.%) of precipitates measured by TEM-EDS.

Looking at the SEM-EDS results of the Z-phase (primary) in Figure 19, it can be seen that the main elements are niobium (up to 65%), chromium (10-30%) and nickel (5-15%). The composition of the σ-phase seems to be constant during the whole ageing time, it is ≈40-45% chromium and ≈10% nickel. The SEM-EDS analysis of the $M_{23}C_6$ and η-phase has to be treated with caution, since these precipitates are small and the influence of the surrounding matrix becomes large.

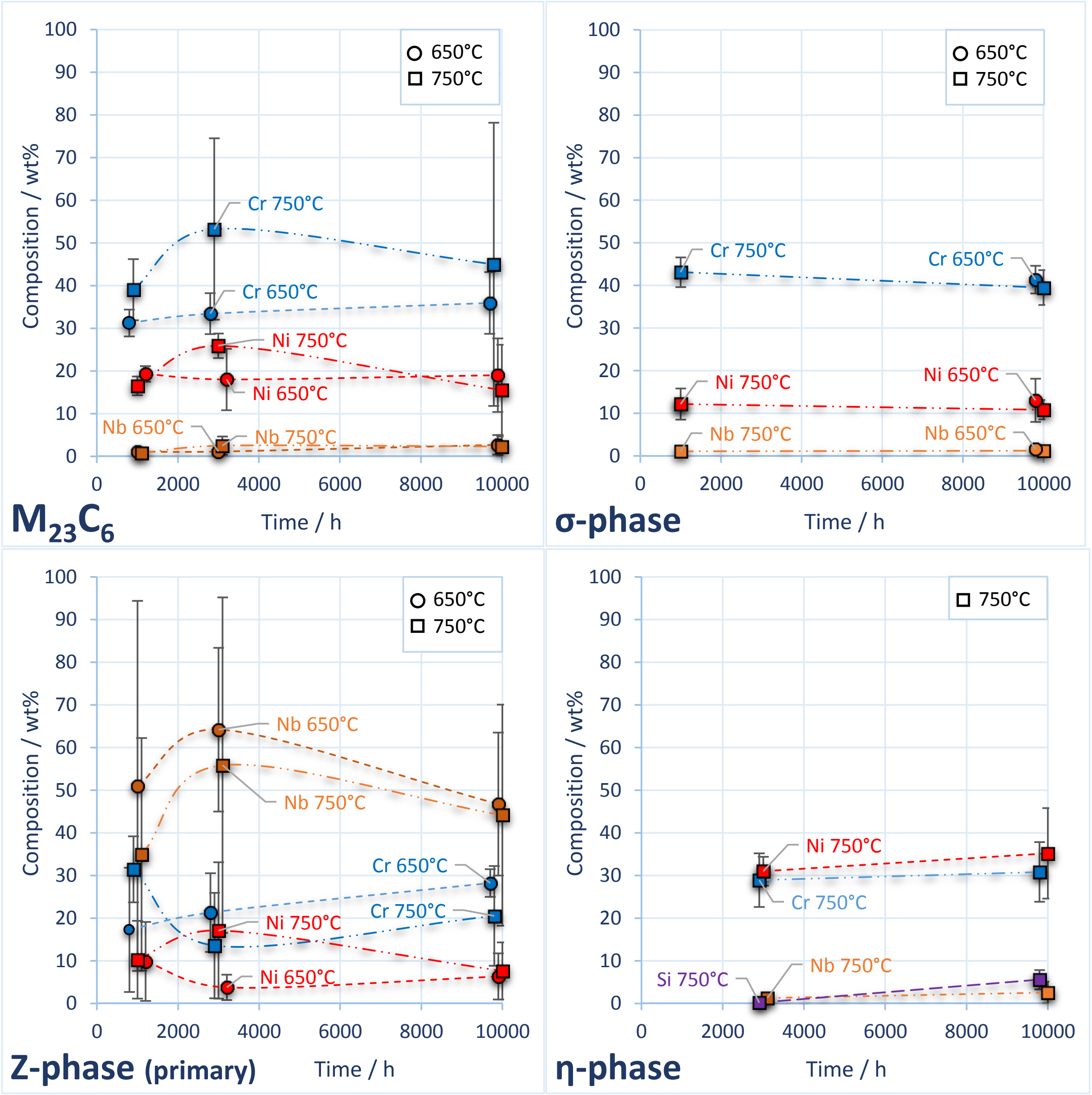

Figure 19: Chemical composition (wt%) of precipitates measured by SEM-EDS.

5.1.4 Discussion

Samples aged at 650 and 750°C for 1,000, 3,000 and 10,000h reveal five different precipitates: Z-phase, $M_{23}C_6$, Nb(C,N), η ($Cr_3Ni_2Si(C,N)$), σ-phase. Additionally to that, two different oxides are found: Al- and Si-oxide. A summary of all observed precipitates is presented in Table 8. Most of these precipitates, except η ($Cr_3Ni_2Si(C,N)$), are found in previous published investigations [32]–[34], [36]–[38]. A summary of these published investigations can be found in the literature review in chapter 3.2.1 on page 10 - 14.

Table 8: Summary of different observed precipitates over the ageing treatment at 750°C.

Phase	1,000h	3,000h	10,000h	Shape	Nucleation	Main chem. elements
Primary Z-phase	(≈)	(≈)	(≈)	IR	GI, GB	Nb, Cr, Ni
Secondary Z-phase	(+)	(++)	(+++)	EL	GI	Nb, Ni, Cr
$M_{23}C_6$	(+)	(++)	(+++)	EL, CU	GB, GI	Cr
Nb(C,N)	(+)	(++)	(+++)	RD, CU	GI	Nb, Cr, Ni
η-phase	(+)	(++)	(+++)	EL, RD	GB, GI	Cr, Ni, Nb
σ-phase	(+)	(++)	(+++)	IR	GB	Cr, Ni, Nb

(+) indicates an increasing precipitate diameter during ageing and (≈) diameter remains constant.
IR: Irregular; EL: Elongated; CU: Cubic; RD: Round; GI: Grain interior; GB: Grain boundary.
Similar results are observed at 650°C, whereas the diameters of most precipitates were smaller, especially of the σ-phase.

The ***η-phase*** requires a more detailed discussion. The chromium- and silicon-rich η-phase is identified in [37] as M_6C and in [32], [36], [38] as G-phase. The high silicon-content, fcc structure and lattice spacing makes it difficult to distinguish between η-phase, M_6C and G-phase. However, in [46] it is reported that the silicon-content of 14 wt% in G-phase is larger than in η-phase and separates the η-phase from the G-phase. Figure 19 shows that the silicon-content of the η-phase is smaller than 10wt%. This confirms the suspicion that the chromium-, nickel- and silicon-rich phase in this thesis is more likely a η-phase and not a G-phase. Furthermore, both phases, $M_{23}C_6$ and η-phase contain carbon, as a result the contrast of $M_{23}C_6$ and η-phase in the BSD micrographs is similar. In the case of the G-phase, which does not contain carbon, the BSD contrast should be brighter, which is not observed in the investigations. Considering all these findings, it is assumed, that the chromium-, nickel- and silicon-rich phase in this thesis is a η-phase and not a G-phase. Pettersson [46] studied a 20Cr-25Ni-4.5Mo steel. After ageing at 850°C for 5 and 3,000h the η-phase composition (wt%) was 25-28Cr, 25-35Ni, 25-31Mo, 6-8Fe, 4.2-7.4Si. Except the molybdenum content, the results are in good agreement with the present observations. Since the molybdenum is not present in the investigated steel, there is no surprise that no molybdenum is present in the η-phase precipitates.

The presence of ***Z-phase*** is natural due to the high stability of this phase when niobium is present in the steel. Several micrometre large primary Z-phase particles are found in all investigated samples. These primary Z-phase particles are randomly distributed (no specific nucleation sites) and have an irregular shape. Often primary Z-phase particles are found to form an elongated cluster, as can be seen in Figure 15(A-2) on page 37. It is assumed that the large primary Z-phase have a detrimental effect on the material properties, it accelerates the initiation of fatigue and especially corrosion-fatigue cracks [35]. Furthermore, the Z-phase contains a lot of niobium as can be seen in Figure 18 and Figure 19. Since niobium is an important solid solution hardening element [7], it is assumed that high phase fraction of Z-phase have a detrimental effect on the solid solution hardening. Additionally to the large primary Z-phase, small Z-phase precipitates of a diameter of several nanometre are found inside the grains. These small Z-phase precipitates are secondary precipitates, which form during the thermal exposure and are assumed to positively contribute to the creep strength, acting as obstacles against movement of dislocations. Figure 18 on page 40 shows that the Z-phase contains significant amounts of nickel (up to 30%Ni). This is not common for the Z-phase. However, less data about EDS analysis of Z-phase in the present steel is found in the literature which supports this high amount of nickel.

The ***σ-phase*** precipitates are found to nucleate mostly on the grain boundary triple points. This is in agreement with [27] where it is reported that the σ-phase initially nucleates on grain boundary triple points, then on grain faces and afterwards on incoherent twin boundaries and intragranular inclusions. A higher presence of σ-phase at 750°C compared to 650°C is observed. This is easily explained by a higher diffusion at 750°C than at 650°C. Compared to all other precipitates, the σ-phase was observed at late ageing times. There are at least three reasons for the slow kinetics of the σ-phase [31]: (i) σ-phase does not contain carbon and nitrogen, as a consequence the σ-phase starts to form after the carbides and nitrides are formed; (ii) the complex crystal structure (TCP) which is very different from the parent austenite matrix; (iii) σ-phase contains a lot of substitutional elements which have a slow diffusion. Considering the composition of the σ-phase, a chromium content of 40-45(wt.%) and a nickel content of 10-15% is observed, see Figure 19. This is in good agreement with investigations in [36] where a similar composition is observed.

The ***$M_{23}C_6$*** precipitates are one of the most dominant precipitates in the investigated steel. At early ageing times they become visible on grain boundaries and afterwards at twin boundaries and slip bands. At 750°C a film of $M_{23}C_6$ precipitates along grain boundaries is observed, which is assumed to be detrimental for the creep properties (can cause grain boundary sliding).

Similarly to Z-phase, the presence of ***Nb(C,N)*** precipitates is natural due to the high niobium content. According to previous studies [27], [28] it is believed that Nb(C,N) at 650°C and 750°C is a transient phase which gradually transforms to Z-phase.

When the chemical composition of the precipitates in Figure 18 is analysed, a strong scattering of the precipitates composition (especially of Nb(C,N)) can be observed. In the case of Nb(C,N) the niobium content varies between 20 and 95%. One possible explanation for this scatter may be caused by a particularly swapping of Nb(C,N) and Z-phase precipitates. The analysed Nb(C,N) with high amount of niobium is probably a Nb(C,N), whereas the analysed Nb(C,N) with low amount of niobium is probably a Z-phase. However, both precipitates, Nb(C,N) and Z-phase, have often a similar shape, contain high amount of niobium and chromium, that makes it difficult to distinguish between them. Therefore, the precipitation calculation is an helpful tool to study the evolution of Z-phase and Nb(C,N) precipitates.

5.1.5 Summary

Microstructure investigations of austenitic steel 25Cr-20Nr-Nb-N are carried out for thermally aged samples at 650 and 750°C for 1,000h, 3,000h and 10,000h. For the investigations, LOM, SEM and TEM techniques are used. The investigations (LOM, SEM and TEM) are carried out at the KTH Stockholm, whereas the evaluations of the experimental results is done by the author himself and partially also in collaboration with the KTH Stockholm. The experimental results are summarized as follows:

- Five different precipitates Z-phase, $M_{23}C_6$, Nb(C,N), η ($Cr_3Ni_2Si(C,N)$), σ-phase and two different oxides Al- and Si-oxide are experimentally found.
- The $M_{23}C_6$ precipitates are found at early ageing times at grain boundaries and after longer ageing times additionally at twin boundaries and slip bands. At 750°C the grain boundaries are particularly covered by a film of $M_{23}C_6$ precipitates.
- Two different types of Z-phase are found. The larger one, having a diameter of several micrometre, is assumed to be a primary one formed during solidification. The smaller one, having a diameter of several nanometre, is assumed to be a secondary one formed during thermal exposure.
- The σ-phase precipitates are found mostly on grain boundary triple points. Samples aged at 750°C have a higher amount of σ-phase than samples aged at 650°C.

The results of microstructure investigations can be used to setup and evaluate the precipitation calculation in order to understand the precipitation kinetics in the austenitic steel. Especially, the experimental findings about the precipitation kinetics of the η-phase are used to implement a new phase "Cr_3Ni_2SiN" in the MatCalc thermodynamic database [74].

5.2 Thermodynamic and Thermokinetic Calculations

5.2.1 Equilibrium and Scheil Calculations

A thermodynamic equilibrium calculation predicts the equilibrium phase fractions versus temperature after infinite long exposure time.

When all existing phases are considered for the MatCalc equilibrium calculation, the Cr_2N phase becomes stable at the expense of η-phase. This condition represents in a wrong way the equilibrium phase condition in the present austenitic steel. In order to show the influence of Cr_2N on the residual equilibrium phases, two kinds of equilibrium calculations are performed, one with and another one without Cr_2N phase, as illustrated in Figure 20. When Cr_2N is considered (Figure 20(A)), MatCalc predicts eight different equilibrium phases in the temperature range between 400 and 1600°C: liquid, austenite as matrix phase, Nb(C,N), Z-phase, $M_{23}C_6$, Cr_2N, σ-phase and G-phase. Nb(C,N) is stable between 1000 and 1300°C, Z-phase up to 1240°C, $M_{23}C_6$ up to 1000°C, Cr_2N up to 870°C, σ-phase up to 820°C, G-phase up to 480°C. When Cr_2N is suspended, then the η-phase becomes stable (up to 780°C) and G-phase unstable, see Figure 20(B).

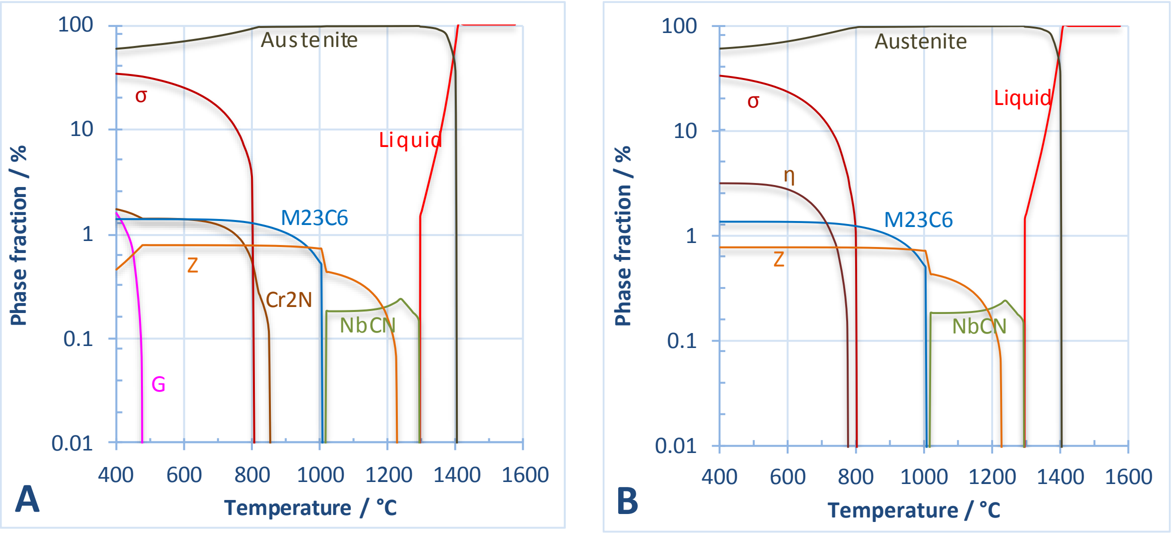

Figure 20: Equilibrium phases with Cr_2N (A) and without Cr_2N (B).

In Table 9 the phase fractions of equilibrium phases (when Cr_2N is suspended) at the relevant temperatures of 650°C and 750°C are presented. It can be seen that the most dominant phase at 650°C is the σ-phase having a phase fraction of 19.1%, whereas at 750°C it is 7.2%. The η-phase shows also a strong decrease of phase fraction between 650 and 750°C. The phase fractions of Z-phase and $M_{23}C_6$ do not change significantly between 650 and 750°C.

Table 9: Equilibrium phase fractions (%) at 650°C and 750°C.

	Z	**$M_{23}C_6$**	**σ**	**η**
650°C	0.8	1.4	19.1	2.3
750°C	0.8	1.3	7.2	0.6

Scheil-calculations [68]–[70] are performed to investigate the effect of segregation processes during solidification on the formation of the precipitates. Compared to the equilibrium calculation, the Scheil-calculation is a series of separate equilibrium calculations at different temperatures. As a result, the Scheil phase consists of many layers (each layer is calculated by equilibrium calculation) which have different compositions. The diffusion of substitutional elements between the layers is frozen (due to Scheil-Guliver assumption of very slow and therefore negligible diffusion in solid phase), whereas the diffusion of interstitial elements like carbon and nitrogen is assumed to be highly mobile in liquid phase as well as in solid phase.

The Scheil-calculation predicts four phases (primary phases) during the solidification: liquid, austenite, Nb(C,N) and Z-phase, see Figure 21. Liquid is stable down to 1236°C (3% liquid phase fraction) which is more than 50°C lower compared to equilibrium. This phenomenon is caused by segregation in the liquid phase during solidification. The calculated chemical composition and phase fraction of the primary Nb(C,N) and Z-phase at 3% liquid phase fraction (1236°C) is presented in Table 10. The phase fraction of the primary Z-phase is almost ten-times larger than the phase fraction of primary Nb(C,N), which indicates that the primary Z-phase is the most dominant primary phase.

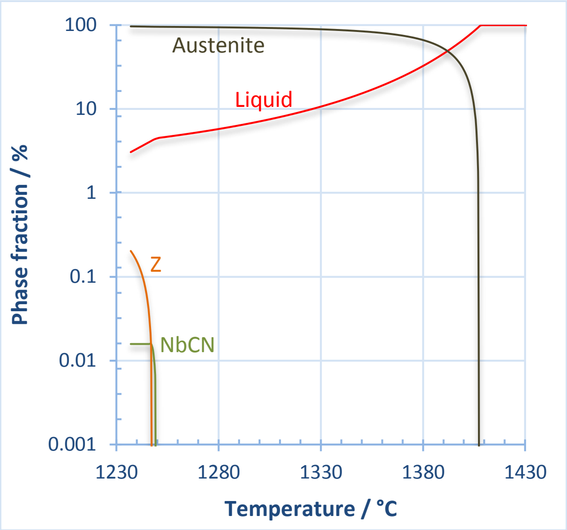

Figure 21: Primary phases according to Scheil calculation.

Table 10: Calculated chemical composition (wt%) and phase fraction (%) of primary Z-phase and Nb(C,N) at 3% liquid phase fraction.

Phase	Temp. °C	Phase fraction	Nb	C	N	Cr	Fe
Nb(C,N)	1236	0.02	88.95	8.57	2.47	-	-
Z	1236	0.22	58.67	-	8.17	28.57	4.58

5.2.1.1 Discussion

In thermodynamic equilibrium, six different precipitate phases are predicted by MatCalc in the temperature range between 400 and 1600°C: Nb(C,N), Z-phase, $M_{23}C_6$, Cr_2N, σ-phase and G-phase. Most of the phases, except Cr_2N, are experimentally found in the 25Cr-20Ni-Nb-N steel [32]–[34], [36]–[38]. In [36], creep exposed sample after 88,363h is investigated. In this long time creep exposed sample, which is assumed to be close to an equilibrium condition, no Cr_2N phase is found. Similar results are reported by Sourmail [27], who describes that Cr_2N is unlikely when Z-phase is present in austenitic steels. Therefore it is assumed that the Cr_2N phase is not a common phase in the 25Cr-20Ni-Nb-N steel. Based on that, equilibrium calculations without Cr_2N phase are carried out. When the Cr_2N is suspended, the η-phase becomes stable and G-phase unstable, see Figure 20(B). Suspending Cr_2N causes a higher chromium and nitrogen contents in the matrix, which in turn stabilizes the η-phase (=Cr_3Ni_2SiN). Since G-phase cannot take up the nitrogen, it is destabilized at the expense of η-phase. The system without the Cr_2N shown in Figure 20(B), is the most reasonable system to describe the equilibrium condition in the 25Cr-20Ni-Nb-N austenitic steel. All equilibrium phases shown in Figure 20(B) are also found experimentally.

The Scheil calculation predicts Nb(C,N) and Z-phase as primary precipitates phases during the solidification, as illustrated in Figure 21. The calculated chemical composition (wt.%) of the primary Z-phase is 58.67Nb-28.57Cr-4.58Fe-8.17N. This is in good agreement with the SEM measurements of the large Z-phase precipitates in Figure 19 on page 41. This observations supports the findings that the large Z-phase precipitates (bright precipitates in Figure 12 on page 36 and Figure 15 on page 37) are primary one which forms during the solidification.

5.2.1.2 Summary

Equilibrium and Scheil calculations of austenitic steel 25Cr-20Nr-Nb-N are carried out by the author. The experimental investigations are summarized as follows.

- The equilibrium system without the Cr_2N, is the most reasonable system which describes the equilibrium condition in the 25Cr-20Ni-Nb-N austenitic steel.
- When Cr_2N is suspended, five different precipitates phases in the temperature range between 400 and 1600°C are predicted: Nb(C,N), Z-phase, $M_{23}C_6$, σ-phase and η-phase. All these phases are also found experimentally.
- The Scheil calculation predicts Nb(C,N) and Z-phase as primary precipitates phases during the solidification. Primary Z-phase is also found experimentally.

With these equilibrium and Scheil calculations, a basis is created for a better understanding of the stability- and transformation- of phases in the 25Cr-20Ni-Nb-N austenitic steel. Especially, the results of the Scheil calculation can be used as input data for the precipitation calculation.

5.2.2 Precipitation Evolution at 650 and 750°C

5.2.2.1 Solution Annealing

In Figure 22 the calculated precipitation evolution during the solution annealing (at 1230°C for 10min) is presented. The $M_{23}C_6$ particles are split depending on whether they are located at grain boundaries ($M_{23}C_6$.gb) or in the grain interiors ($M_{23}C_6$.gi). The primary Z-phase and Nb(C,N), denoted as Z(prim) and Nb(C,N)(prim), are used as input data, so they are already present before the solution annealing calculation. During the heating to the solution annealing temperature, several phases such as $M_{23}C_6$.gb, η-phase, Z-phase and Nb(C,N) precipitate. However, most of them dissolve before the solution annealing temperature is reached. Only primary Z(prim), Nb(C,N)(prim) and secondary Nb(C,N) are found during and after solution annealing. The phase fraction and mean radius of secondary Nb(C,N) after solution annealing at 1230°C and quenching are ≈0.08% and ≈20nm, respectively.

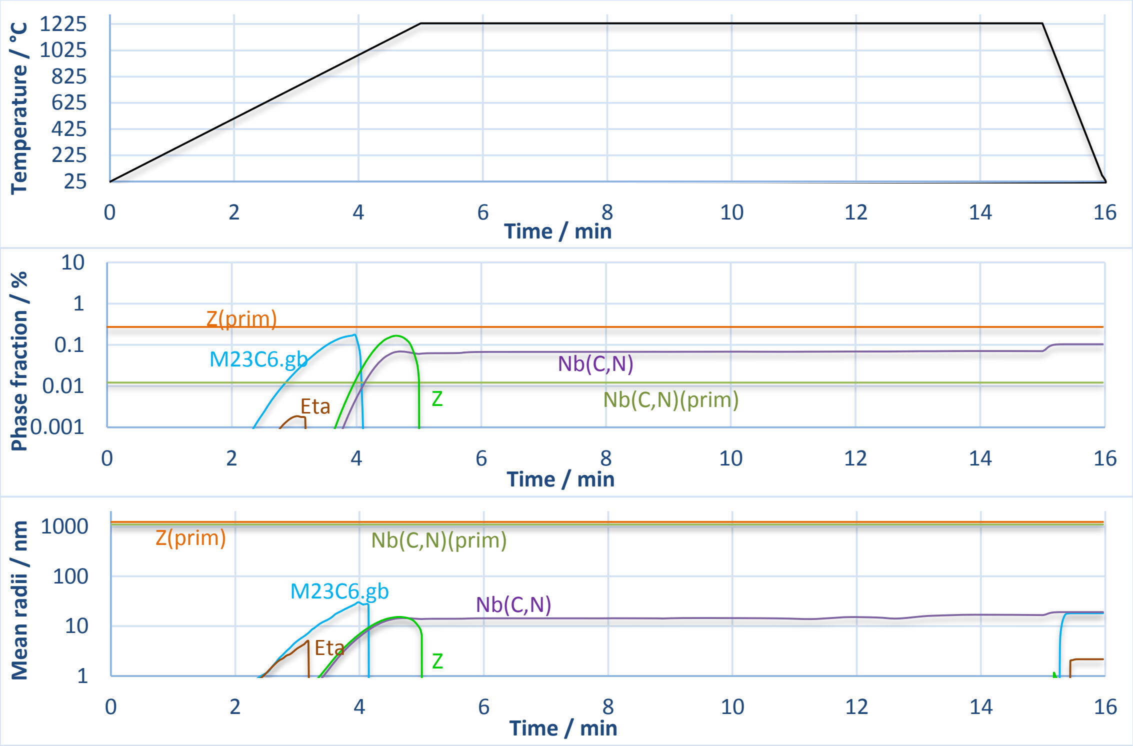

Figure 22: Evolution of phase fraction and mean radius of precipitates during solution treatment at 1230°C.

5.2.2.2 Service at 650 and 750°C

In Figure 23 the calculated precipitation evolutions during service temperatures of 650 and 750°C are given. The calculation shows the formation of five precipitates $M_{23}C_6$, σ, η, Z and G phase in addition to those already present after the solution treatment.

All precipitates (except Z(prim), Nb(C,N)(prim)) show an increase of phase fraction and mean radius with increasing ageing time. The phase fraction and mean radius of primary precipitates is constant during the ageing. The secondary Nb(C,N) which nucleate during the solution annealing starts to dissolve earlier at 750°C (<10,000h) than at 650°C (≈100,000h). A small fraction (≈0.003%) of G phase appears at 650°C but not at 750°C. The phase fraction and mean radius of $M_{23}C_6$.gb are higher than those of $M_{23}C_6$.gi. Considering the grain boundary precipitates, the most dominant phase is σ. The secondary Z phase fraction is increased in two stages. The first increase takes place during the first 100h of ageing and the second one during the dissolution of secondary Nb(C,N). Experimental mean radii and phase fractions of σ-phase and $M_{23}C_6$ are also displayed. When the number density of precipitates (Figure 23 (E, F)) is analysed, $M_{23}C_6$.gb and η-phase shows a gradual decrease in number density with increase of ageing time, indicating that coarsening is present. The secondary Nb(C,N) and G-phase shows an abrupt drop in number density, which means that dissolution is present.

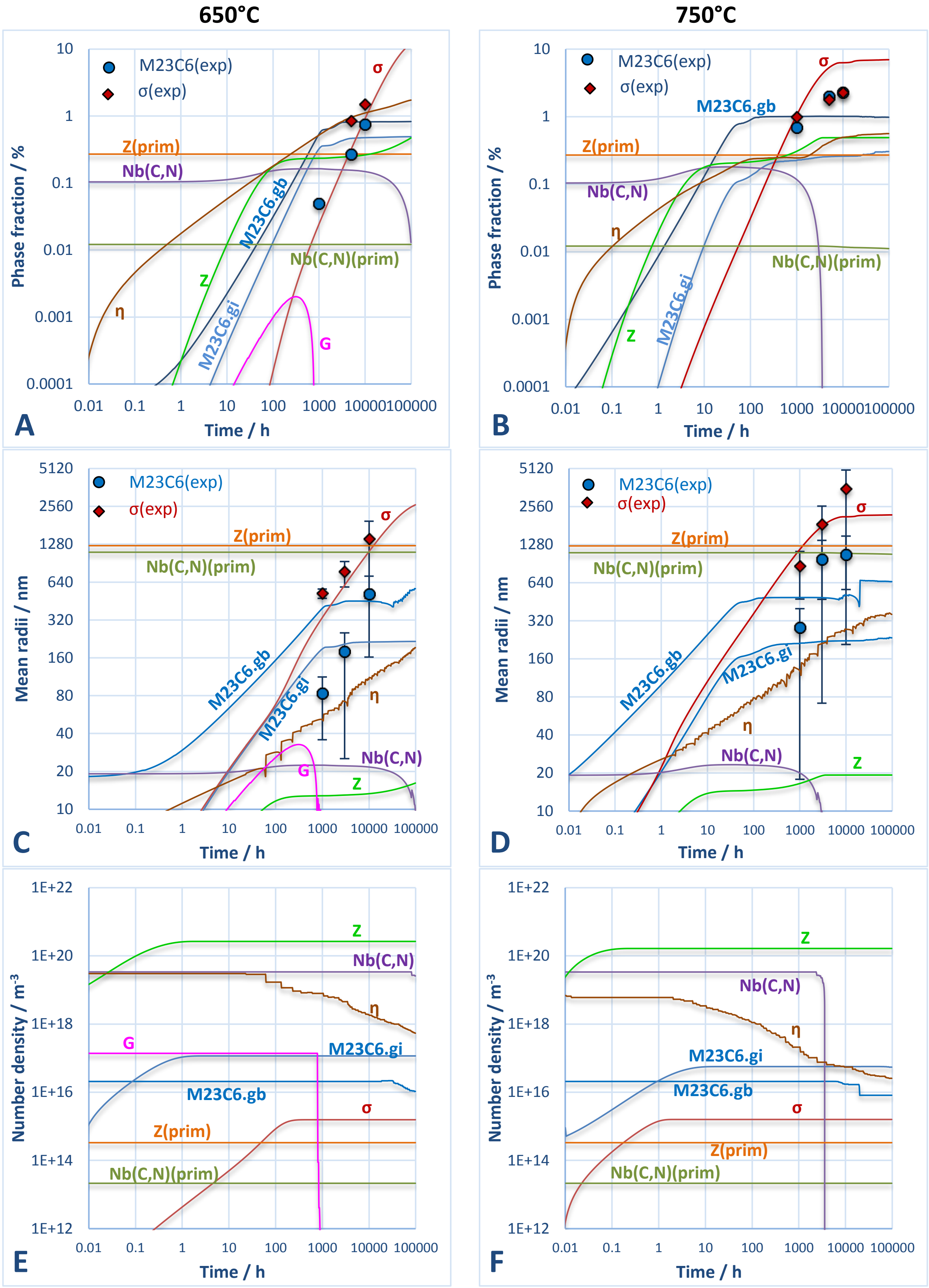

Figure 23: Precipitation evolution at 650°C (A, C, E) and 750°C (B, D, F) for 100,000h. gb: grain boundary; gi: grain interior.

Table 11 shows the calculated precipitates compositions at 650°C after 10,000h. At 750°C the precipitates compositions are similar.

Table 11: Precipitates compositions (wt%) at 650°C after 10,000h.

	Fe	C	Cr	Si	Ni	Nb	Mn	N
M23C6.gb	9.29	5.64	83.80	-	0.64	-	0.62	-
M23C6.gi	7.15	5.65	86.24	-	0.36	-	0.61	-
σ-phase	44.34	-	47.97	0.50	6.74	-	0.45	-
Nb(C,N)(prim)	-	8.82	-	-	-	88.65	-	2.53
Nb(C,N)	-	0.79	-	-	-	87.11	-	12.10
Z(prim)	5.56	-	27.50	-	-	58.39	-	8.55
Z-phase	6.57	-	26.46	-	-	58.21	-	8.75
η-phase	1.14	0.03	49.48	8.91	36.03	-	-	4.41

In Figure 24 the evolution of total carbon content in the matrix and the precipitates as a function of ageing time is presented. No significant differences in carbon content between 650°C and 750°C is observed; transformations are shifted to shorter times at 750°C. As can be seen, at the beginning most of the carbon is stored in the matrix. When $M_{23}C_6$.gb, $M_{23}C_6$.gi and Nb(C,N) starts to form (characterized by increasing carbon content), the matrix is depleted by carbon (from 0.05% to <0.01%C). Afterwards, when Nb(C,N) starts to dissolve (after1,000h at 650°C and 40h at 750°C), carbon is released which is used for further formation of $M_{23}C_6$.gb and $M_{23}C_6$.gi.

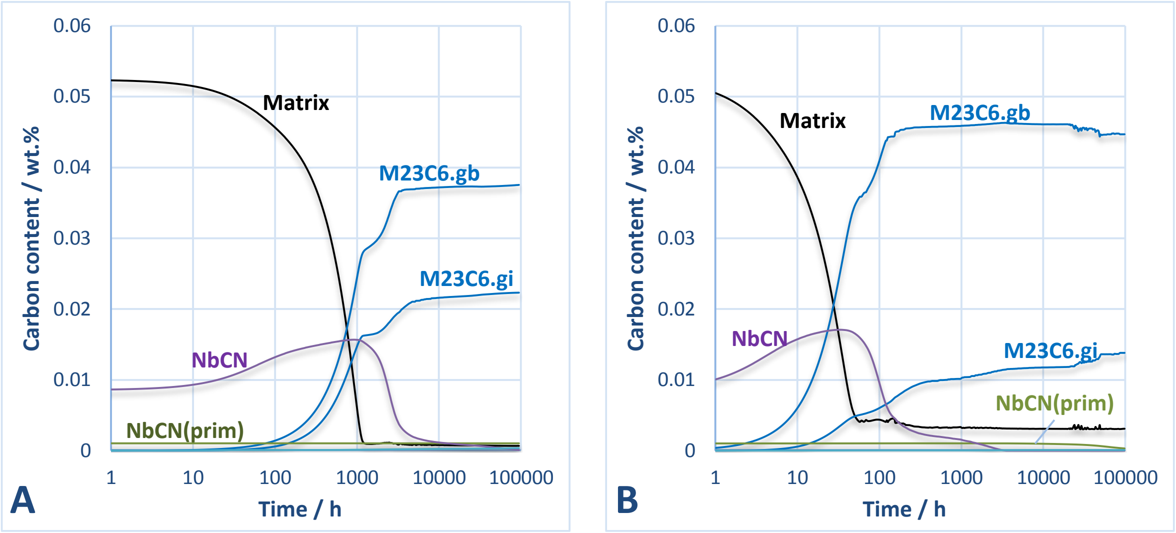

Figure 24: Total content (wt%) of carbon in matrix and precipitates during aging at (A) 650°C and (B) 750°C.

The obtained experimental data of η-phase, Z-phase and Nb(C,N) were not enough to verify the simulated precipitation evolution of these precipitates. Therefore, the verifications of these precipitates are made by the experimental data of Iseda et al. [36]. They measured the content of chemical elements in precipitates of a 25Cr-20Ni-Nb-N austenitic steel (HR3C) having a grain size of ≈60µm and exposed at 650°C for 10,000h. The results of their investigations, which are marked as "exp.", are presented in Figure 25. In order to compare their results with the present calculation, a precipitation calculation with a grain size of 60µm has been performed. The results are also shown in Figure 25. The curve marked as "Total" represents the calculated total content of nickel, chromium, iron or niobium in all precipitates. As can be seen in Figure 25(A) the calculated total content of nickel in the precipitates is in very good agreement with the experimental values. It can be seen that almost the whole nickel is stored in the η-phase, only negligible amount is stored in the $M_{23}C_6$.gb precipitates. Similar to the nickel content, the calculated total chromium content shows also a very good agreement with the experimental values, see Figure 25(B). As expected, most of chromium is stored into the $M_{23}C_6$.gb, $M_{23}C_6$.gi and η-phase. Smaller amounts of chromium are stored in the secondary and primary Z-phase. The total content of iron in the precipitates is presented in Figure 25(C). The most iron is stored in $M_{23}C_6$.gb, $M_{23}C_6$.gi. Close to the 10,000h, when σ-phase significantly starts to form, iron becomes stored in σ-phase. The total content of niobium in the precipitates is presented in Figure 25(D). The solid line represents the niobium content in the present austenitic steel with a dislocation density of $1x10^{12}$ m^{-2} and the dashed line with a dislocation density of $1x10^{10}$ m^{-2}. Initially, most of the niobium is stored in the primary Z-phase and secondary Nb(C,N). At later times, when the Z-phase starts to form, a significant amount of niobium becomes stored in the secondary Z-phase. The calculation with a dislocation density of $1x10^{10}$ m^{-2} shows very good agreement with the experimental results.

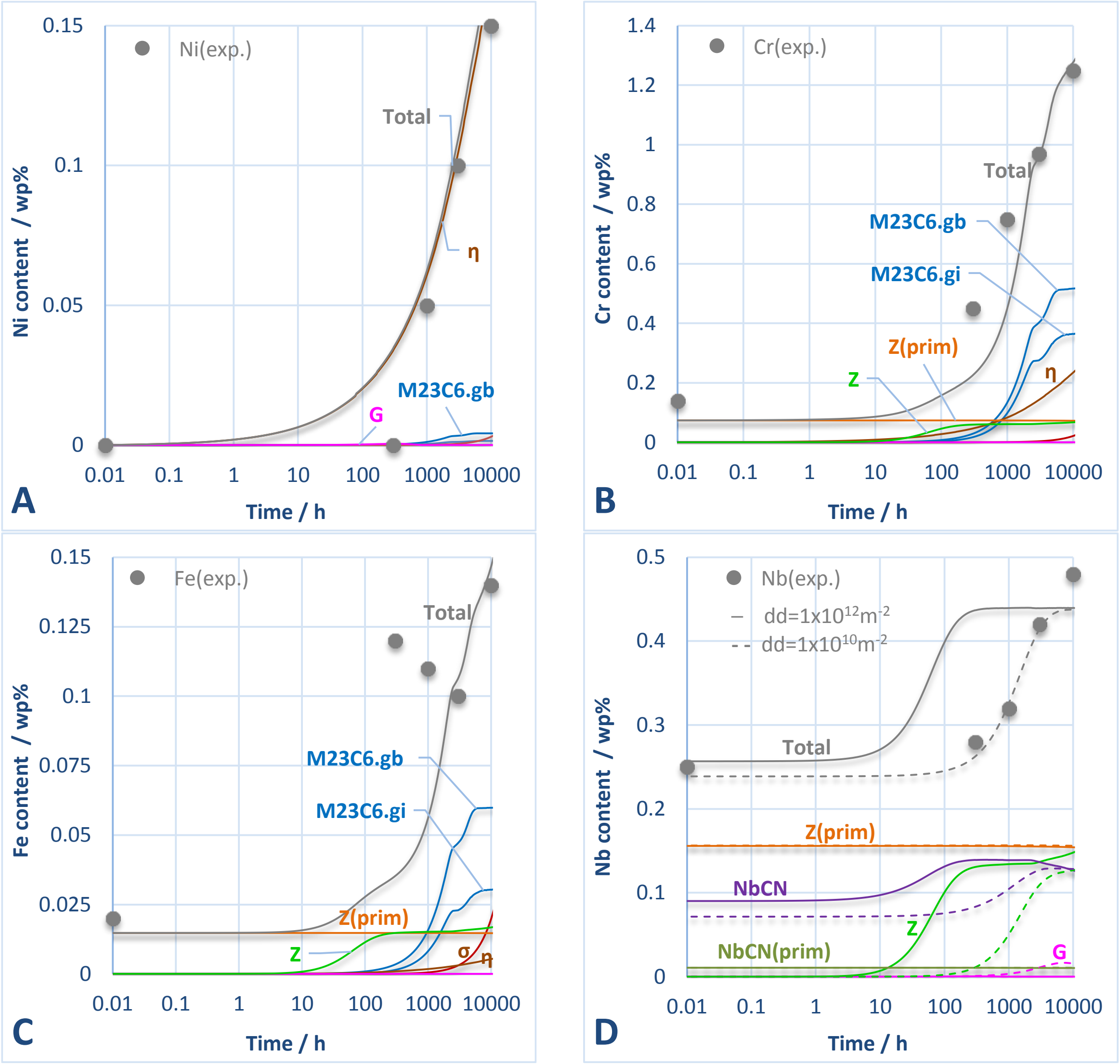

Figure 25: Total content (wt.%) of (A) nickel, (B) chrom, (C) iron and (D) niobium at 650°C and 60µm grain size; dd: dislocation density.

5.2.2.3 Discussion

The microstructure of the 25Cr-20Ni-Nb-N austenitic steel has been investigated by many workers over the last years. The disagreements about the identification of the Si-rich phase (η-, G- and M_6C) are still present. In order to understand the precipitation evolution as well as the interactions between the precipitates, a simulation of the precipitates evolution is necessary. In this chapter the precipitation evolution during long term ageing at 650 and 750°C is explained and discussed in detail. The precipitation process (nucleation, growth and coarsening), interactions between the precipitates, as well as the influence of some microstructure parameters such as dislocation density are explained.

By analysing the micrographs and experimental results from the literature, it was found that the $M_{23}C_6$ precipitates are mostly present at the grain boundaries, only at long ageing times they start to nucleate inside grains on the twin boundaries and slip bands. Since the twin boundaries and slip bands as nucleation sites are not available in MatCalc, a decision must be taken as whether or not to consider the $M_{23}C_6$ inside grains. In order to find a $M_{23}C_6$ setup for the MatCalc, which describes the evolution of $M_{23}C_6$ in most reasonable way, it was decided to create two populations of $M_{23}C_6$ in MatCalc: $M_{23}C_6$.gb ("gb" refers to grain boundary) and $M_{23}C_6$.gi (refers to grain interior). As nucleation sites for the $M_{23}C_6$.gi, the subgrain boundary corners are chosen. As a consequence, the phase fraction and mean radius of $M_{23}C_6$.gb are higher than those of $M_{23}C_6$.gi, shown in Figure 23(A, B). A similarity is qualitatively observed in the experimental investigation. So this approach of using the subgrain boundary corners as substitution for twin boundaries and slip bands is the most reasonable way to simulate correctly the $M_{23}C_6$ evolution. When comparing the simulated results of the $M_{23}C_6$.gb and $M_{23}C_6$.gi with experimental one in Figure 23, the results are satisfying. It seems that the simulations predict an earlier formation of $M_{23}C_6$.gb and $M_{23}C_6$.gi precipitates compared to the experiments. This deviation is probably caused by the measurement technique. The fraction of the $M_{23}C_6$ precipitates is measured by SEM, which is more suitable for large particles than for smaller particles. Accordingly, the small precipitates, which are present at earlier stages of ageing, are not detected by SEM. To verify this assumption, an additional calculation is performed and compared with the experimental results of Iseda et al. [36], see Figure 25(B). As can be seen, the simulation of the $M_{23}C_6$ evolution shows very good agreement with the experimental results. The increase of chromium content is directly related to the increase of phase fraction of $M_{23}C_6$. From this point of view, it seems that the simulation of $M_{23}C_6$.gb and $M_{23}C_6$.gi precipitates is correct. By analysing the evolution of $M_{23}C_6$.gb and $M_{23}C_6$.gi in Figure 23 it can be seen, that both precipitates show similar evolution in phase fraction and mean radius. At the beginning the phase fraction and mean radius increase at a constant number density for $M_{23}C_6$.gb and an increasing number density for $M_{23}C_6$.gi, meaning that precipitates are growing. After ≈1,000h at 650°C and ≈40h at 750°C the carbon content in the matrix reaches a minimum, see Figure 24. As a result, the growth of the $M_{23}C_6$.gb and $M_{23}C_6$.gi is stopped and a first plateau of phase fraction and mean radius is created, see Figure 23. Immediately when the Nb(C,N) starts to dissolve and further carbon is released. As a consequence, the phase fraction and mean radius of $M_{23}C_6$.gb and $M_{23}C_6$.gi start to increase. Close to an ageing time of 100,000h a further increase of mean radius of $M_{23}C_6$.gb at a constant phase fraction is observed, which means that precipitates coarsen. Since the diffusion in the grain interior is lower compared to the grain boundary, no coarsening of $M_{23}C_6$.gi after 100,000h is observed.

The simulation of the evolution of ***σ-phase*** shows good agreement with experimental results, see Figure 23. The σ-phase shows a very slow kinetics, it is the last precipitate to nucleate. This is also reported in [31]. Due to the faster diffusion, the formation of σ-phase starts earlier at 750°C compared to 650°C. This is also found experimentally, where less σ-phase is found at 650°C, whereas significant σ-phase formation is found after 1,000h at 750°C. The phase fraction after 100,000h at 650°C is higher compared to the same time at 750°C. This can be explained by the equilibrium phase fraction which decreases rapidly with higher temperature, see Figure 20 on page 46. In Figure 23 at 650°C the σ-phase shows a constant increase of phase fraction and mean radius, so growing is present. At 750°C the phase fraction and mean radius increase until ≈10,000h where a plateau is observed (equilibrium condition).

The ***secondary Nb(C,N)*** precipitates are the only one, except the primary precipitates, which are stable during the solution treatment at 1230°C, see Figure 22 on page 50. During the subsequent ageing the phase fraction and mean radius remain almost constant until the dissolution of the Nb(C,N) starts, see Figure 23 on page 52. Since the diffusion is higher at 750°C than at 650°C, the Nb(C,N) dissolve earlier at 750°C than at 650°C. The dissolution of Nb(C,N) may not be a surprise when the equilibrium plot in Figure 20 on page 46 is analysed. As can be seen, the Nb(C,N) is only stable at high temperature from ≈1000°C to 1300°C, this is more than 250°C higher than the ageing temperature of 750°C. When the Nb(C,N) starts to dissolve, a small amount of niobium, carbon and nitrogen is released. Niobium and nitrogen are used for the formation of the secondary Z-phase and carbon is used for the $M_{23}C_6$ formation. This can be seen in Figure 23 on page 52, where the phase fraction of the Z-phase and $M_{23}C_6$ increases when Nb(C,N) starts to dissolve. This is in agreement with findings in [27], [28], where it is reported that the Z-phase grows at the expense of MX (Nb(C,N)) precipitates in 20-25Cr austenitic steels. Furthermore, the present calculation confirms the assumption in [31] where it is assumed that the MC to $M_{23}C_6$ transformation can take place in several austenitic steels after long time exposure. In addition to the secondary Nb(C,N) precipitates, also ***primary Nb(C,N)*** are present. It is shown that the secondary Nb(C,N) precipitates dissolve in the present steel, therefore it would be expected that the primary Nb(C,N) also dissolve. However, no dissolution of primary Nb(C,N) during the ageing is observed, see Figure 23 on page 52. There are at least two reasons for the non-dissolution of the primary Nb(C,N): (i) it is well known that the diffusion along the dislocation (pipe diffusion) is higher compared to the matrix diffusion; the secondary Nb(C,N) are located on dislocation and the primary Nb(C,N) are randomly distributed inside the matrix; as consequence, the dissolution of the secondary Nb(C,N) occurs faster compared to the primary one; (ii) large precipitates dissolve more slowly compared to small precipitates; since the primary Nb(C,N) have a diameter of several micrometres and the secondary Nb(C,N) of several nanometres, the dissolution of secondary Nb(C,N) is faster.

An additional niobium-rich phase is the ***secondary Z-phase***. Similar to all other secondary precipitates (except Nb(C,N)), it dissolves during the solution treatment, see Figure 22 on page 50. Afterwards, when the ageing is applied, the Z-phase starts to form and grow on dislocations using chromium, niobium and nitrogen from the supersaturated matrix, see Figure 23 on page 52. When the matrix is depleted by niobium, the growth of the Z-phase stops. This happens after ≈100 and ≈10h at 650 and 750°C, respectively, see Figure 23 on page 52. Afterwards a plateau of phase fraction and mean radius appears. Close to 10,000h when the Nb(C,N) significantly starts to dissolve, niobium is released and the Z-phase starts to grow again. No coarsening of Z-phase up to 100,000h is predicted. Additional to the secondary Z-phase, the ***primary Z-phase*** is also present. As can be seen in Figure 23 on page 52, the phase fraction and mean radius of the primary Z-phase remains unchanged during the whole ageing treatment.

According to the experimental investigations, the nickel-rich ***G-phase*** is discussed to be more likely a η-phase than a G-phase, see chapter 5.1.4 on page 41. However, to clarify this assumption, the G-phase is taken into account for the precipitation calculation. The evolution of the G-phase is presented in Figure 23 on page 52. At 650°C ageing, a small fraction of G-phase appears, and immediately afterwards it dissolves, whereas at 750°C no significant G-phase fraction is predicted. The calculation supports the assumption that the nickel-rich phase is more likely to be a η-phase than a G-phase.

Additional to the $M_{23}C_6$.gb and σ-phase, a further dominant grain boundary precipitate is the ***η-phase***. The nucleation of the η-phase starts during the quenching from the solution annealing temperature. After quenching, the number of η-phase precipitates is about $3 x 10^{19} m^{-3}$, which is by far the highest amount compared to other grain boundary precipitates such as $M_{23}C_6$.gb ($2\ x 10^{16} m^{-3}$) and σ-phase ($2.5\ x 10^{11} m^{-3}$). As a result of this high number density, the interparticle spacing between the η-phase precipitates is low. When service is applied, the η-phase starts to grow, which causes a further decrease of η-phase interparticle spacing. Once the interparticle spacing is small enough that η-phase cannot grow anymore due to mutual obstruction, the η-phase precipitates simultaneously start to coarsen (characterized by decreasing number density) and grow (characterized by increasing phase fraction). This happens at 650°C close to 100h service time and at 750°C between 1 and 10h, see Figure 23 E and (F). In order to explain more in detail this simultaneously growing and coarsening of η-phase, a additional precipitation calculation is performed considering only the η-phase (all other precipitates were suspended). For the calculations, four different nucleation constants (NC) are applied: 1, $1x10^{-2}$, $1x10^{-4}$ and $1x10^{-6}$. These constants are used to decrease the number density of the η-phase. The results of the calculations are shown in Figure 26(A-C). As can be seen in Figure 26(A, B), the phase fractions and mean radii of η-phase is similar for all four nucleation constants. This is not the case for the number densities, as can be seen in Figure 26(C), where a lower nucleation constant causes a lower number density. This lower number density leads to a larger interparticle spacing and further on to a delayed start of coarsening (decrease of number density): the coarsening for NC=1 starts between 1 and 10h, for $NC=1x10^{-2}$ between 10 and 100h, for $NC=1x10^{-4}$ close to 1000h and for $NC=1x10^{-6}$ close to 10,000h. A schematic illustration of simultaneous growth and coarsening is shown in Figure 26(D). This kind of growth and coarsening at same time is not often present, but under specific conditions, like high number density of grain boundary precipitates. A further effect which causes simultaneous growth and coarsening is the increasing ratio between diffusion at grain boundary and inside grain, as shown in the thesis of Radis [75] by calculation of AlN precipitates evolution at 1000°C. This diffusion ratio may also contribute to the simultaneous growth and coarsening, but for the present case, the main reason is the high number density. The simultaneous growth and coarsening of η-phase is still present even after 100,000h exposure. The evolution of the η-phase seems to be very good predicted, see Figure 25(A) on page 55.

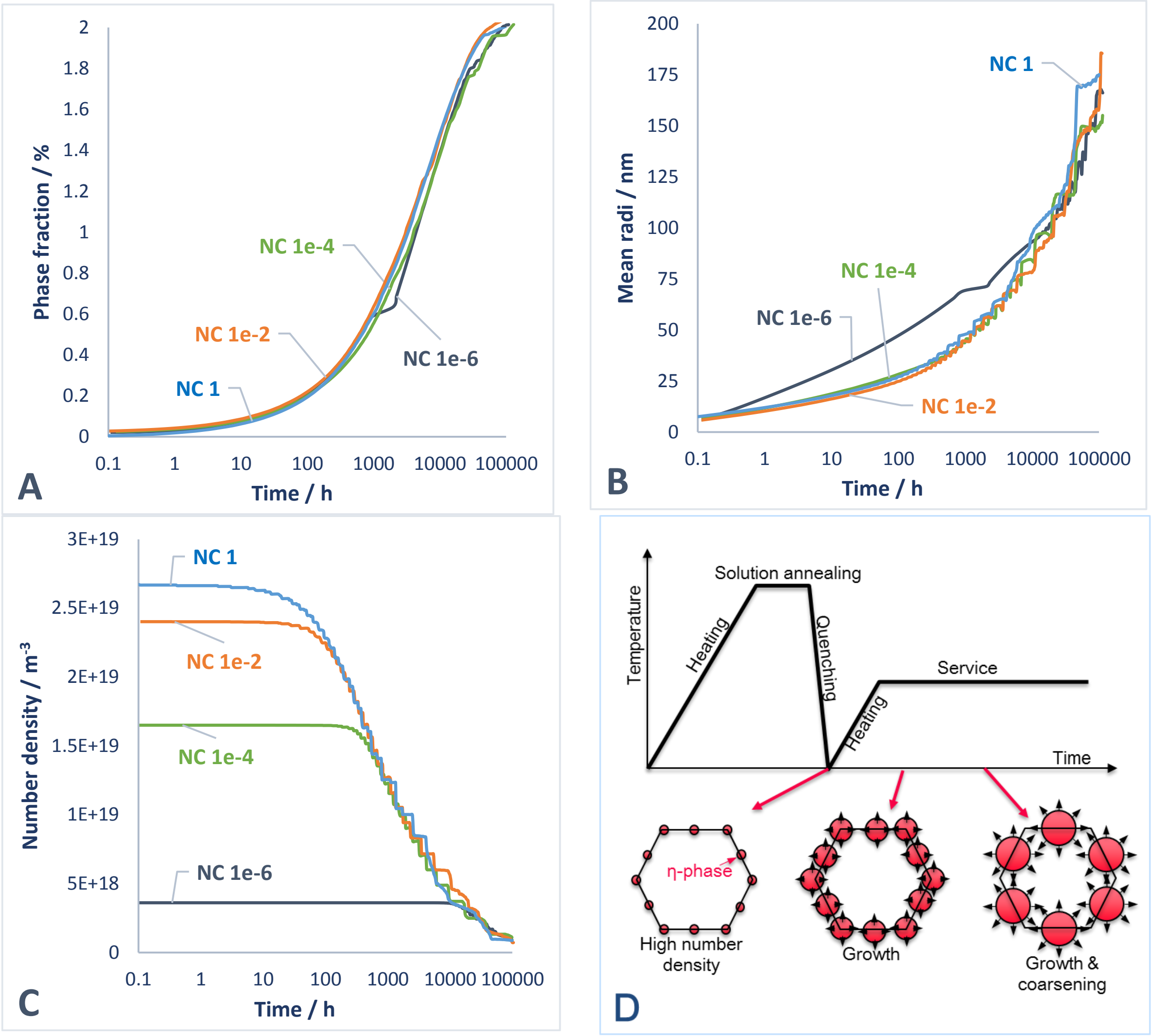

Figure 26: Influence of number of nucleation sites on (A) phase fraction, (B) mean radi and (C) number density of η-phase during service at 650°C. Schematic illustration of simultaneous growth and coarsening of η-phase (D).

In Figure 25(D) on page 55 the calculated niobium content in the precipitates is compared with the experimental results of Iseda et al. [36]. As can be seen, the dislocation density has a significant influence on the starting point of formation of the secondary Z-phase and Nb(C,N) precipitates. When the dislocation density is decreased from $1x10^{12}$ to $1x10^{10}$ m^{-2}, the formation of secondary Z-phase and Nb(C,N) is switched to later times. This does not apply for the primary Z-phase and Nb(C,N), which remain unchanged when the dislocation density is changed. The primary Z-phase and Nb(C,N) are randomly distributed, they are not located on the dislocation and as a result their evolutions are independent of the dislocation density.

5.2.2.4 Summary

Thermo-kinetic calculations of the precipitation evolution in the austenitic stainless steel 25Cr-20Ni-Nb-N are performed by the author with the help of the software MatCalc. The results are summarized as follows:

- For the precipitation calculations, eight precipitates are considered: $M_{23}C_6$, σ, primary Z, secondary Z, primary Nb(C,N), secondary Nb(C,N), η (Cr_3Ni_2SiN) and G. Furthermore, a multistage heat treatment of solution annealing and ageing at 650 and 750°C is applied.
- The precipitation calculation shows a good agreement with experimental results.
- The phase fraction of the $M_{23}C_6$ at the grain boundaries ($M_{23}C_6$.gb) is higher compared to the $M_{23}C_6$ inside grains ($M_{23}C_6$.gi).
- The σ-phase is found to be the most dominant phase on the grain boundaries.
- The secondary Nb(C,N) precipitates are found to dissolve during the ageing at 650 and 750°C. The released niobium, carbon and nitrogen is used for the formation of secondary Z-phase and $M_{23}C_6$ precipitates.

The results of the precipitation calculation contribute to a better understanding of the evolution and transformation of precipitates in a 25Cr-20Ni-Nb-N austenitic steel. With this calculation, a basis was created for the precipitation strength calculation in order to optimize the 25Cr-20Ni-Nb-N by modifying the chemical composition and heat treatment.

5.3 Creep Strength Calculations

For the 25Cr-20Ni-Nb-N steel, three main contributions to creep strength are assumed: from precipitates, from solid solution and from dislocations. These three contributions are analysed separately using the creep strength modelling approach of Sandström et al. [13]–[18], that is summarized in chapter 3.2.2 on page 17. Results from precipitation kinetics simulations (from chapter 5.2.2.2 on page 50) are used as input for calculating the precipitation hardening contribution. All results shown in this chapter, are obtained in collaboration with Prof. Sandström (KTH Stockholm) and further on published in [76].

5.3.1 Precipitation Hardening

The interparticle distances according to eq. (13), on page 21, are illustrated in Figure 27(A)-(B) and Figure 28(A)-(B) as a function of the ageing time at 650°C and 750°C, respectively. Eq. (13) does not take into account the influence of climb. The smallest interparticle spacing is observed for the secondary Z-phase (primary Z-phase is not considered). Small spacing is also found for secondary Nb(C,N) (primary Nb(C,N) is not considered) and at 650°C for Cr_3Ni_2SiN (η). However, at longer times, Nb(C,N) is transformed to Z-phase and disappears. In spite of the increase in volume fraction of η with ageing time, see Figure 23, its interparticle spacing increases at longer times due to the increase in particle radius and dissolution of small η particles. For Z-phase and Nb(C,N) on the other hand there is no increase in the interparticle spacing until Nb(C,N) starts to dissolve.

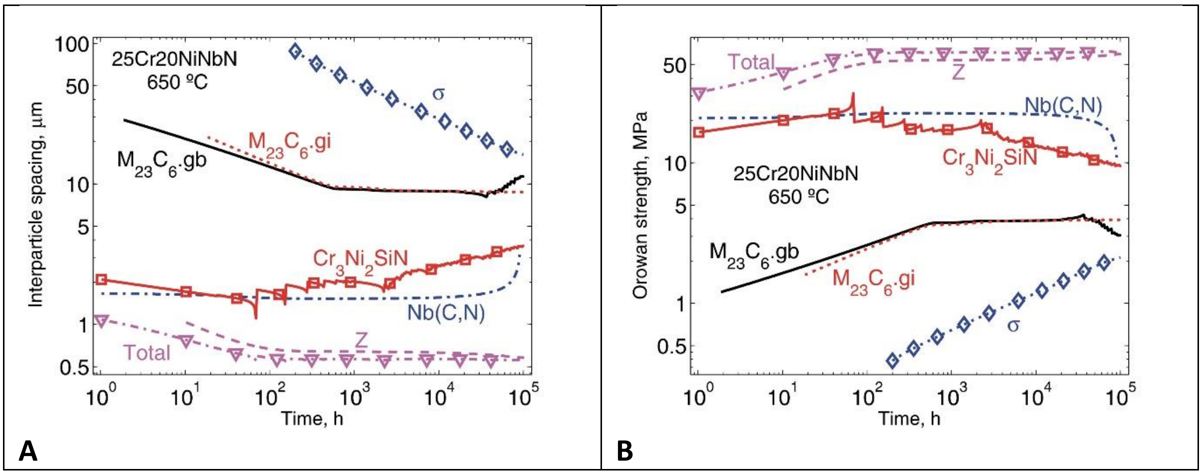

Figure 27: (A) Interparticle spacing, eq. (13) and (B) Orowan strength, eq. (12) versus time for 25Cr-20Ni-Nb-N at 650°C.

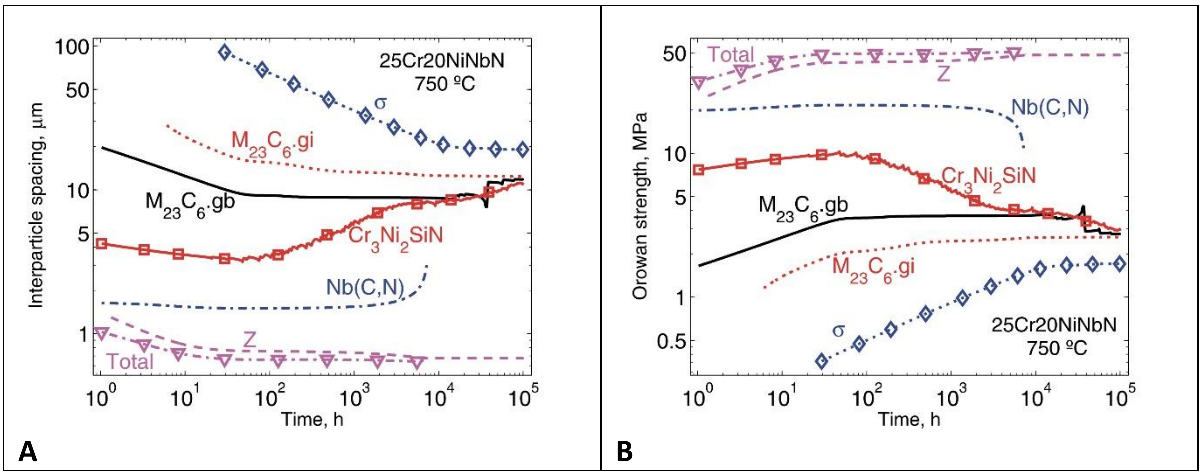

Figure 28: (A) Interparticle spacing, eq. (13) and (B) Orowan strength, eq. (12) versus time for 25Cr-20Ni-Nb-N at 750°C.

Figure 27(B) and Figure 28(B) show that the main contribution to the Orowan strength according to eq. (12), on page 21, comes from the Z-phase. In [77] it is reported that the elongated shape of precipitates decreases the interparticle spacing and further on increases the creep strength. To remind once again, for the simulation of secondary Z-phase and $M_{23}C_6$.gb precipitates a shape factor (relationship length/width of precipitate) of 3 is applied. The effect of this particle shape factor on the resulting creep strength turned out to be quite small following the procedure by Sonderegger et al. [78].

The interparticle spacing $L_{part\ tot}$ when all particles types are considered is shown in Figure 27(A), Figure 28(A) and marked as total. The total contribution to the Orowan strength $\sigma_{part\ tot}$ is illustrated in Figure 27(B), Figure 28(B) and marked as total. Again, it can be seen that the dominant contribution comes from the Z-phase at long times. At 100,000h the predicted Orowan strength is 56 MPa at 650°C and 50 MPa at 750°C.

When climbing is taken into account, the particle strength is reduced with increasing temperature and time, as illustrated in Figure 29. At times up to 10,000h at 650°C, the effect of climbing is small. However, at longer times at 650°C and particularly at 750°C, climbing strongly reduces the strength contribution. The reason is that at longer times, there is more time available for climbing and at a higher temperature the climbing is faster.

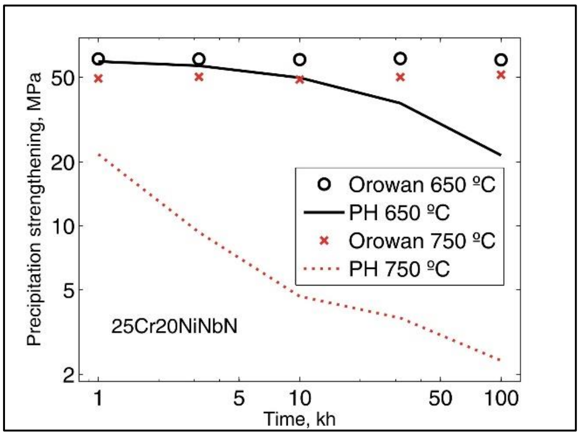

Figure 29: Particle strengthening for the material 25Cr20NiNbN versus creep time. The Orowan strength, eq. (12) is compared to the particle hardening (PH) when climb is taken into account, eq. (15).

5.3.2 Solid Solution Hardening

The modelling for the solid solution is shown in chapter 3.2.2.3 on page 24. There are two main elements contributing to the solid solution hardening: from niobium and from nitrogen.

The concentration of niobium solutes around an edge dislocation is presented in Figure 30. The distribution of Nb-solutes around a dislocation is highly localised. The maximum concentration can be more than a factor of 100 higher than the average solute content in the matrix. The maximum content decreases somewhat with increasing temperature. Fermi-Dirac statistics means that one atom can only be placed in one atomic position, which is not the case for Boltzmann statistics. However, there is only a small difference between the two types of statistics.

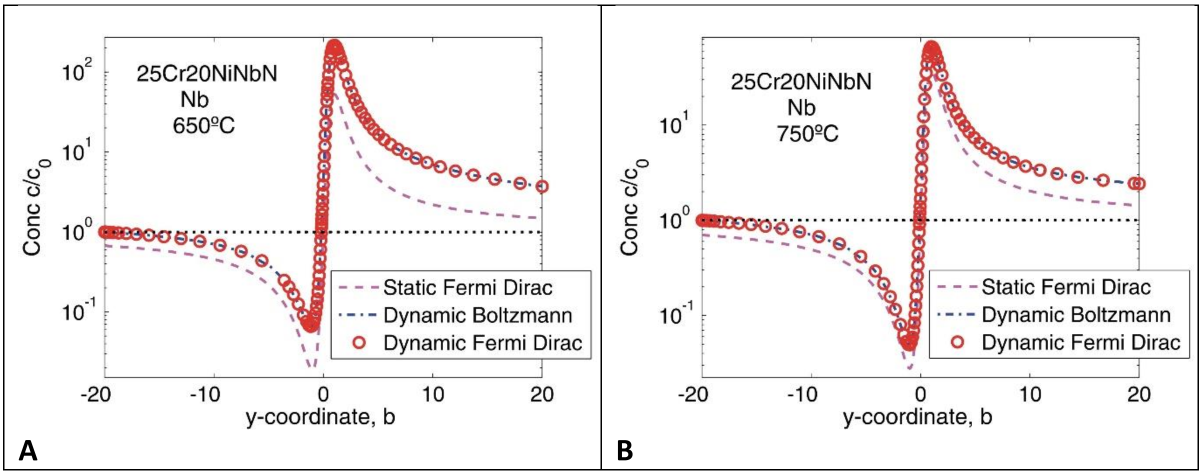

Figure 30: Concentration of niobium solutes around an edge dislocation A) at 650°C and B) at 750°C. The dislocation is either non-moving (static, eq. (23)) or climbing in the y-direction, eq. (24).

The maximum absolute solute concentration is given in Figure 31. In spite of the fact that the solute concentration in the matrix increases with temperature, the maximum concentration is reduced, since the drop in c/c_0 at the dislocation is faster.

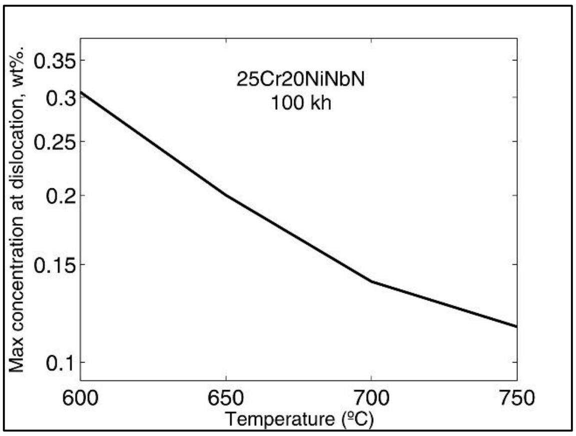

Figure 31: Maximum Nb-solute concentration solute at dislocation versus temperature for a creep time of 100 kh according to eq. (24).

The result for the solid solution hardening of niobium is shown in Figure 32(A). According to the precipitation computations, 0.0001 Nb at 650°C and 0.0008 Nb (wt.%) at 750°C remain in solid solution after 100,000h. The low amount of Nb in solid solution is the main reason for the small solid solution hardening effect, less than 1MPa. The solid solution hardening decreases when increasing temperature and time. In Figure 32, the equilibrium content of Nb in solid solution has been used. If the amount from the precipitation calculations is used instead, the magnitude of the solid solution hardening would be even smaller. Chromium, nickel and manganese have very small lattice misfit parameters (ε≈1% or less) [15] and the resulting solid solution hardening is negligible. It should be recalled that it varies exponentially with the misfit parameter.

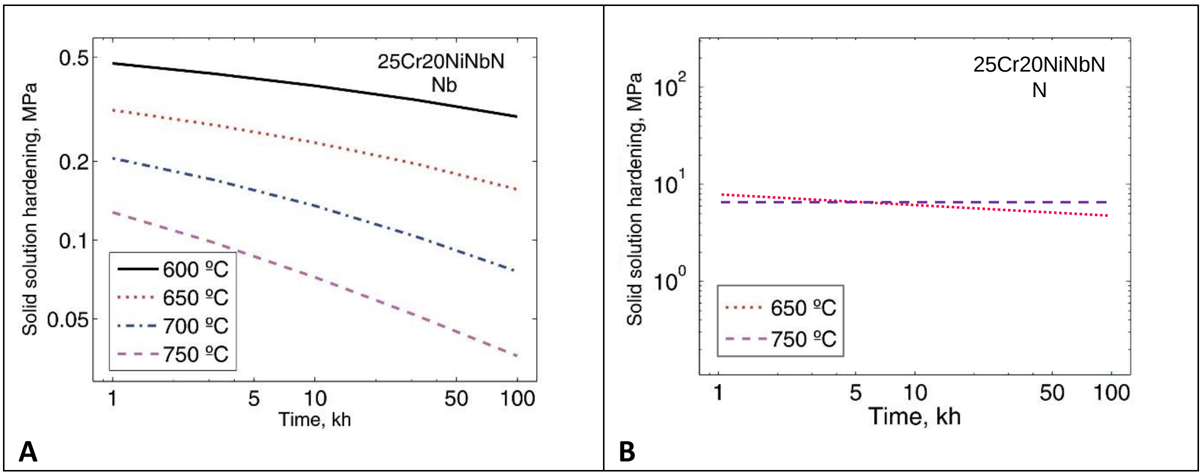

Figure 32: Solid solution hardening due to (A) Nb according to eq. (26) and (B) N according to eq. (29) versus creep time at different temperatures.

The result for the solid solution hardening of nitrogen is shown in Figure 32(B). The solid solution hardening effect from nitrogen is between 5 and 10MPa, and it is only weakly temperature and time dependent. In principle, carbon could also give a contribution to solid solution hardening, but the amount of carbon in solid solution is very small and the contribution to the creep strength is negligible.

5.3.3 Dislocation Hardening

The contribution from the dislocations to the creep strength σ_{disl} is derived from the minimum creep rate $\dot{\varepsilon}_{\min}$ according to eq. (9) on page 19. The minimum creep rate is in turn derived from the Monkman-Grant relation

$$\dot{\varepsilon}_{min} = \frac{C\varepsilon_R}{t_R} \tag{31}$$

where *C* is a constant of the order of unity, ε_R is the creep elongation at rupture and t_R the rupture time. Unfortunately, data for the creep elongation at rupture is not available. One approach is then to take the rupture elongation from a related steel. For example, 25Cr-20Ni (TP310) has a typical rupture elongation of a little less than 0.05 (5%) [79]. Since some creep rate data exist for 25Cr-20Ni-Nb-N [24], the product $C\varepsilon_R$ can be computed. The resulting values for the product vary between 0.02 and 0.07 in an essentially non-systematic way. The average value 0.04 has been used in the computations.

Alternatively, the creep rupture can be predicted taking creep cavitation into account. This has been done for other austenitic steels such 18Cr-10Ni (304), 17Cr-12Ni-Ti (321) and 17Cr-12Ni-2Mo (316) [80]. The analysis demonstrates that the Monkman-Grant and the cavitation give quite similar results. In the present the cavitation approach has not been chosen since the cavitation behaviour has not been quantified for the investigated steel 25Cr-20Ni-Nb-N. The contribution of the dislocation hardening to the total creep strength is shown in Figure 33.

5.3.4 Creep Strength

The total creep strength is obtained by adding the contributions from the different mechanisms according eq. (30) on page 26. The creep strength contributions are illustrated in Figure 33. The contribution from the dislocations, σ_{disl}, is the largest one, but precipitation hardening, σ_{PH}, and solid solution hardening from nitrogen, σ_{solN}, is also of great importance. Solid solution hardening from substitutional elements, σ_{sol}, is however, negligible. Since σ_{solN} is only weakly temperature and time dependent, its most important role is at high temperatures and long times.

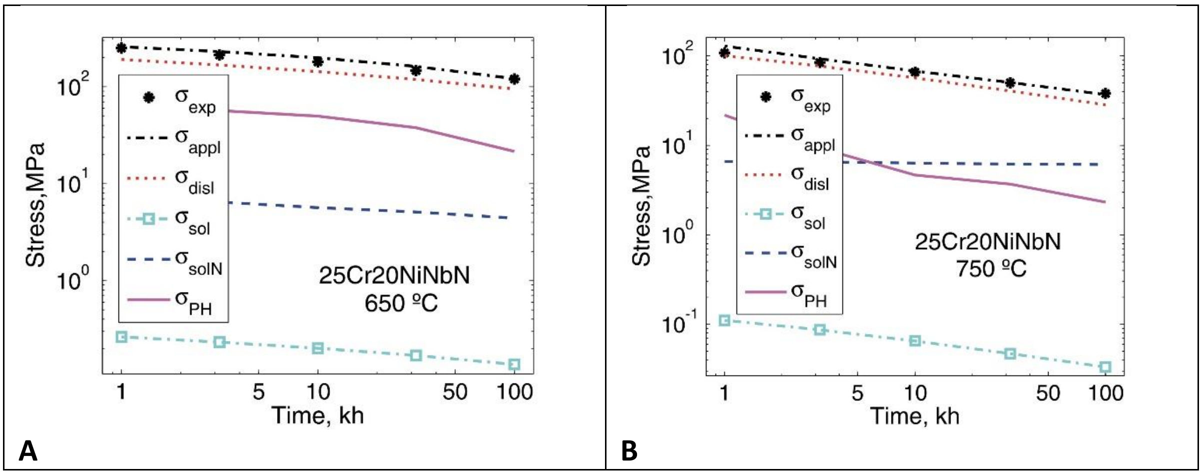

Figure 33: Contribution to the creep strength of 25Cr-20Ni-Nb-N from dislocations, precipitates and elements in solid solution versus creep time; A) 650°C, B) 750°C.

The creep rate can be calculated with the help of eq. (9) on page 19. The result is compared to experimental data in Figure 34.

The model gives quite a reasonable representation of the experimental creep rates. It can be seen that the model can describe how the slope of the creep curves (the creep exponent) increases by increasing stress and decreasing temperature. The exception is the highest temperature 750°C, where the experiments show the quite unusual behaviour that the creep exponent increases by temperature.

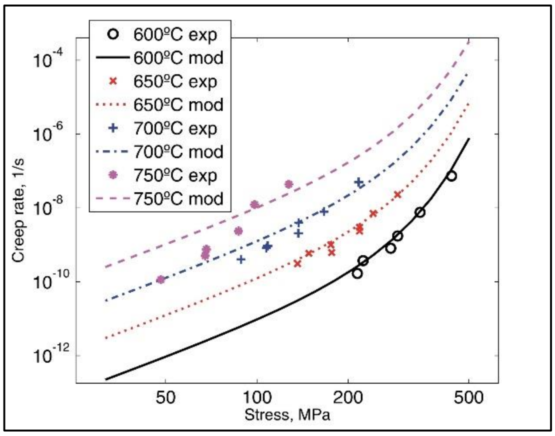

Figure 34: Stationary creep rate of 25Cr-20-Ni-Nb-N compared with experimental data from [24] at 600 to 750°C.

5.3.5 Discussion

In spite of the increase in radius of the Z phase during the ageing, Figure 23 on page 52, the increase in volume fraction gives a net reduction in the interparticle spacing and an increase in the Orowan strength, Figure 27 and Figure 28 on page 62. For the η phase the increase in particle radius is faster than the increase in phase fraction. Consequently, its Orowan strength contribution is reduced with ageing times, Figure 27 and Figure 28. The radius and fraction of $M_{23}C_6$.gi particles are constant at long ageing times, and as a result the Orowan strength contribution is unchanged. The same applies to $M_{23}C_6$.gb except at very long times where coarsening of the particles appears and the Orowan strength contribution drops. The strength contribution from σ is quite small. Due to the rapid increase in phase fractions at long times, no drop in strength contribution is found.

According to Figure 33 on page 67, the dominant contribution to the creep strength comes from the dislocations. Due to the combination of climb and glide in the eq. (11) on page 20, the variation of the creep exponent can be represented. The inverse slope m is 10.5 at short times and 3.9 at long times at 650°C. At the higher temperature 750°C, the corresponding values are m = 3.3 and m = 3.1, respectively. If glide had not been taken into account the inverse slope would have been constant, m = 3.

Figure 27 and Figure 28 on page 62 show that the total Orowan strength is fairly independent of ageing time except for an initial rise at short times. When climb is taken into account, the precipitation hardening drops with increasing creep time, see Figure 29 on page 64 and Figure 33 on page 67. The drop is much higher at the higher temperature due to a faster climb rate. Consequently, fewer particles will contribute to the creep strength, since the dislocations will be able to climb across also somewhat larger particles.

Two types of solid solution hardening have been analysed for substitutional and interstitial elements, respectively. Both types of solutes slow down the movement of the dislocations due to the lattice misfit to the host atoms. The substitutional elements give rise to a drag force on moving dislocations. The model for substitutional elements has been verified against experiments for Ni-20Cr-(6W) [15]. This alloy has the advantage that practically all W is in solid solution. This means that the complication for austenitic stainless steels where the substitutional element contribute to both particle and solid solution hardening is avoided. In spite of the fact that Nb has a large lattice misfit parameter, the solid solution hardening is small for the investigated steel. The reason is that the concentration of niobium in solution is quite small. The temperature and time dependence for this type of solid solution hardening is about the same as that of the dislocation hardening. The main effect of Nb in solution is that it increases the activation energy by the interaction of solutes and dislocations. When the dislocations climb, the cloud of solutes is quite narrow and the solutes will jump in and out of the cloud, which requires thermal activation. The additional activation energy explains why the activation energy for creep is considerably higher than that for self-diffusion for austenitic stainless steels.

The effect of interstitial elements on the solid solution hardening has also been analysed. From experiments and modelling of creep in copper doped with phosphorus, the influence of fast diffusing elements in solid solution has been studied. 50 wt. ppm P, all in solid solution, gives a large increase in the creep strength [18] as well as a large improvement in the creep ductility [17]. The assumption is that the P solutes are locked to the dislocations and that a break stress is needed to make the dislocations move [18]. The magnitude of the break stress gives the solid solution hardening. The model utilised in the present paper reproduces the influence of P on creep in copper [15]. Thus, this provides experimental verification of the model. The same mechanism is assumed to apply to nitrogen in solid solution in the investigated austenitic stainless steel. The break stress is proportional to the amount of nitrogen in the solute cloud around a dislocation. The resulting break stress is only weakly temperature and time dependent, which means that this strength contribution is important also at long times.

Diffusion creep has not been considered in the analysis. The reason is that the applied stress must be below about 5 MPa to give a creep exponent of unity, which is associated with the diffusion creep. This can be seen by considering a paper by Nilsson and Dunlop on a 20Cr 30NiTi steel [81], which is a steel with somewhat similar properties to 310NbN. They observed a creep exponent of unity below 5 MPa at 800°C. In another study on 20Cr25NiNb at 750°C creep was investigated at low stresses [82]. The shear stresses were 2.5 to 12.5 MPa corresponding to tensile stresses of 7.5 to 38 MPa taking the Taylor factor into account. In the paper they suggested that creep was controlled by Coble creep, but that is not realistic since the creep exponent was about three. If the creep rate is estimated with help of the dislocation model in the present paper it gives a creep exponent of three and a creep rate that is only a factor of three lower than the observed value. It can be concluded that the model gives a reasonable representation of the creep behaviour also at low stresses. Only at very low stresses diffusion creep is of importance. Unfortunately, there are considerable uncertainties in applying creep diffusion models [83]. For example for the results in [81] the creep rate computed with Nabarro-Herring's and Coble's formulae is an order of magnitude lower and an order of magnitude higher than the observed value, respectively. For these reasons diffusion creep has not been considered in the present model.

Another mechanism that could influence the creep strength is the climb of extended dislocations. With decreasing stacking fault energy the distance between the partial dislocations is increased, which would be expected to give a reduced creep rate for a given applied stress. Argon and Moffatt [84] derived an expression for the influence of the stacking fault energy on the creep rate. They obtained an expression where the creep rate was proportional to the square of the stacking fault energy. However, this does not seem to be consistent with creep data for austenitic stainless steels. We can take 304 (18Cr-10Ni) and 316 (17Cr-12Ni-2Mo) as an example. Their creep strength is essentially controlled by recovery of dislocations and the creep strength of 316 is only slightly higher than that of 304: However, 304 has a lower stacking fault energy than 316, which would suggest that the former material should have the largest creep strength in contrast to the observations. Similar results are obtained when the creep strength of other austenitic stainless steels are compared. It must be concluded that the effect of the stacking fault on the creep strength is limited. To sum up, the three dominating contributions to the creep strength of austenitic stainless steels come from the dislocations, precipitates and elements in solid solution.

5.3.6 Summary

In corporation with Prof. Sandström (KTH Stockholm) a creep strength modelling of the austenitic stainless steels 25Cr-20Ni-Nb-N is performed. The results can be summarized as follows:

- There are three main contributions to the creep strength from dislocations, precipitates and elements in solid solution.
- Hardening due to forest dislocations gives the largest contribution to the creep strength. A model originally developed for copper in the power-law break down regime was applied. The model could reproduce the observed variation in the slope of the creep rupture curve with temperature.
- When predicting the precipitation hardening, the particle distributions obtained from the modelling of the ageing of the alloy were used. Climb across the particles reduces the creep strength. After long time exposure at high temperatures more particles are climbed, thus the creep strength is reduced. It is assumed that only particles that are large enough and cannot be passed by climbing dislocations contribute to the creep strength as suggested by a number of previously performed studies.
- Nb in solid solution gives rise to a drag stress by forming solute clouds around the dislocations. However, this strength contribution is negligibly small. N in solid solution is assumed to be locked to the dislocations to a large extent. Thus a break stress is needed in order to move the dislocations. This contribution to the creep strength is fairly independent of creep time and temperature.
- The model for the creep rate can in a reasonable way describe how the creep exponent is increasing with increasing stress and decreasing temperature.

Taking into account the different contributions to the creep strength, the total creep strength can be predicted. It is in agreement with the experimental value.

6 Modification of 25Cr-20Ni-Nb-N Austenitic Steel

The procedure for the modification of the 25Cr-20Ni-Nb-N austenitic steel is shown in Figure 35. The process can be split up into seven sections: (1) Start condition; (2) Objectives; (3) Calculation; (4) Manufacturing; (5) Testing; (6) Investigation; and (7) Evaluation. With the help of (1) already performed precipitation evolution (see chapter 5.2.2 on page 50) and the (2) objectives, additional (3) precipitation calculations are performed where the modified composition for the 25Cr-20Ni-Nb-N austenitic steel is defined.

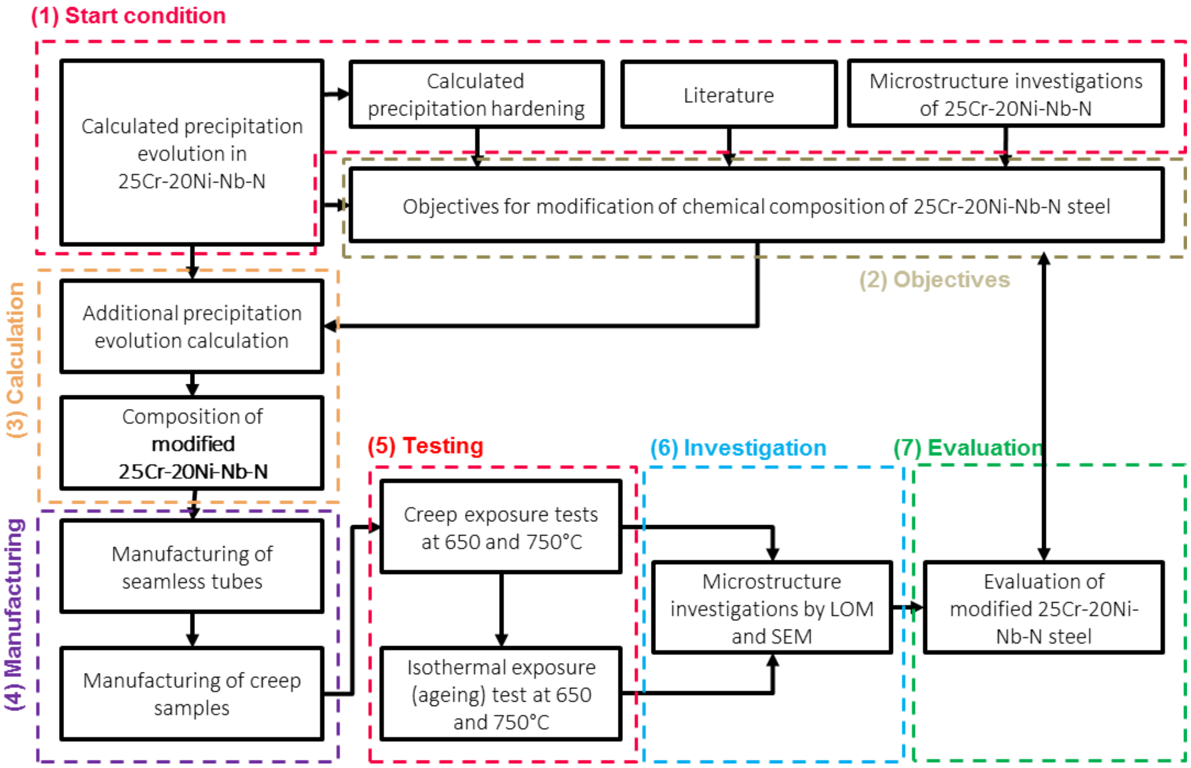

Figure 35: Applied modification process for 25Cr-20Ni-Nb-N austenitic steel.

Using the modified composition, (4) seamless tubes for superheater application are produced. Afterwards, creep samples are manufactured in order to perform (5) creep and thermal exposure tests. The isothermal exposure tests are performed with the head section of the premature fractured creep samples. When the tests are completed, the microstructure is (6) investigated by LOM and SEM technique. Finally, the microstructure results of the modified steel are (7) evaluated with respect to the objectives.

6.1 Objectives

The chemical composition of the 25Cr-20Ni-Nb-N steel is changed in order to modify the precipitation evolution. To avoid a completely new material standardisation process, which is very time- and cost-intensive, the modification of the microstructure is performed within the ASTM standard of the 25Cr-20Ni-Nb-N steel. The upper and lower limits of the ASTM standard are presented in Table 12.

Table 12: Limits for the modification of the chemical composition in wt.%.

	C	**Si**	**Mn**	**Cr**	**Ni**	**Nb**	**N**
MAX	**0.100**	**0.75**	**2.0**	**26.0**	**23.0**	**0.60**	**0.350**
25Cr-20Ni-Nb-N (Non-modified)	0.062	0.38	1.2	24.7	20.6	0.44	0.182
MIN	**0.040**	**0.0**	**0.0**	**24.0**	**17.0**	**0.20**	**0.150**

The modification process contains several objectives. These objectives are defined by the MACPLUS project partners and are listed below:

1. In order to avoid a new material standardisation process, the modified composition must be within the ASTM standard of 25Cr-20Ni-Nb-N steel.
2. The corrosion attacks by Iron-alkali sulfate increase to a maximum at 700°C [9]. Since the austenitic steels are operating in this temperature range, a strong corrosion attack is expected. A high chromium content is an effective way to increase the corrosion resistance. Therefore, the chromium content in the modified steel must be at least 25wt.% to guarantee sufficient corrosion resistance at high temperature.
3. The intermetallic σ-phase in lumpy form is expected to have detrimental effect on the mechanical behaviour of stainless steels. In [9] it is reported that the σ-phase is very brittle, and therefore its formation reduces the ductility and fracture toughness. In addition, its formation causes a depletion of chromium in the matrix

which in turn decreases the corrosion resistance. Calculations show that σ-phase in the 25Cr-20Ni-Nb-N steel shows a very fast growth, a high phase fraction (≈10%) and a mean radius of more than 2,500nm after 100,000h ageing at 650°C. This high σ-phase fraction causes a depletion of chromium (from 25 to 20%) in the matrix, as can be seen in Figure 36(A). In order to demonstrate the importance of chromium, the total corrosion (scale thickness plus penetration) of several austenitic steels exposure at 650°C in environment of coal ash and 10% alkali sulfate and with/without 5% NaCl is shown in Figure 36(B). For service in superheater applications, the corrosion rate should be smaller than <0.5mm/y [85]. The chromium content of each steel is noted on the top of the bars. When the total corrosion in NaCl rich environment (black bars) is analysed, it can be seen, that steels with low chromium content such as 347HFG (18%Cr), have several times higher total corrosion rate per year than high chromium steels such as HR3C (25%Cr). This in turn means that the depletion of chromium (by formation of σ-phase, see Figure 36(A)) can drastically increase the total corrosion of investigated 25Cr-20Ni-Nb-N austenitic steel. Summarizing all these findings, the major objective of the modification process is to supress the formation of σ-phase.

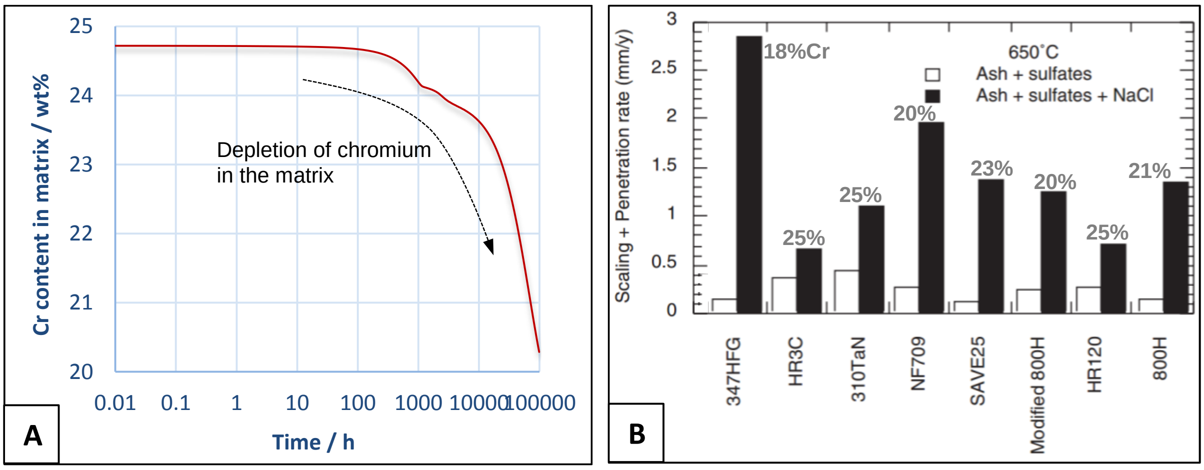

Figure 36: Depletion of chromium in matrix of investigated 25Cr-20Ni-Nb-N steel (A) and scaling rate plus penetration rate for several austenitic steels after exposure in presence of various deposits (5 wt% NaCl) [85] (B) at 650°C.

4. In addition to corrosion resistance, the creep strength of austenitic steels is of great importance for superheater applications. Therefore, one additional objective is to avoid a loss of creep strength in the modified austenitic steel. It is shown in Figure 27(B) and Figure 28(B) on page 63 that fine precipitates such as secondary Nb(C,N)

and Z-phase contribute significantly to the creep strength. In order to avoid a loss, and/or to increase the creep strength, the Z-phase and Nb(C,N) phase fractions should be increased and mean radii decreased.

5. In [7] it is reported that at high stresses the fracture mainly occurs along grain boundaries, by grain boundary sliding. Small grain boundary precipitates, such as a $M_{23}C_6$-film in Figure 16 on page 38, are expected to promote grain boundary sliding. According to [7], large grain boundary precipitates with low interparticle spacing are promising against grain boundary sliding. Therefore, one additional objective is to increase the size and decrease the interparticle spacing of grain boundary precipitates.

The modification process is performed by equilibrium-, Scheil- and kinetic-calculations using the software MatCalc. The calculations are performed with the same setup mode as described in chapter 4.3 on page 28.

6.2 Thermodynamic and Thermokinetic Calculations

6.2.1 Results

Several equilibrium calculations are performed to demonstrate the influence of the main chemical elements such as chromium, carbon, nitrogen and niobium on the phase fractions in the 25Cr-20Ni-Nb-N steel. The results of these calculations for 650°C are presented in Figure 37. On the horizontal axis a lower and higher content (compared to the non-modified composition) of chromium, carbon, nitrogen and niobium is shown. On the vertical axis the change of phase fraction relative to the non-modified composition is shown. As can be seen, the chromium content has a significant influence on the σ-phase. A higher chromium content (26% Cr) increases the fraction of the σ-phase whereas a lower content (22% Cr) decreases it. The carbon content mostly influences the phase fraction of $M_{23}C_6$. A higher amount of carbon (0.08% C) increases the fraction of $M_{23}C_6$ whereas a lower amount (0.05% C) decreases it. The nitrogen content has an effect on both σ- and η-phase. A lower content of nitrogen (0.14% N) increases the fraction of σ-phase and decreases the fraction of η-phase. The opposite is observed when higher nitrogen content (0.25% N) is used. The niobium content has a major influence on the Z-phase but also, to a lesser extent, on the η- and σ-phase. A higher content of niobium (0.6% Nb) increases the fraction of the Z-phase and σ-phase, whereas the η-phase fraction is decreased. The opposite happens when a lower niobium content (0.3% Nb) is used.

Since the results for 750°C equilibrium temperature are similar to the 650°C, they are not presented in the figure.

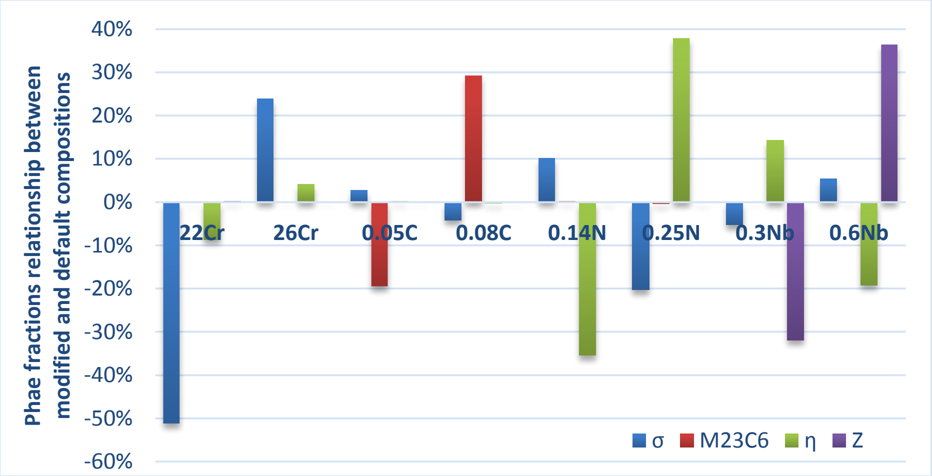

Figure 37: Influence of Cr, C, N, Nb on equilibrium phase fractions at 650°C.

The equilibrium calculations are restricted to a condition with infinite exposure time at constant temperature. No influence of heat treatment and microstructure such as grain size and primary precipitates can be considered in the equilibrium calculations. Therefore, it is not useful to modify the chemical composition only on the base of equilibrium calculations. Considering that, precipitation kinetics calculations are performed. In total many precipitation calculations with different compositions are performed. Using the results from equilibrium calculations as well as precipitation calculations by MatCalc a modified (most promising) composition is defined, as shown in Table 13.

Table 13: Modified chemical composition (wt%) of 25Cr-20Ni-Nb-N steel.

	C	Cr	Si	Ni	Nb	Mn	N	W	Cu
25Cr-20Ni-Nb-N (Non-modified)	0.062	24.7	0.38	20.6	0.44	1.2	0.1819	-	-
Modified	0.062	**25.0**	0.38	20.6	**0.60**	1.2	**0.3500**	**0.5**	**0.5**

Table 13 shows that the carbon, silicon, nickel and manganese contents remain unchanged. The chromium content is slightly increased to provide high corrosion resistance. The niobium content is increased to the maximum allowed amount of 0.6% to promote the formation of fine Z-phase. The nitrogen content is increased to the maximum allowed amount of 0.35% to promote the Z-phase formation and to avoid σ-phase formation. A higher content of nitrogen and niobium is expected to increase the creep strength, as shown in Figure 5 on page 18. Tungsten is added to the maximum allowable amount of 0.5% to increase the solid solution hardening [7]. Sanicro 25 is a newly developed austenitic steel for USC/A-USC power plant applications. Its chemical composition is similar to the steel investigated in this thesis with one difference: Sanicro 25 contains 3% copper, which promotes the precipitation of fine Cu-rich precipitates and which are expected to be important for the creep strength. In order to achieve a similar effect, the copper content in the modified austenitic steel is increased to the maximum allowable amount of 0.5%.

Figure 38 shows a comparison between the modified and non-modified composition at 650 and 750°C after 100,000h. On the horizontal axis the precipitates are presented. On the vertical axis the change of phase fraction and mean radii relative to the non-modified composition is shown. As can be seen, the fraction of $M_{23}C_6$.gb is lower, whereas the fraction of $M_{23}C_6$.gi is higher. The detrimental σ-phase is completely suspended at 650 and 750°C. No Nb(C,N)(prim) are present. The phase fraction of secondary Nb(C,N) and Z(prim) is higher. The fraction of secondary Z-phase is lower. A higher η-phase fraction is predicted for both 650 and 750°C.

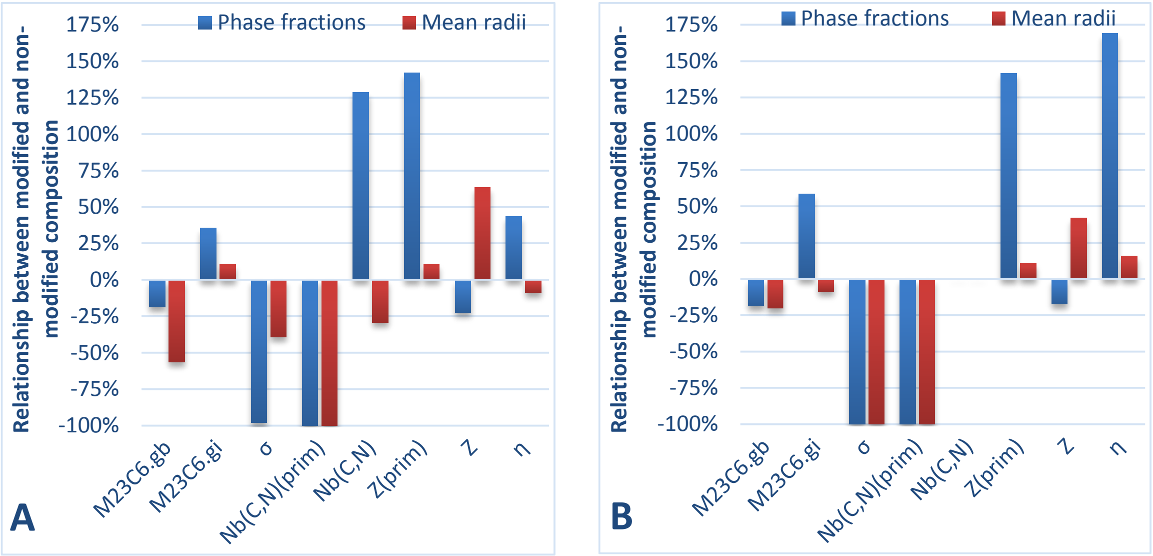

Figure 38: Precipitates phase fractions and mean radii of modified composition (related to non-modified composition) at (A) 650°C and (B) 750°C after 100,000h exposure time.

6.2.1.1 Discussion

The modified composition is in the ASTM standard of the 25Cr-20Ni-Nb-N steel, that means that the first objective is achieved. Considering the second objective, the chromium content is slightly increased (from 24.7 to 25%Cr), therefore a sufficient high corrosion resistance is expected. The third and major objective was to supress the formation of σ-phase. Figure 38 shows that almost no σ-phase is present at 650 and 750°C. It is expected that the absence of σ-phase should increase the ductility and fracture toughness of modified steel. Additionally, the solute chromium in modified steel (≈24%Cr after 100,000h) is significantly higher compared to the non-modified steel (≈20%Cr after 100,000h), as shown in Figure 39. As a result, a higher corrosion resistance of the modified composition is expected.

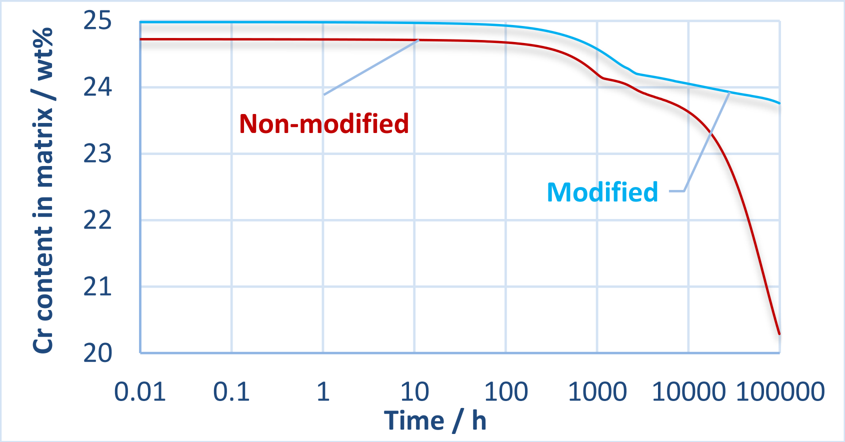

Figure 39: Chromium content in the matrix of non-modifeid and modified steel.

It is shown in Figure 27(B) and Figure 28(B) on page 63 that fine Z-phase and Nb(C,N) precipitates are most important for the creep strength of the 25C5-20Ni-Nb-N steel. In order to achieve a high creep strength by precipitation hardening, a high precipitates phase fraction and small radius is necessary. Figure 40 shows the evolution of Z-phase and Nb(C,N) precipitates in the non-modified and modified steel at 650 and 750°C exposure. When the Z-phase is analysed, it can be seen that at beginning of the exposure the phase fraction of Z-phase is higher in modified composition compared to the non-modified. At later exposure times the Z-phase fraction in non-modified composition becomes higher. The mean radius of the Z-phase is higher within whole exposure time in modified composition compared to non-modified. As a result, the interparticle spacing of Z-phase (see Figure 40(E, F)) is lower in non-modified composition. Summarizing these observations about Z-phase, it can be expected that the contribution of Z-phase to the creep strength is lower (due to the higher interparticle spacing) in modified composition than in non-modified. This is not the case for Nb(C,N) precipitates, where the interparticle spacing is lower in modified composition, and therefore a higher contribution to the creep strength of Nb(C,N) is expected.

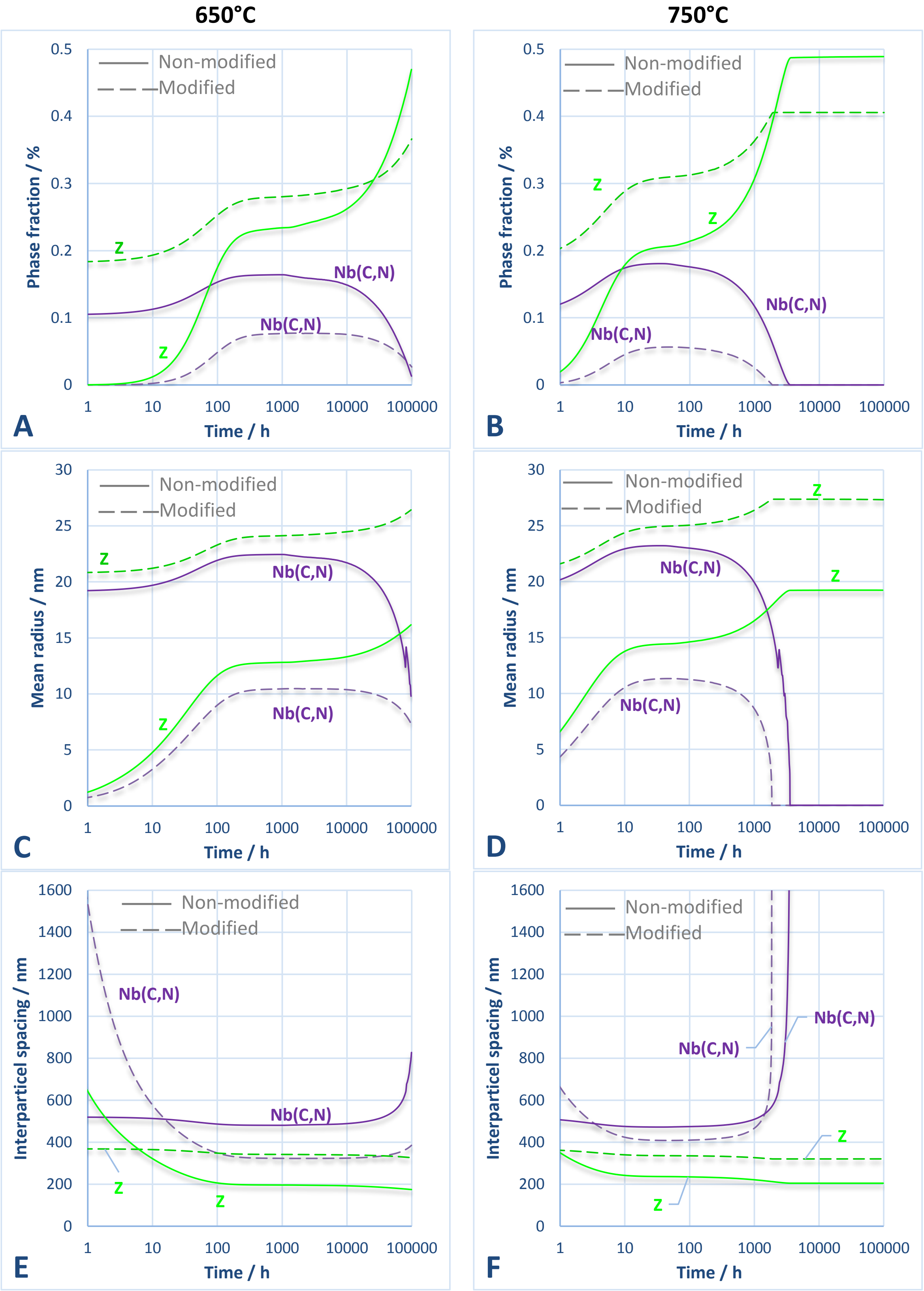

Figure 40: Evolution of phase fractions (A, B), mean radii (C, D) and interparticle spacing (E, F)) of secondary Z-phase and Nb(C,N) in modified and non-modified composition.

Additional to the Z-phase and Nb(C,N) precipitates, the contribution of nitrogen to the creep strength by solid solution is also of great importance, as presented in Figure 32(B) on page 66. It is expected that a higher nitrogen content increase the creep strength (see Figure 5 on page 18). The evolution of nitrogen content in solid solution of non-modified and modified composition is shown in Figure 41. As can be seen, the nitrogen content is two times higher in modified composition compared to non-modified. Therefore, a higher contribution from solid solution hardening by nitrogen in modified composition is expected.

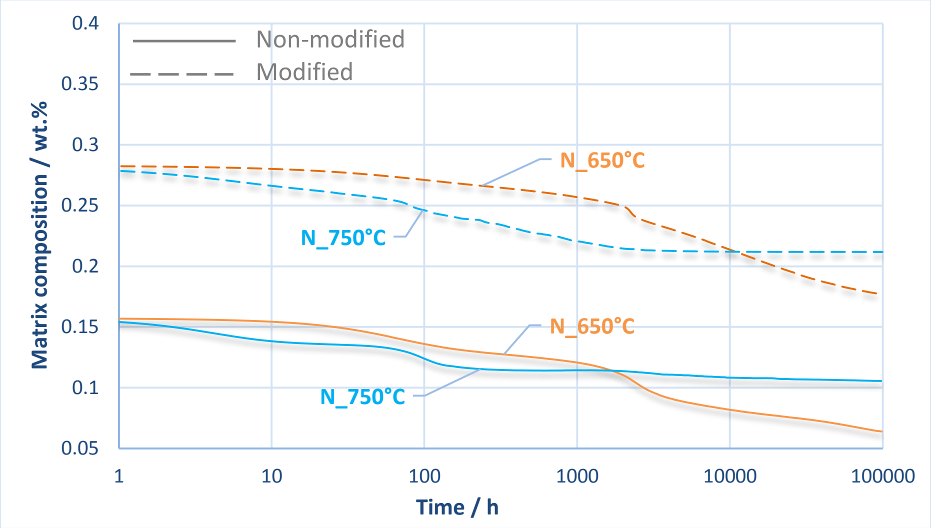

Figure 41: Evolution of nitrogen content in solid solution in modified and non-modified composition at 650 and 750°C.

Summarizing the observations about precipitation hardening by Z-phase, Nb(C,N) and solid solution hardening by nitrogen in modified composition, it can be concluded that on the one hand the precipitation hardening by Z-phase is lower, but on the other hand the precipitation hardening by Nb(C,N) and solid solution hardening by nitrogen is higher. Furthermore, the modified composition contains 0.5% tungsten, which in turn increases the solid solution hardening. Additional to that, creep strength calculations (not presented in this thesis) by Prof. Sandström (KTH Stockholm) of modified composition are performed where no loss of creep strength is predicted. Finally, no loss of creep strength in modified composition is expected and therefore the fourth objective is achieved.

Small precipitates such as Z-phase and Nb(C,N) are obstacles against moving of dislocations and are therefore of great importance for the matrix strength. This in turn avoid a transgranular material failure. Additional to that, intergranular failure, by grain boundary sliding can occur. An effective way to avoid grain boundary sliding are large grain boundary precipitates with small interparticle spacing [7]. Figure 42 shows the evolution of the phase fraction, mean radius and interparticle spacing of grain boundary precipitates such as

$M_{23}C_6$.gb and η-phase in modified and non-modified composition. As can be seen, the size and interparticle spacing of $M_{23}C_6$.gb is significantly lower in modified composition compared to non-modified. When the η-phase radius is analysed, it is similar in both, modified and non-modified composition. The η-phase interparticle spacing, at late ageing time, is lower in modified composition. To sum up the observations about grain boundary precipitates, it is to mention that on the one hand the grain boundary precipitates are smaller which promote grain boundary sliding in modified composition, but on the other hand the interparticle spacing is lower that prevents grain boundary sliding. However, no higher resistance against grain boundary sliding in modified composition is expected, and therefore the fifth objective is not successfully achieved.

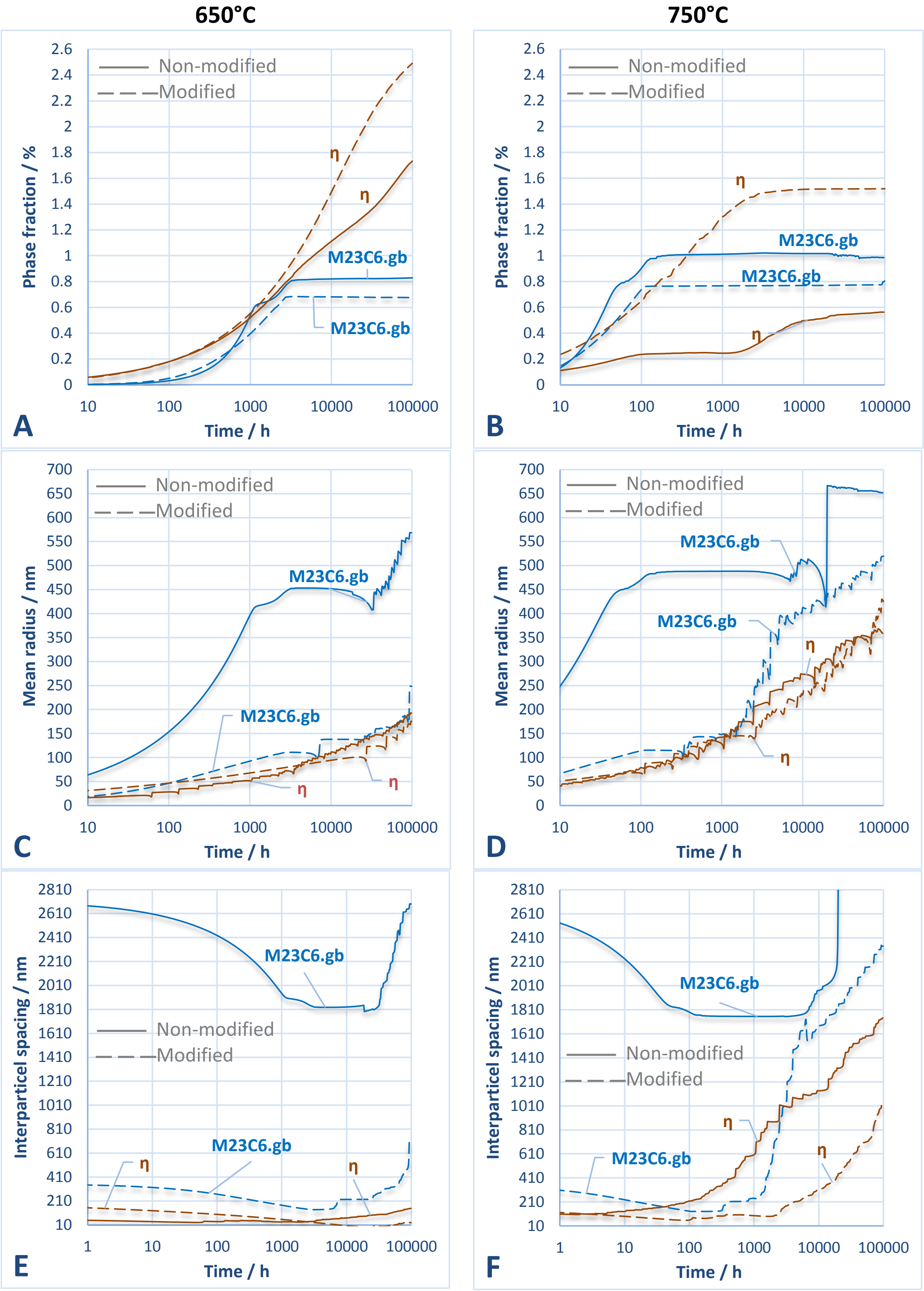

Figure 42: Evolution of phase fractions (A, B), mean radii (C, D) and interparticel spacing (E, F) of $M_{23}C_6$.gb and η-phase in modified and non-modified composition.

6.2.1.2 Summary

Modification of chemical composition of the 25Cr-20Ni-Nb-N steel is performed. For the modification process, equilibrium, Scheil and precipitation calculations by MatCalc are applied. These calculations are carried out by the author at the Institute of Materials Science and Welding. The results are summarized as follows:

- Influence of chromium, carbon, nitrogen and niobium on the equilibrium phases in the 25Cr-20Ni-Nb-N steel is shown.
- The modified composition is within the standard of 25Cr-20Ni-Nb-N steel.
- The chromium content in the modified composition is slightly increased to increase the corrosion resistance.
- The σ-phase is almost not present in the modified composition. Therefore a higher toughness of modified composition is expected.
- No loss of creep strength in modified composition is expected.

Finally a modified composition is suggested which can be used for manufacturing of seamless tubes for superheater applications.

6.3 Material and Experimental

6.3.1 The Modified 25Cr-20Ni-Nb-N Steel

The whole manufacturing process of the modified steel can be classified into production of the ingot, forging and extruding of the tubes. When the semi ingot was produced, a hot forging is applied. The chemical analysis of the ingot (heat) as well as the target composition (marked in red) can be seen in Table 14. Almost all elements are within the modified composition except carbon which is ≈20% higher than the defined one.

Table 14: Chemical composition (wt%) of modified 25Cr-20Ni-Nb-N ingot.

	C	Cr	Si	P	Ni	Nb	Mn	N	S	W	Cu
Target	0.062	25.00	0.38	-	20.6	0.60	1.20	0.35	-	0.50	0.50
Heat	0.075	25.27	0.39	0.023	20.3	0.61	1.17	0.34	<0.003	0.46	0.47

After the hot forging is applied, the ingot becomes a polygon like shape, where the outer surface contains a certain amount of defects and cracks. In order to remove these, a grinding was applied. Afterwards the polygon like shaped sample is rotary forged to be able to prepare the sample for the manufacturing of tubes. The tube manufacturing process is shown in Figure 3 on page 9. Some pictures taken during the extrusion process are shown in Figure 43.

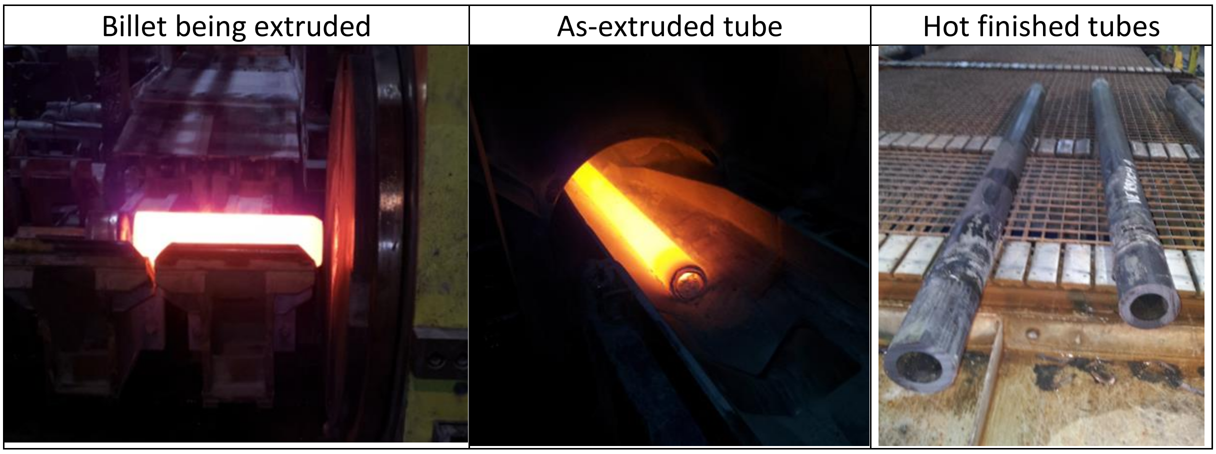
Billet being extruded
As-extruded tube
Hot finished tubes

Figure 43: Modified 25Cr-20Ni-Nb-N austenitic steel during extrusion [26].

The tube parameters such as tube diameter, length, amount, determines what forming process, cold pilgering or drawing, has to be applied. In the case of the present steel the cold drawing came out to be more suitable. Both processes have the same effect: (i) to increase the strength by work hardening and/or (ii) to increase the degree of deformation in order to adjust the grain size during solution annealing by recrystallization.

Two types of extruded tubes are manufactured. One tube is cold drawn and solution annealed (at 1230°C for 15min in order to adjust the grain size and to dissolve the precipitates which have formed during the manufacturing of the tubes) whereas the other one is only quenched immediately after extrusion.

6.3.2 Creep Exposure Test

In the chapter above, the manufacturing processes of the as-received tubes are explained. Out of these as-received tubes, creep samples are manufactured. For the creep tests both type of tubes are used, the first one was cold drawn and solution annealed, whereas the second one was only quenched immediately after extrusion. The tubes are noted as:

- Tube condition ECS (Extruded cold drawn and solution annealed)
- Tube condition EQ (Extruded and quenched immediately after extrusion)

The dimension of the ECS tube is 54mm in outer diameter and 7mm in thickness, whereas the dimension of the EQ tube is 60mm in outer diameter and 8mm in thickness. Creep samples are manufactured out of the tubes in order to evaluate the creep rupture strength of modified composition with the creep rupture data of 25Cr-20Ni-Nb-N (HR3C) steel. Since long-term creep tests are too time consuming, a creep rupture time up to ≈1,000h is chosen, this corresponds to a stress of ≈250MPa at 650°C and ≈110MPa at 750°C, see Figure 4 on page 17. In total six creep samples are manufactured. For each tube type (ECS, EQ) three stresses are chosen:

- At 650°C: 250, 300 and 325MPa
- At 750°C: 110, 132 and 143MPa.

It is expected that the above mentioned stresses cause a creep rupture up to 1,000h creep exposure. The creep samples are prepared according the DIN50125 and the location of the creep samples can be seen in Figure 44. One half of the tubes is used to investigate the tubes in as-received condition and the other half is used for creep samples preparation.

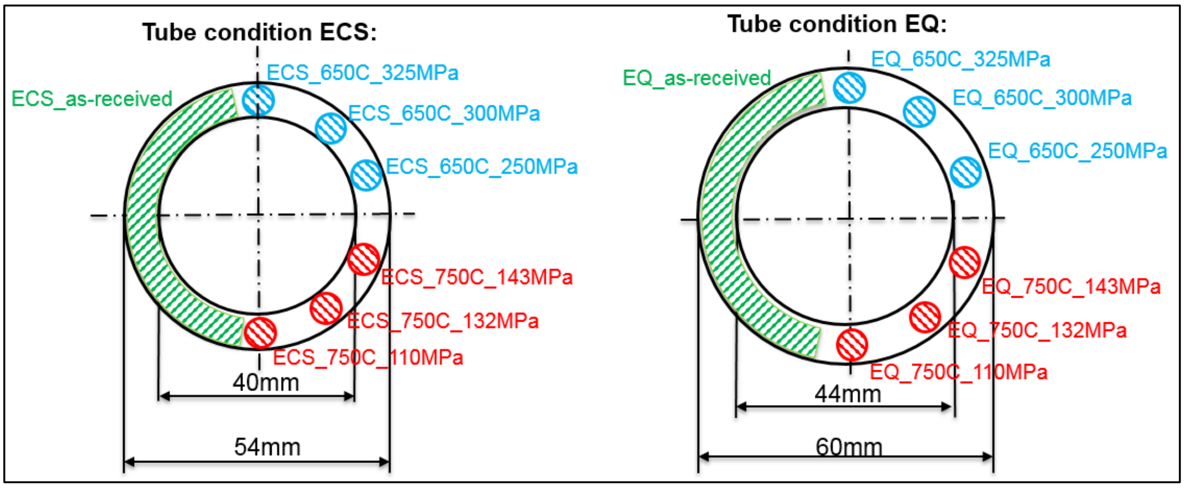

Figure 44: Location and notation of creep samples.

6.3.3 Isothermal Exposure Tests (Ageing)

The following chapter will show that all creep samples with the modified composition are ruptured before 1,000h exposure time (longest creep rupture time 682h). These rupture times are not representative to compare the microstructure with the non-modified steel (shortest ageing time 1,000h). For a suitable comparison with the non-modified composition, the head sections of the fractured modified creep samples, which have not been creep-loaded (only aged), are cut down and subsequently aged at 650 and 750°C until a total time of 1,000h has been reached.

6.4 Results and Discussion

6.4.1 Microstructure in As-received Condition

The dominant precipitates in the as-received condition are the primary Z-phase precipitates. They are randomly distributed on grain boundaries and grain interior. In Figure 45(A) a SEM micrograph of an as-received ECS sample is shown. The bright precipitates are primary Z-phase particles. They contain most niobium, chromium and iron, as shown in the EDS analysis in Figure 45(B).

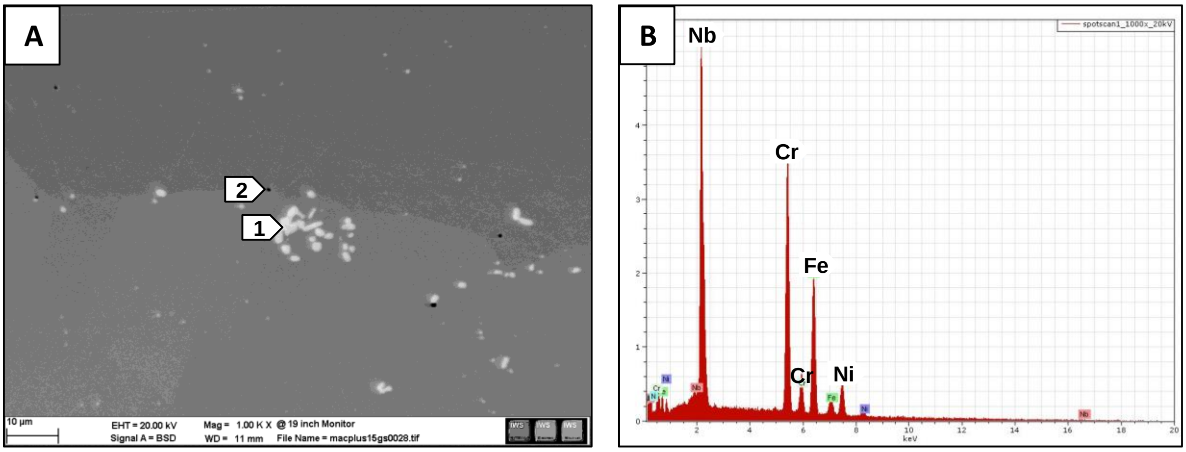

Figure 45: Primary Z-phase precipitates in as-received ECS condition (A) and EDS analysis of primary Z-phase (B). A-1: primary Z-phase; A-2: Pores.

More than 560 primary precipitates are analysed. The area fraction varies between 0.3% and 0.58%. The size distribution is shown in Figure 46. As can be seen, most of the primary precipitates have a diameter of ≈2µm.

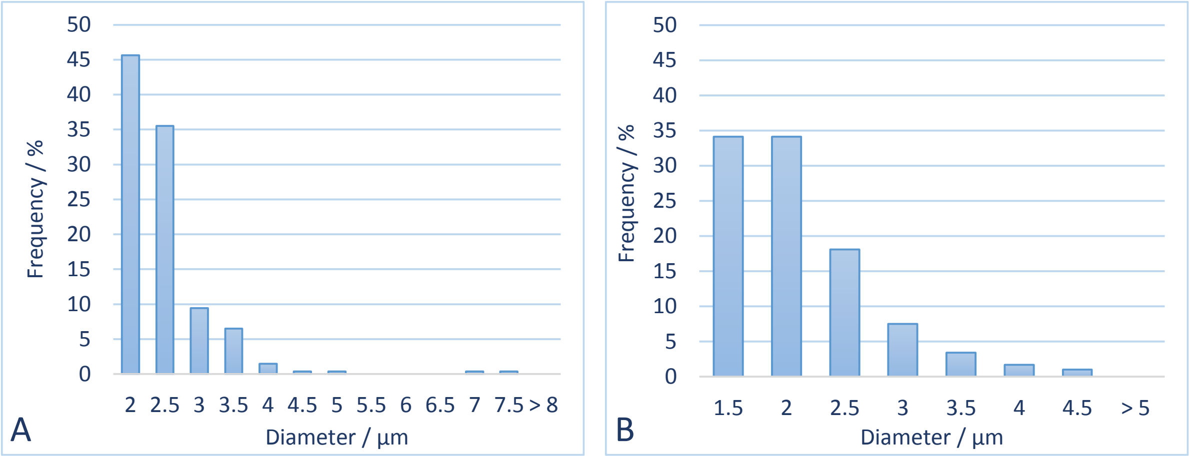

Figure 46: Distribution of primary precipitates in (A) ECS and (B) EQ sample.

6.4.2 Creep Strength and Microstructure at 650°C

EQ and ECS samples are creep exposed at 650°C for 250, 300 and 325MPa. All creep samples including their rupture times are shown in Figure 47. As can be seen, samples tested at low stress like 250MPa are ruptured in the head section of the creep sample, whereas samples tested at high stresses like 300 and 325MPa are ruptured in the load (gauge) section. There are no significant differences in creep strength between EQ and ECS samples can be observed. All creep samples do not show any significant reduction of area. When rupture times of modified composition are compared with HR3C (reference material), see Table 15, it is obvious that the modified composition is ruptured much earlier. The creep samples tested at 250MPa are broken in the head, and therefore they cannot be used for the comparison.

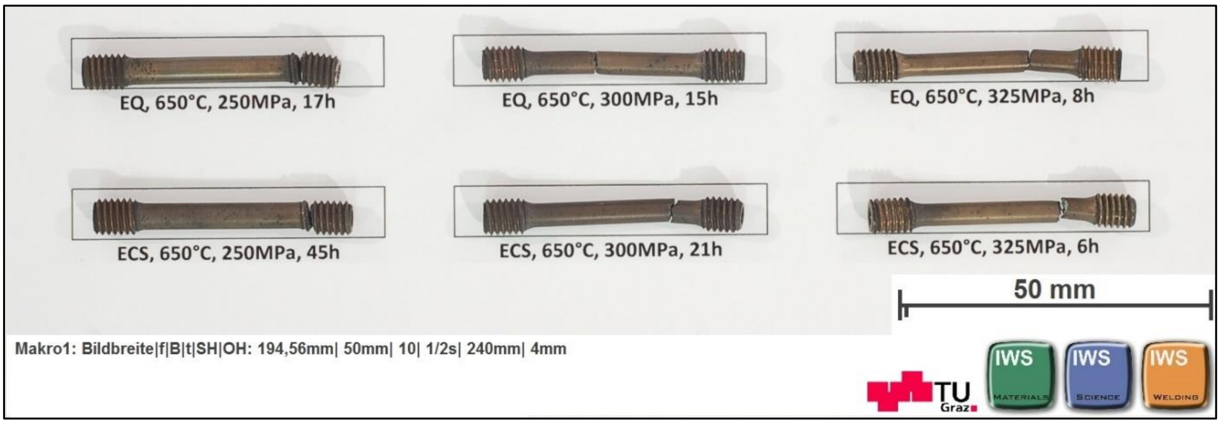

Figure 47: Creep samples ruptured at 650°C.

Table 15: Creep rupture times of HR3C and modified 25Cr-20Ni-Nb-N at 650°C.

		250MPa	300MPa	325MPa
HR3C [24]		480h*	220h*	80h*
Modified 25Cr20Ni-Nb-N	EQ	(17h)	15h	8h
	ECS	(45h)	21h	6h

* Average rupture time; () Broken in head section of creep sample.

The fracture surface of an ECS sample in Figure 48(A) clearly reveals an intergranular brittle fracture. Similar fracture is observed for all creep samples. Figure 48(B-2) shows the formation of a crack along the grain boundary. The bright precipitates, Figure 48(B-1), are primary Z-phase precipitates and (B-3) is a twin boundary which is typical for an austenite microstructure.

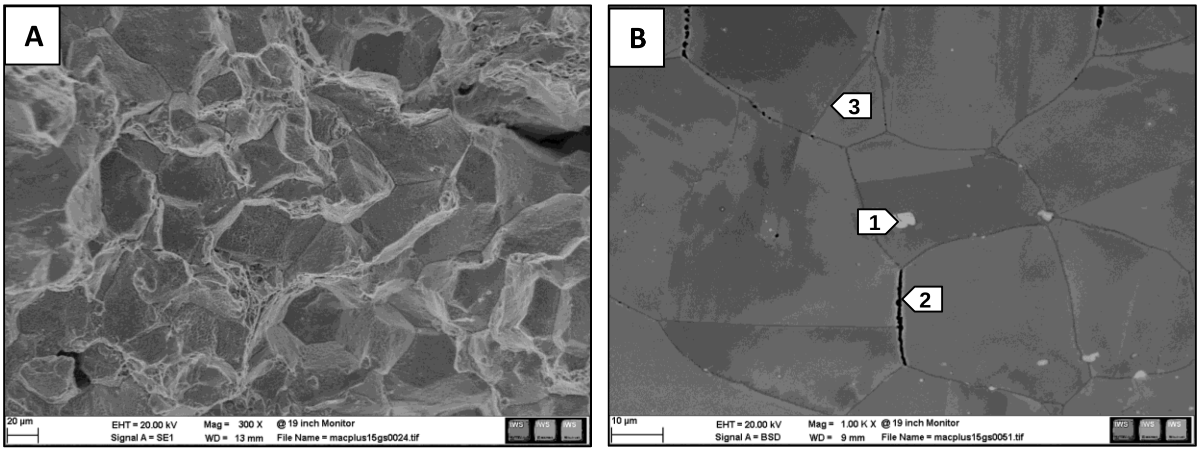

Figure 48: Fracture surface (A) and cross section (B) of ECS sample after creep exposure at 650°C and 300MPa for 21h. B-1: Primary Z-phase; B-2: Crack along a grain boudary; B-3: Twin boundary.

In order to compare the microstructure of the modified composition with the non-modified composition (see chapter 5.1.1 on page 35) in addition to the creep tests an ageing treatment (up to a total time of 1,000h) is applied. For ageing the head section of an ECS creep sample is used. Figure 49(A) shows a low magnification and (B) a high magnification of a grain boundary triple point of an ECS sample aged at 650°C for 1,000h. Besides primary Z-phase precipitates, no other precipitates such as σ-phase are detected.

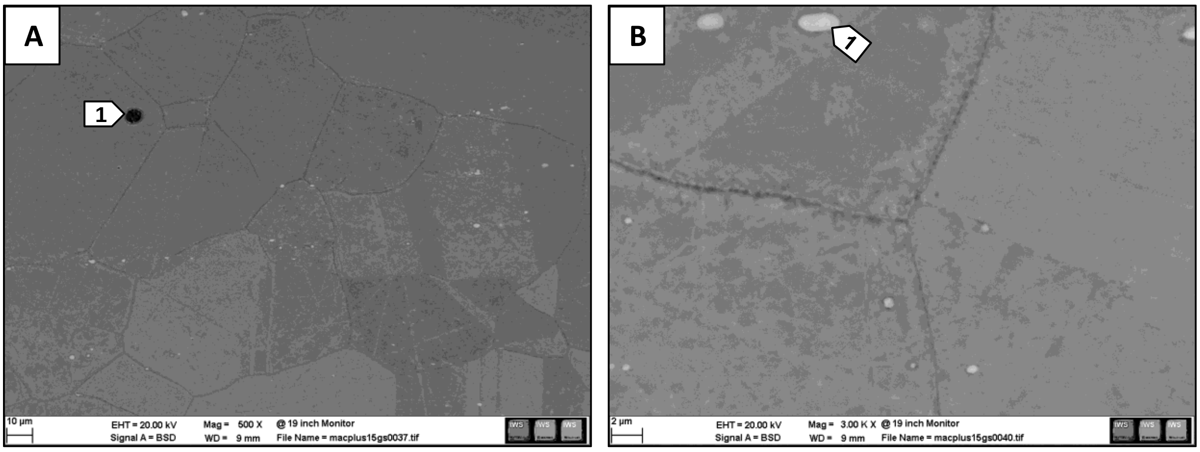

Figure 49: Low magnification (A) and high magnification of grain boundary triple point (B) of ECS sample aged at 650°C for 1,000h. A-1: Inclusion; B-1: Primary Z-phase.

6.4.3 Creep Strength and Microstructure at 750°C

EQ and ECS samples are creep exposed at 750°C for 110, 132 and 143MPa. All creep samples including their rupture times are shown in Figure 50. As can be seen, EQ sample tested at low stress such as 110MPa is ruptured in the head section of the creep sample, whereas all other samples are ruptured in the load (gauge) section. All creep samples do not show any significant reduction of area. When rupture times of modified composition are compared with HR3C (reference material), see Table 16, it can be seen that the modified composition is ruptured earlier. The creep sample EQ tested at 110MPa is broken in the head section, and therefore it cannot be used for the comparison.

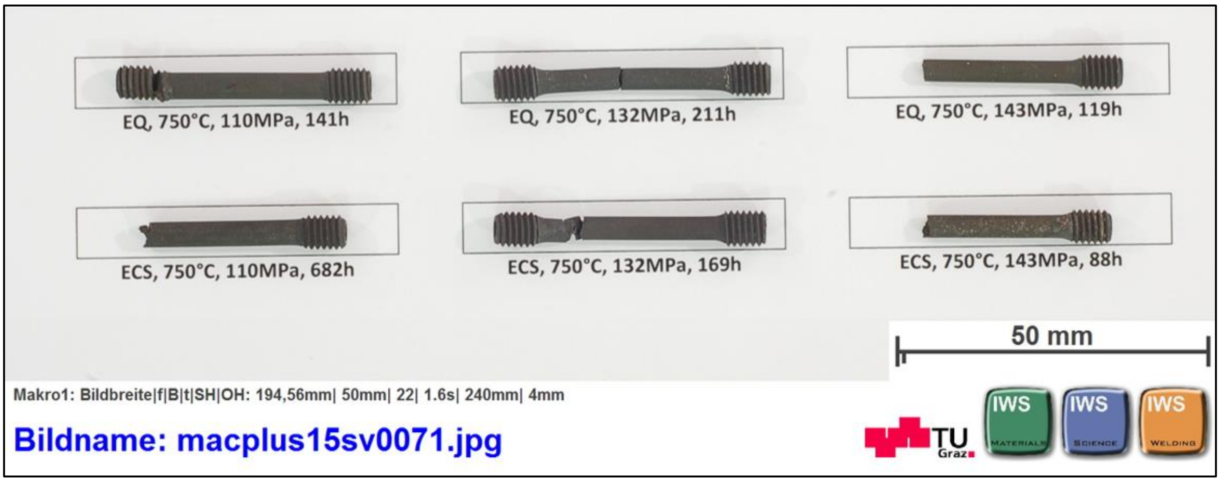

Figure 50: Creep samples ruptured at 750°C.

Table 16: Creep rupture times of HR3C and modified 25Cr-20Ni-Nb-N at 750°C.

		110MPa	**132MPa**	**143MPa**
HR3C [24]		700h*	220h*	180h*
Modified 25Cr20Ni-Nb-N	EQ	(141h)	211h	119h
	ECS	682h	169h	88h

* Average rupture time; () Broken in head section of creep sample.

Figure 51(A) shows the fracture surface of an ECS creep sample exposed at 750°C and 110MPa for 682h. The individual grains indicate that fracture occurs along the grain boundaries. This is also shown in Figure 51(B-2), where cracks formed along grain boundaries. The bright precipitates, see Figure 51(B-1), are randomly distributed primary Z-phase precipitates.

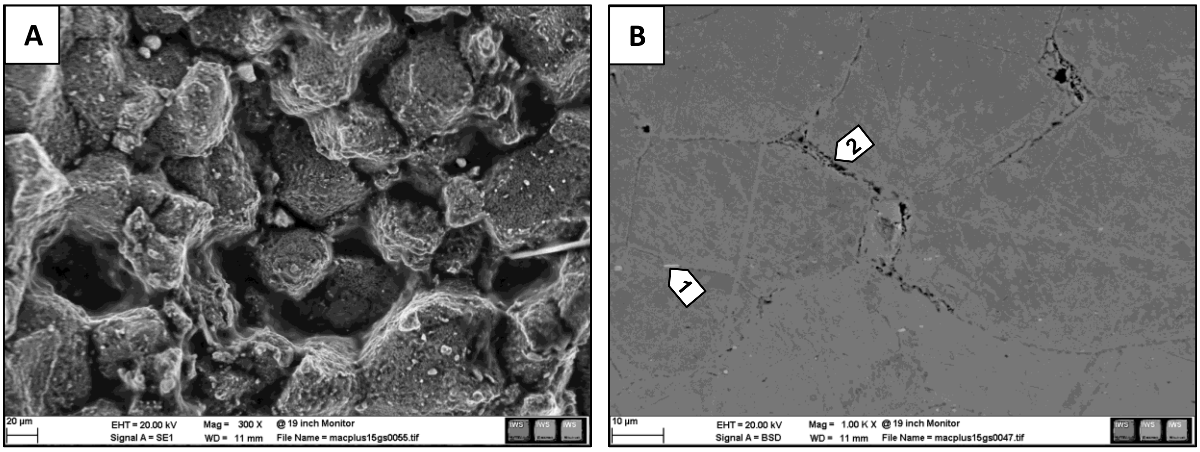

Figure 51: Fracture surface (A) and cross section (B) of ECS sample after creep exposure at 750°C and 110MPa for 682h. B-1: Primary Z-phase; B-2: Crack along a grain boundary.

In order to compare the microstructure of the modified composition with the non-modified composition (see chapter 5.1.2 on page 37), the head of the ECS creep sample (750°C/110MPa) is cut down and afterwards heat treated up to a total times of 1,000h at 750°C. The microstructure of the aged ECS sample is shown in Figure 52. The primary Z-phase precipitates are randomly distributed, see Figure 52(A-1). The grain boundaries are surrounded by η-phase precipitates, see Figure 52(B-2). The EDS analysis of the η-phase and primary Z-phase is shown in Figure 53(B). As can be seen, when EDS line scan cross the grain boundary precipitate (see Figure 53(B-1)), the silicon-, nickel- and chromium-intensity increase, which is an indication for η-phase. No σ-phase precipitate could be observed along grain boundaries and on grain boundary triple points.

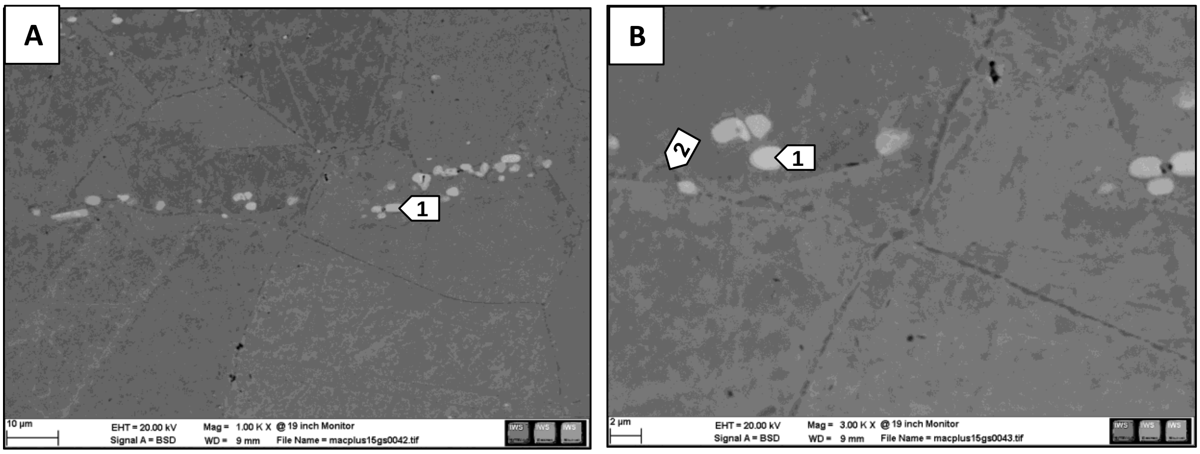

Figure 52: Low magnification (A) and high magnification of grain boundary triple point (B) of ECS sample aged at 750°C for 1,000h. A-1, B-1: Primary Z-phase; B-2: η-Phase.

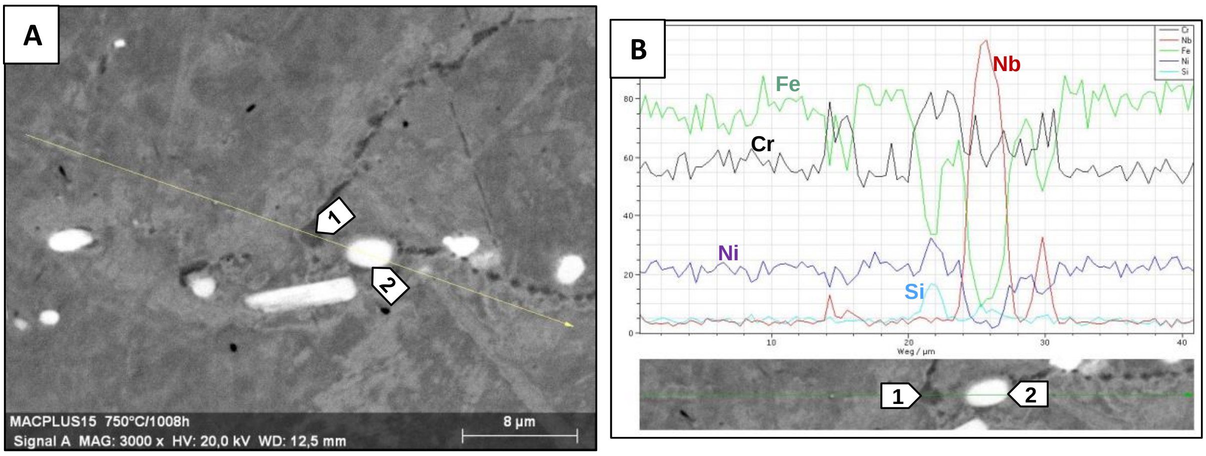

Figure 53: Grain boundary (A) and EDS analysis of η-phase and primary Z-phase (B) in ECS sample aged at 750°C for 1,000h. A-1, B-1: η-phase; A-2, B-2: Primary Z-phase.

6.4.4 Discussion

Results of the creep strength and microstructure evolution of modified austenitic steel are shown above. In this chapter, the failure of the modified steel, using the results from microstructure and precipitation calculation evolution will be discussed. Finally, the objectives of the modification process will be evaluated.

Limited short term creep tests at 650 and 750°C of modified 25Cr-20Ni-Nb-N are performed. The creep tests are performed for EQ and ECS samples. The rupture times of the modified composition and the reference material HR3C [24] are shown in Figure 54. When the rupture times at 650°C is analysed, it can be seen that the modified steel (marked in blue) is ruptured significantly earlier, compared to the average rupture time of HR3C. The reason for that will be discussed later. At 750°C (marked in red) the rupture times are close to the average and particularly within the scatter of HR3C. Further on, it can be seen that the rupture times of modified composition (ECS samples) are closer to HR3C with increasing exposure time and decreasing load at 750°C: Δt_R ($t_{R\_HR3C} - t_{R\_ECS}$) = 92h for 143MPa, Δt_R=51h for 132MPa and Δt_R=18h for 110MPa.

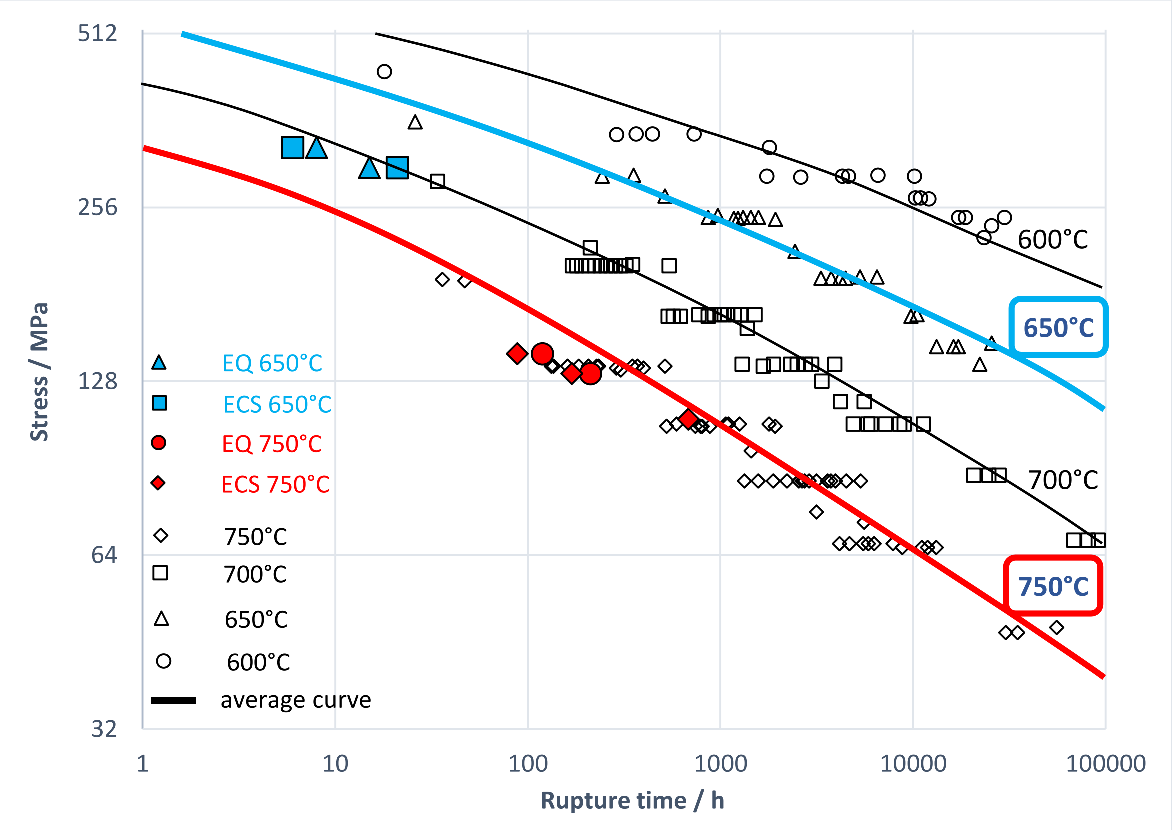

Figure 54: Creep rupture time of HR3C and modified 25Cr-20Ni-Nb-N austenitic steel.

SEM investigations are performed to investigate the microstructure of the modified steel. Due to the low resolution of the SEM, only large precipitates, and fracture surface could be investigated. Considering the fracture surface, the grain boundaries could be clearly seen, which indicates that all creep samples are fractured along the grain boundaries. No significant reduction of area was observed, therefore a low ductility for the modified steel is expected. Considering the precipitates evolution in the modified steel, primary Z-phase precipitates are present in all samples. In addition to that, η-phase, having a high Cr-, Ni- and Si-content, is found along the grain boundaries at 750°C after 1,000h ageing. It is expected that η-phase is also present at 650°C after 1,000h, but due to the low resolution of the SEM, it could not be detected. No $M_{23}C_6$ precipitates are found at 650 and 750°C up to 1,000h, this is either due to the high presence of the η-phase shifting the formation of $M_{23}C_6$ to later times or due to the low size of $M_{23}C_6$ which could not be detected by the SEM. No σ-phase precipitates are found at 650 and 750°C after 1,000h. In comparison to that, a high presence of σ-phase precipitates at grain boundary triple points is found in the non-modified composition, see chapter 5.1.2 on page 37.

Due to the limited findings out of the experimental investigations, less statements about the failure mechanism in the modified composition can be done. It is observed that the failure always occurs along grain boundaries, this indicates that the grain boundaries are weaker than the matrix. The primary Z-phase precipitates are randomly distributed (most of them are inside grains), and, if primary Z-phase precipitates would cause the failure, cracks inside grains should occur, but this was not observed.

The intergranular failure occurs even after short exposure times, this is an indication that embrittlement has taken place. This is also supported by the low reduction of area. There are many possible reasons for the low ductility, one of them are coarse particles like primary Z-phase which would cause a dimple rupture, but this is not observed. However, only a limited number of investigations were performed where no statement about the cause of low ductility can be done.

It is shown above that the modified steel is ruptured significant earlier at 650°C compared to the average rupture time of HR3C. That was not the case for 750°C creep exposure, where a longer rupture time is observed. In order to discuss the early failure at 650°C, additional precipitation calculations are performed, using the composition from the chemical analysis of the modified steel in Table 14 on page 85. Two different calculations at 650°C for 8h and 750°C for 682h are performed. These calculations should represent the precipitation distribution of ECS creep exposed samples at 650°C/6h and 750°C/682h. The precipitates phase fractions are shown in Figure 55. As shown, the phase fractions of the grain boundary precipitate such as $M_{23}C_6$.gb (0.0008% at 650°C and 0.70% at 750°C) and η-phase (0.03% at 650°C and 1,63% at 750°C) are much lower at 650°C compared to 750°C. This low phase fractions of $M_{23}C_6$.gb and η-phase may contribute to a low grain boundary strength and further on to preliminary failure at 650°C. In Figure 27 and Figure 28 on page 63 it is shown that the secondary Z-phase precipitates are of great importance for the creep strength. The phase fraction of the secondary Z-phase (0.21% at 650°C and 0,37% at 750°C), which form inside the matrix, is high at 650 and 750°C. As a consequence, the matrix strength is high. The high matrix strength, together with low grain boundary strength is probably the reason why the material failure always occurs along the grain boundaries.

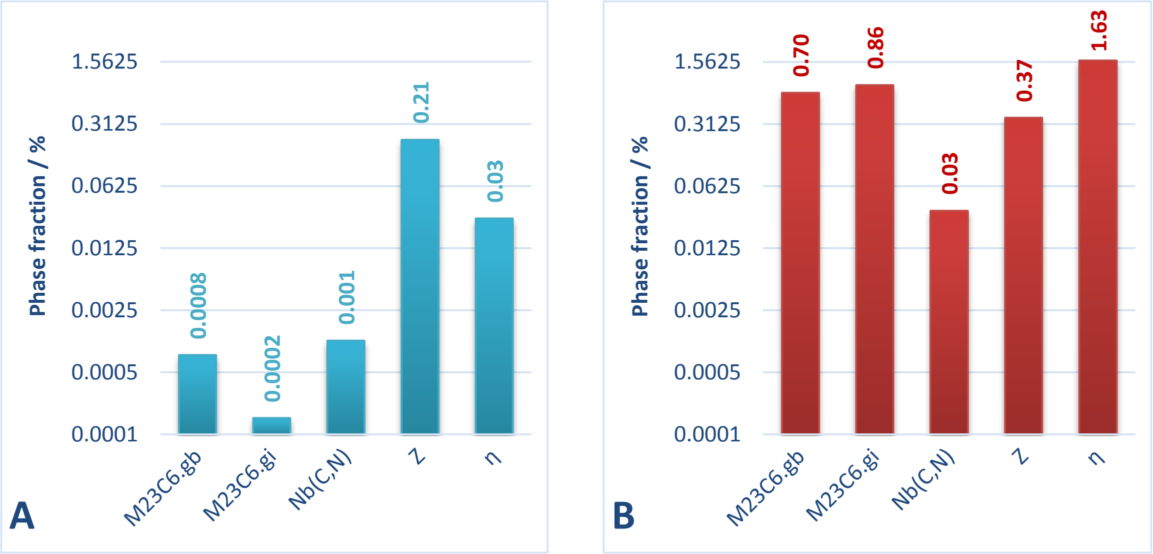

Figure 55: Phase fractions of precipitates at 650°C after 6h (A) and at 750°C after 682h (B) of modified austenitic steel.

As mentioned above, it is assumed that the low phase fraction of grain boundary precipitates may contribute to the low creep strength. In order to investigate this assumption, a heat treatment (before creep loading) should be applied to form a sufficient amount of grain boundary precipitates. According to MatCalc calculations, an isothermal ageing at 850°C for 20h would form a total phase fraction of grain boundary precipitates of 1.9% (=1.3% $M_{23}C_6$.gb + 0.6% η-phase). This is significantly higher compared to ruptured ECS sample at 650°C/6h and it is expected to be sufficient to investigate the effect of grain boundary precipitates on the creep rupture time.

The creep strength, microstructure and failure of modified steel is discussed above. When the objectives (see chapter 6.1 on page 74) are analysed, following statements can be made:

Related to 1st objective: All chemical elements (except niobium) of modified composition are within the ASTM standard of 25Cr-20Ni-Nb-N steel, see Table 17. Niobium amount (0.61%) is slightly higher than allowed (0.6%). Tungsten and copper is not defined in the standard, but amounts up to 0.5% are allowed.

Table 17: ASTM standard and heat composition of modified 25Cr-20Ni-Nb-N in wt.%.

	C	**Si**	**Mn**	**Cr**	**Ni**	**Nb**	**N**	**W**	**Cu**
MAX	0.100	0.75	2.0	26.0	23.0	0.60	0.350	-	-
Heat	**0.075**	**0.39**	**1.17**	**25.27**	**20.3**	**0.61**	**0.34**	**0.50**	**0.50**
MIN	0.040	0.0	0.0	24.0	17.0	0.20	0.150	-	-

Related to 2nd objective: The chromium content is higher than 25wt%, this should guarantee a sufficient corrosion resistance at high temperature.

Related to 3rd objective: The rapidly growing σ-phase in the non-modified steel was not experimentally observed in the modified steel. The formation of σ-phase in modified steel is successfully suppressed by high nitrogen content, as explained and predicted by the precipitation calculation in chapter 6.2 on page 76.

Related to 4th objective: As mentioned at the beginning of this chapter, the creep rupture time of modified composition at 650°C is significantly lower compared to the HR3C, whereas at 750°C the creep rupture time is within the scatter of HR3C. The loss in creep strength is quite alarming since the modified composition is within the ASTM standard. Furthermore, creep strength calculations of modified composition did not predict any loss in creep strength. The present creep modelling approach can be used when creep cavitation is the main mechanism for failure. For stainless steels like 304, 316, 321 and 347 it is assumed that the embrittlement is due to creep cavitation. The results for these steels are in good agreement with observations and the creep model results are not very different if it is assumed ductile or brittle rupture. For the modified austenitic steel the embrittlement mechanism is not known, which makes it difficult to predict the rupture time. It is unlikely that cavitation on its own would cause the observed embrittlement in the modified steel. However, further investigations have to be done in turn of the embrittlement of modified steel. Finally, it can be said that the 4th objective is not achieved.

Related to 5th objective: The performed ageing treatment of 1,000h and low resolution of SEM were not sufficient to analyse the grain boundary precipitates in a reasonable way.

Therefore, no statement about grain boundary precipitates can be done. Longer ageing treatments have to be applied in order to evaluate the grain boundary precipitates.

A high corrosion resistance and high creep strength are one of the most important properties of advanced austenitic steels for applications in USC and A-USC power plants. A high corrosion resistance is successfully achieved by high chromium content and absence of σ-phase, but the creep strength is lost. Taking this into consideration, it is expected that this modified composition is not suitable for USC and A-USC power plant applications.

6.4.5 Summary

Microstructure investigations of modified composition of an austenitic steel 25Cr-20Ni-Nb-N are carried out for creep exposed and thermally aged samples at 650 and 750°C. For the investigations LOM and SEM are used. The investigations are carried out by the author at the Institute of Material Science and Welding. The experimental results are summarized as follows:

- The creep rupture time of modified composition at 650°C is significantly lower compared to HR3C steel, whereas at 750°C it is within the scatter of HR3C.
- All creep samples show intergranular rupture and low reduction of area, indicating that embrittlement has taken place.
- Primary Z-phase precipitates are observed in as-received and all thermally exposed samples.
- At 650°C after 1,000h ageing no secondary precipitates are observed. At 750°C after 1,000h, η-phase precipitates on grain boundaries are found.
- In all investigated samples, no σ-phase precipitates are observed. This finding confirms the accuracy of the precipitation calculations where the σ-phase is suppressed by high nitrogen content.

Finally, it can be summarized that the σ-phase in the modified composition is supressed but creep strength is significantly lost.

7 Summary

The present thesis deals with the microstructure investigation and calculation of precipitation evolution in an advanced 25Cr-20Ni-Nb-N austenitic steel for USC and A-USC power plant applications. Additionally, the hardening mechanisms during creep are evaluated and a modified composition of a 25Cr-20Ni-Nb-N steel is developed which suppress the formation of σ-phase. The main findings can be summarized as follows:

- Microstructure investigations are carried out for thermally aged samples at 650 and 750°C for 1,000h, 3,000h and 10,000h. Five different precipitates Z-phase, $M_{23}C_6$, Nb(C,N), η ($Cr_3Ni_2Si(C,N)$), σ-phase and two different oxides Al- and Si-oxide are experimentally found. After long ageing times, the brittle acting σ-phase is found to be a dominant phase on the grain boundaries. Furthermore, the findings about the η-phase are used to implement this phase into the thermodynamic database of MatCalc.
- Equilibrium-calculations by MatCalc are carried out where it is shown when Cr_2N is suspended, five different precipitates phases in the temperature range between 400 and 1600°C are predicted: Nb(C,N), Z-phase, $M_{23}C_6$, σ-phase and η-phase. All these phases are also found experimentally.
- Scheil-calculations by MatCalc are carried out to evaluate the amount of primary precipitates in the 25Cr-20Ni-Nb-N austenitic steel. It is found that the primary Z-phase is the most prominent primary phase.
- Precipitation calculations by MatCalc are carried out considering a solution- and service-treatment at 650 and 750°C for 100,000h. The precipitation evolutions are compared with experimental results and analysed in detail. The main findings can be summarized as follows:

  - For the precipitation calculations, eight precipitates are considered: $M_{23}C_6$, σ, primary Z, secondary Z, primary Nb(C,N), secondary Nb(C,N), η (Cr_3Ni_2SiN) and G.
  - The σ-phase is found to be the most dominant phase on the grain boundaries at long ageing time.
  - With the help of the precipitation calculations and experimental investigations it is found that the silicon-rich phase in the 25Cr-20Ni-Nb-N steel is more likely a η-phase and not a G-phase.
  - The interactions between the precipitates are studied and compared with literature. Assumptions from the literature such as the interaction between MX precipitates with $M_{23}C_6$ and Z-phase are analysed and explained in detail.
- The creep strength is calculated in collaboration with Prof. Sandström (KTH Stockholm). There are three main contributions to the creep strength from dislocations, precipitates and elements in solid solution. The contribution from the dislocations is found to be the highest one.
- A modification of the 25Cr-20Ni-Nb-N chemical composition within the ASTM standard is performed. By the help of the precipitation calculation a modified composition is defined where the σ-phase formation is suppressed. The chromium content of the modified composition is kept high to increase the corrosion resistance.
- Superheater tubes using the modified chemical composition are extruded and creep samples are manufactured. A limited amount of short term creep test at 650 and 750°C are performed to analyse the creep rupture time and the presence of σ-phase precipitates.

Finally, it can be summarized, that a significant amount of coarse σ-phase precipitates in an advanced 25Cr-20Ni-Nb-N are observed. With the help of the precipitation calculation with MatCalc and creep strength modelling by Prof. Sandström (KTH), a modified composition within the ASTM standard is defined. Using this modified composition, superheater tubes are produced, where on the one hand no σ-phase is observed, but on the other hand a significant lower creep strength is measured.

8 Outlook

Extensive investigations and calculation of the precipitation evolution of an advanced 25Cr-20Ni-Nb-N austenitic steel are carried out. Therefore, findings and compromises have been made, which have to be analysed more in detail:

- The TEM-EDS analysis of the secondary Z-phase reveal a significant high amount of nickel (up to 30%). Such high amounts of nickel are not common for this type of precipitate. Further structure analysis of Z-phase in austenitic steels would be necessary to analyse the Z-phase in detail.
- In [36] creep exposed sample of 25Cr-20Ni-Nb-N steel after 88,363h is investigated. In this long time creep exposed sample, which is assumed to be close to an equilibrium condition, no Cr_2N phase is found. Similar results are reported by Sourmail [27], who writes that Cr_2N is unlikely when Z-phase is present in austenitic steels. These findings are not in agreement with MatCalc where Cr_2N is predicted as an equilibrium phase. Further investigations and improvement of Cr_2N have to be done in order to predict Cr_2N phase correctly.
- It is experimentally shown that the σ-phase is present at 750°C in the 25Cr-20Ni-Nb-N austenitic steel. In order to stabilize the σ-phase at 750°C an interface energy correction is applied, which is not a reasonable solution. Further improvement of thermo-kinetic modelling of σ-phase at high temperature is necessary to avoid the interface energy correction.
- The twin boundaries in austenitic steels are important nucleation sites for many precipitates such as $M_{23}C_6$ or η-phase. Especially at longer ageing times, when the precipitates starts to form in grain interior, the twin boundaries as nucleation sites becomes very important. Therefore, it is necessary to develop a twin boundary nucleation site model in MatCalc.

- For the non-modified composition it was found by simulation that the temperature cycle of the manufacturing process does not have a significant influence on the precipitation evolution during service. Such simulations were not applied to the modified composition. Therefore, one further task for the outlook is to collect the data (heating-, cooling-rates and holding times) of the temperature cycle during of the manufacturing process and to apply it to the precipitation calculation of modified steel.

The modified composition is investigated by a limited number of short-term creep tests. Further test and investigations are necessary in order to investigate the modified composition more in detail:

- Further long-term creep tests at 650, 700 and 750°C are necessary to evaluate the creep strength of modified 25Cr-20Ni-Nb-N austenitic steel.
- The formation of σ-phase is analysed by a short-term ageing up to 1,000h. Longer ageing tests are necessary to evaluate the presence of σ-phase in the modified steel.
- It was shown that the σ-phase formation cause a depletion of chromium in the matrix. Since no σ-phase was observed in the modified composition, a higher corrosion resistance is expected. Therefore, corrosion tests of modified composition should be applied and the results should be compared with the non-modified composition.
- The intergranular failure after short exposure times and low reduction of area is an indication that embrittlement has taken place in the modified composition. The reasons for that embrittlement could not be clarified and further investigations have to be done in order to analyse this phenomenon.
- Significant low short-term creep strength of the modified composition is measured. This was not predicted by the creep strength calculations. One possible explanation for the different prediction of creep strength could be the embrittlement. The applied creep strength model is suitable for austenitic steels where the embrittlement is caused by creep cavitation, which is probably not the only cause for the degradation in the modified steel. The cause of embrittlement has to be investigated in order to evaluate the applicability of the present creep model on the modified austenitic steel.

- A further opportunity to calculate the creep strength is to apply another creep strength model. Recently a new creep strength model for the martensitic steels has been developed by Yadav et. al [86] at the Institute of Material Science and Welding. Some input parameters such as dislocation density have to be investigated in order to adapt the model to the present austenitic steel.

9 References

[1] *World Energy Outlook 2013*. Paris: Organisation for Economic Co-operation and Development OECD, 2004.

[2] J. M. Wheeldon and J. P. Shingledecker, “Materials for boilers operating under supercritical steam conditions,” in *Ultra-supercritical coal power plants : Materials, technologies and optimisation*, D. Zhang, Ed. Woodhead, 2013, pp. 81–103.

[3] G. Booras and N. Holt, “Pulverized coal and igcc plant cost and performance estimates,” *Gasif. Technol. Washingt. DC, Oct. 3-6*, 2004.

[4] R. Viswanathan, J. F. Henry, J. Tanzosh, G. Stanko, J. Shingledecker, B. Vitalis, and R. Purgert, “U.S. Program on Materials Technology for Ultra-Supercritical Coal Power Plants,” *J. Mater. Eng. Perform.*, vol. 14, no. 3, pp. 281–292, Jun. 2005.

[5] O. Tassa, S. Matera, R. Sandström, J. Zurek, and M. Farooq, “Microstructure Evolution After Long Term High Temperature Exposure of Austenitic 22-25Cr Austenitic Stainless Steels,” Liège, Belgium, in *Proc.: 10th Liège Conference on Materials for Advanced Power Engineering*, 2014.

[6] S. Vujic, C. Beal, C. Sommitsch, F. Muhammad, R. Sandström, and J. Zurek, “Modelling and optimizing precipitation in creep resistant austenitic steel 25Cr-20Ni-Nb-N,” Waikoloa, Hawaii, in *Proc.: Advances in Materials Technology for Fossil Power Plants*, 2013.

[7] R. Bürgel, H. J. Maier, and N. Thomas, *Handbuch Hochtemperatur-Werkstofftechnik*, 4th ed. Vieweg+Teubner, 1998.

[8] R. Sandström, M. Farooq, and B. Ivarsson, “Influence of particle formation during long time ageing on mechanical properties in the austenitic stainless steel 310,” *Mater. High*

Temp., vol. 29, no. 1, pp. 1–7, Mar. 2012.

[9] Y. Yin, R. Faulkner, and F. Starr, “Austenitic steels and alloys for power plants,” in *Structural Alloys for Power Plants*, A. Shirzadi and S. Jackson, Eds. Elsevier, 2014, pp. 105–152.

[10] J. Svoboda, F. D. Fischer, P. Fratzl, and E. Kozeschnik, “Modelling of kinetics in multi-component multi-phase systems with spherical precipitates,” *Mater. Sci. Eng. A*, vol. 385, no. 1–2, pp. 166–174, Nov. 2004.

[11] E. Kozeschnik, J. Svoboda, P. Fratzl, and F. D. Fischer, “Modelling of kinetics in multi-component multi-phase systems with spherical precipitates,” *Mater. Sci. Eng. A*, vol. 385, no. 1–2, pp. 157–165, Nov. 2004.

[12] E. Kozeschnik, J. Svoboda, and F. D. Fischer, “Modified evolution equations for the precipitation kinetics of complex phases in multi-component systems,” *Calphad*, vol. 28, no. 4, pp. 379–382, Dec. 2004.

[13] R. Sandström, M. Farooq, and J. Zurek, “Basic creep models for 25Cr20NiNbN austenitic stainless steels,” *Mater. Res. Innov.*, vol. 17, no. 5, pp. 355–359, 2013.

[14] R. Sandström and J. Hallgren, “The role of creep in stress strain curves for copper,” *J. Nucl. Mater.*, vol. 422, no. 1–3, pp. 51–57, Mar. 2012.

[15] P. A. Korzhavyi and R. Sandström, “First-principles evaluation of the effect of alloying elements on the lattice parameter of a 23Cr25NiWCuCo austenitic stainless steel to model solid solution hardening contribution to the creep strength,” *Mater. Sci. Eng. A*, vol. 626, pp. 213–219, 2015.

[16] R. Sandström, “Basic model for primary and secondary creep in copper,” *Acta Mater.*, vol. 60, no. 1, pp. 314–322, Jan. 2012.

[17] R. Sandström and R. Wu, “Influence of phosphorus on the creep ductility of copper,” *J. Nucl. Mater.*, vol. 441, no. 1–3, pp. 364–371, Oct. 2013.

[18] R. Sandström and H. C. M. Andersson, “Creep in phosphorus alloyed copper during power-law breakdown,” *J. Nucl. Mater.*, vol. 372, no. 1, pp. 76–88, Jan. 2008.

[19] D. Kothari and P. M. V. Subbarao, “Power Generation,” in *Handbook of Mechanical Engineering*, K.-H. Grote and E. K. Antonsson, Eds. Springer, 2009, pp. 1361–1419.

[20] J. M. Wheeldon and J. N. Phillips, “An economic and engineering analysis of a 700 ° C advanced ultra-supercritical pulverized coal power plant,” in *Ultra-supercritical coal power plants : Materials, technologies and optimisation*, Elsevier, 2013, pp. 229–243.

[21] F. Starr, “High temperature materials issues in the design and operation of coal-fired steam turbines and plant,” in *Structural Alloys for Power Plants*, A. Shirzadi and S. Jackson, Eds. Elsevier, 2014, pp. 36–68.

[22] M. Fukuda, E. Saito, and H. Semba, “Advanced USC technology development in Japan,” Liège, Belgium, in *Proc.: Materials for Advanced Power Engineering*, 2010.

[23] F. Masuyama, “Alloy development and material issues with increasing steam temperature,” Hilton Head Island, South Carolina, USA, in *Proc.: Advances in Materials Technology for Fossil Power Plants*, 2004.

[24] M. Igarashi, “25Cr-20Ni-Nb-N steel,” in *Landolt Börnstein*, vol. 2B, K. Yagi, G. Merckling, T.-U. Kern, H. Irie, and H. Warlimont, Eds. Springer, 2004, pp. 292–296.

[25] Nippon Steel & Sumitomo Metal, “Seamless Steel Tubes and Pipes for Boilers,” Tokyo, Japan, 2013.

[26] TUBACEX, “Manufactoring process,” 2014. [Online]. Available: http://www.tubacex.es/en/.

[27] T. Sourmail, “Literature review Precipitation in creep resistant austenitic stainless steels,” *Mater. Sci. Technol.*, vol. 17, no. 1, pp. 1–14, 2001.

[28] T. Sourmail and H. Bhadeshia, “Microstructural Evolution in Two Variants of NF709 at 1023 and 1073 K,” *Metall. Mater. Trans. A*, 2005.

[29] J. H. Yoon, E. P. Yoon, and B. S. Lee, “Correlation of chemistry, microstructure and ductile fracture behaviours of niobium-stabilized austenitic stainless steel at elevated temperature,” *Scr. Mater.*, vol. 57, no. 1, pp. 25–28, 2007.

[30] O. Yoo, Y.-J. Oh, B.-S. Lee, and S. W. Nam, “The effect of the carbon and nitrogen contents on the fracture toughness of Type 347 austenitic stainless steels,” *Mater. Sci. Eng. A*, vol. 405, no. 1–2, pp. 147–157, 2005.

[31] A. F. Padilha and P. R. Rios, “Decomposition of Austenite in Austenitic Stainless Steels,” *ISIJ Int.*, vol. 42, no. 4, pp. 325–327, 2002.

[32] K. Nobuyoshi, M. Igarashi, Y. Minami, H. Mimura, F. Masuyama, M. Prager, and P. R. Boyles, “Field Test Results of Newly Developed Austenitic Steels in the Eddystone Unit No.1 Boiler,” San Antonio, Texas, USA, in *Proc.: Creep and Fatigue at Elevated Temperatures (CREEP)*, 2007, no. 1.

[33] F. Yuanyuan, Z. Jie, and L. Xiaona, “PRECIPITATES IN HR3C STEEL AGED AT HIGH TEMPERATURE,” *ACTA Metall. Sin.*, vol. 46, no. 7, pp. 844–849, 2010.

[34] C. Chi, H. Yu, and X. Xie, *Advanced Austenitic Heat-Resistant Steels for Ultra-Super-Critical (USC) Fossil Power Plants*. InTech, 2011.

[35] E. J. Giordani, V. a. Guimarães, T. B. Pinto, and I. Ferreira, “Effect of precipitates on the corrosion-fatigue crack initiation of ISO 5832-9 stainless steel biomaterial,” *Int. J. Fatigue*, vol. 26, no. 10, pp. 1129–1136, 2004.

[36] A. Iseda, H. Okada, H. Semba, and M. Igarashi, “LONG-TERM CREEP PROPERTIES AND MICROSTRUCTURE OF SUPER304H , TP347HFG AND HR3C FOR ADVANCED USC BOILERS,” *Energy Mater.*, vol. 2, no. 4, pp. 199–206, 2007.

[37] Y. Zun, C. Hui, and L. Hongguo, “Performance on New Heat-resistant Steel HR3C in the Ultra-supercritical Units After Service at High Temperature for 25 000 Hours,” Wuhan, China, in *Proc.: Chinese Society for Electrical Engineering*, 2011, vol. 8013.

[38] H. Okada, M. Igarashi, S. Yamamoto, O. Miyahara, A. Iseda, N. Komai, and F. Masuyama, “Long-Term Service Experience With Advanced Austenitic Alloys in Eddystone Power Station,” San Antonio, Texas, USA, in *Proc.: Creep and Fatigue at Elevated Temperatures (CREEP)*, 2007.

[39] H. U. Hong and S. W. Nam, “The occurrence of grain boundary serration and its effect on the M23C6 carbide characteristics in an AISI 316 stainless steel,” *Mater. Sci. Eng. A*, vol. 332, no. 1–2, pp. 255–261, 2002.

[40] U. K. Mudali, P. Shankar, D. Sundararaman, and R. K. Dayal, “Microstructural and electrochemical studies in thermally aged type 316LN stainless steels,” *Mater. Sci. Technol.*, vol. 15, no. 12, pp. 1451–1453, 1999.

[41] J. Barcik, “Mechanism of Sigma - phase precipitation in Cr-Ni austenitic steels,” *Mater. Sci. Technol.*, vol. 4, pp. 5–15, 1988.

[42] J. Barcik, “The kinetics of σ-phase precipitation in AISI310 and AISI316 steels,” *Metall. Trans. A*, vol. 14, no. 3, pp. 635–641, 1983.

[43] M. Farooq, R. Sandström, and M. a Lundberg, “Precipitation during long time ageing in the austenitic stainless steel 310,” *Mater. High Temp.*, vol. 29, no. 1, pp. 8–16, Mar. 2012.

[44] D. Li, Y. Gao, J. Tan, F. Wang, and J. Zhang, “Effect of σ-Phase on the creep properties of Cr25Ni20 stainless steel,” *Scr. Metall.*, vol. 23, pp. 1319–1321, 1989.

[45] Y. Minami, H. Kimura, and Y. Ihara, “Microstructural changes in austenitic stainless steels during long-term aging,” *Mater. Sci. Technol.*, vol. 2, pp. 795–806, 1986.

[46] R. F. A. Jargelius-Pettersson, “Precipitation in a nitrogen-alloyed stainless steel at 850°C,” *Scr. Metall. Mater.*, vol. 28, pp. 1399–1403, 1993.

[47] R. C. Ecob, R. C. Lobb, and V. L. Kohler, “The formation of G-phase in 20/25 Nb stainless steel AGR fuel cladding alloy and its effect on creep properties,” *J. Mater. Sci.*, vol. 22, no. 8, pp. 2867–2880, 1987.

[48] D. J. Powell, I. R. Pilkington, and D. A. Miller, “THE PRECIPITATION CHARACTERISTICS OF 20 % Cr / 25 % Ni-Nb STABILISED STAINLESS STEEL,” vol. 36, no. 3, pp. 713–724, 1988.

[49] E. Kozeschnik, J. Svoboda, R. Radis, and F. D. Fischer, “Mean-field model for the growth and coarsening of stoichiometric precipitates at grain boundaries,” *Model. Simul. Mater. Sci. Eng.*, vol. 18, pp. 1–19, Jan. 2010.

[50] R. Sandström, “Creep strength of austenitic stainless steels for boiler applications,” in *Coal Power Plant Materials and Life Assessment: Developments and Applications*, A. Shibli, Ed. Elsevier, 2014, pp. 127–146.

[51] P. Ambrosi and C. Schwink, “Slip line length of copper single crystals oriented along [100] and [111],” *Scr. Metall.*, vol. 12, no. 3, pp. 303–308, 1978.

[52] Y. Kawasaki and T. Takeuchi, “Cell structures in copper single crystals deformed in the [001] and [111] axes,” *Scr. Metall.*, vol. 14, no. 2, pp. 183–188, 1980.

[53] N. D. Ryan, H. J. McQueen, and E. Evangelista, “Dynamic recovery and strain hardening in the hot deformation of type 317 stainless steel,” *Mater. Sci. Eng.*, vol. 81, pp. 259–272, 1986.

[54] J. Hirth and J. Lothe, *Theory of dislocations*, 2nd ed. New York: Wiley, 1982.

[55] A. F. Smith, “Low-Temperature Diffusion of Chromium in a Fine-Grained Austenitic Stainless Steel with Varying Dislocation Densities,” *Met. Sci.*, vol. 9, no. 1, pp. 425–429, 1975.

[56] M. Kassner, “Creep Behavior of Particle-Strengthened Alloys,” in *Fundamentals of Creep in Metals and Alloys*, 3rd ed., Butterworth-Heinemann, 2015, pp. 163–181.

[57] L. M. Brown and R. K. Ham, “Strengthening Method in Crystals,” in *Elsevier*, A. Kelly and R. B. Nicholson, Eds. Amsterdam: Elsevier, 1971, pp. 22–28.

[58] R. Lagneborg, “Bypassing of dislocations past particles by a climb mechanism,” *Scr. Metall.*, vol. 7, pp. 605–613, 1973.

[59] W. Blum and B. Reppich, *Creep Behaoiour of Crystalline Solids*. Swansea, U.K.: Pineridge Press, 1985.

[60] J. Rösler and E. Arzt, “The kinetics of dislocation climb over hard particles—I. Climb without attractive particle-dislocation interaction,” *Acta Metall.*, vol. 36, no. 4, pp. 1043–1051, 1988.

[61] J. Eliasson, Å. Gustafson, and R. Sandström, “Kinetic modelling of the influence of particles on creep strength,” *Key Eng. Mater.*, vol. 171/174, pp. 277–284, 2000.

[62] H. Magnusson and R. Sandström, “The role of dislocation climb across particles at creep conditions in 9 to 12 pct Cr steel,” *Metall. Mater. Trans. A*, vol. 38, no. 10, pp. 2428–2434, 2007.

[63] J. W. Martin, *Precipitation Hardening*. Butterworth-Heinemann, 1998.

[64] R. Wang, S. Wang, and X. Wu, “Edge dislocation core structures in FCC metals determined from ab initio calculations combined with the improved Peierls–Nabarro equation,” *Phys. Scr.*, vol. 83, no. 4, pp. 1–7, 2011.

[65] M. D. Mathew, K. Laha, and V. Ganesan, “Improving creep strength of 316L stainless steel by alloying with nitrogen,” *Mater. Sci. Eng. A*, vol. 535, pp. 76–83, Feb. 2012.

[66] C. Templier, J. C. Stinville, P. Villechaise, P. O. Renault, G. Abrasonis, J. P. Rivière, A. Martinavičius, and M. Drouet, “On lattice plane rotation and crystallographic structure of the expanded austenite in plasma nitrided AISI 316L steel,” *Surf. Coatings Technol.*,

vol. 204, no. 16–17, pp. 2551–2558, May 2010.

[67] S. Vujic, M. Farooq, B. Sonderegger, R. Sandström, and C. Sommitsch, “Numerical Modelling and Validation of Precipitation Kinetics in Advanced Creep Resistant Austenitic Steel,” *Comput. METHODS Mater. Sci.*, vol. 12, no. 3, pp. 175–182, 2012.

[68] E. Kozeschnik, E. Rindler, and B. Buchmayr, “Scheil-Gulliver simulation with partial redistribution of fast diffusers and simultaneous solid-solid phase transformations,” *Int. J. Mater. Res.*, vol. 98, no. 9, pp. 826–831, 2009.

[69] W. Rindler, E. Kozeschnik, and B. Buchmayr, “Computer simulation of the brittle-temperature-range (BTR) for hot cracking in steels,” *Steel Res.*, vol. 71, no. 11, pp. 460–465, 2000.

[70] E. Kozeschnik, “A scheil-gulliver model with back-diffusion applied to the microsegregation of chromium in Fe-Cr-C alloys,” *Metallurgical and Materials Transactions A*, vol. 31, no. 6. pp. 1682–1684, 2000.

[71] E. Kozeschnik, “Treatment of heterogeneous nucleation,” 2011. [Online]. Available: http://matcalc.tuwien.ac.at.

[72] B. Sonderegger and E. Kozeschnik, “Generalized nearest-neighbor broken-bond analysis of randomly oriented coherent interfaces in multicomponent Fcc and Bcc structures,” *Metall. Mater. Trans. A Phys. Metall. Mater. Sci.*, vol. 40, no. 3, pp. 499–510, 2009.

[73] B. Sonderegger and E. Kozeschnik, “Interfacial Energy of Diffuse Phase Boundaries in the Generalized Broken-Bond Approach,” *Metall. Mater. Trans. A*, vol. 41, no. 12, pp. 3262–3269, Jul. 2010.

[74] E. Povoden-Karadeniz, S. Vujic, and E. Kozeschnik, “Thermodynamic modeling and simulation of time-temperature-precipitation diagrams in stainless steel,” San Sebastian, Spain, in *Proc.: CALPHAD XLII*, 2013.

[75] R. Radis, “Numerical simulation of the precipitation kinetics of nitrides and carbides in microalloyed steel,” 2010.

[76] S. Vujic, R. Sandström, and C. Sommitsch, “Precipitation evolution and creep strength modelling of 25Cr20NiNbN austenitic steel,” *Mater. High Temp.*, no. 0, pp. 1–12, 2015.

[77] B. Sonderegger and E. Kozeschnik, “Particle strengthening in fcc crystals with prolate and oblate precipitates,” *Scr. Mater.*, vol. 66, no. 1, pp. 52–55, 2012.

[78] B. Sonderegger, I. Holzer, E. Kozeschnik, and C. Sommitsch, "Particle distance distributions and their effect on precipitation strengthening," *Comput. Methods Mater. Sci.*, vol. 11, no. 1, pp. 148–153, 2011.

[79] S. Kihara, "25Cr-20Ni steel," in *Landolt Börnstein*, vol. 2B, K. Yagi, G. Merckling, T.-U. Kern, H. Irie, and H. Warlimont, Eds. Heidelberg: Springer-Verlag GmbH, 2004, pp. 286–291.

[80] R. Sandström, "Creep strength in austenitic stainless steels," Rome, Italy, in *Proc.: Creep and Fracture in High Temperature Components: Design & Life Assessment Issues (ECCC)*, 2014.

[81] J. O. Nilsson, P. R. Howell, and G. L. Dunlop, "Interfacial microstructure and low stress, high temperature creep of an austenitic stainless steel," *Acta Metall.*, vol. 27, no. 2, pp. 179–186, 1979.

[82] I. . Crossland and B. . Clay, "Diffusion creep and its inhibition in a stainless steel," *Acta Metall.*, vol. 25, no. 8, pp. 929–937, 1977.

[83] B. Wilshire, "Observations, theories, and predictions of high-temperature creep behavior," *Metall. Mater. Trans. A*, vol. 33, no. 2, pp. 241–248, 2002.

[84] A. S. Argon and W. C. Moffatt, "Climb of extended edge dislocations," *Acta Metallurgica*, vol. 29, no. 2. pp. 293–299, 1981.

[85] K. Natesan and J. H. Park, "Fireside and steamside corrosion of alloys for USC plants," *Int. J. Hydrogen Energy*, vol. 32, no. 16, pp. 3689–3697, 2007.

[86] S. D. Yadav, M. Schuler, C. Sommitsch, and C. Poletti, "Physical Based Creep Strain Modelling of 9Cr," Rome, Italy, in *Proc.: Creep and Fracture in High Temperature Components: Design & Life Assessment Issues (ECCC)*, 2014.

Appendix

A script is a text file which contain a lot of specific MatCalc commands. Especially when a lot of precipitation evolution calculations have to be done, then the scripts are a useful approach to speed up routine or repetitive operations. After a script file is created, it can be easily modified in order to perform new calculations with for example modified composition and new heat treatment.

On the next eleven pages a script for the calculations of precipitation evolution in the present austenitic steel is presented. The results in chapter 5.2.2 and chapter 6 are obtained with this script.

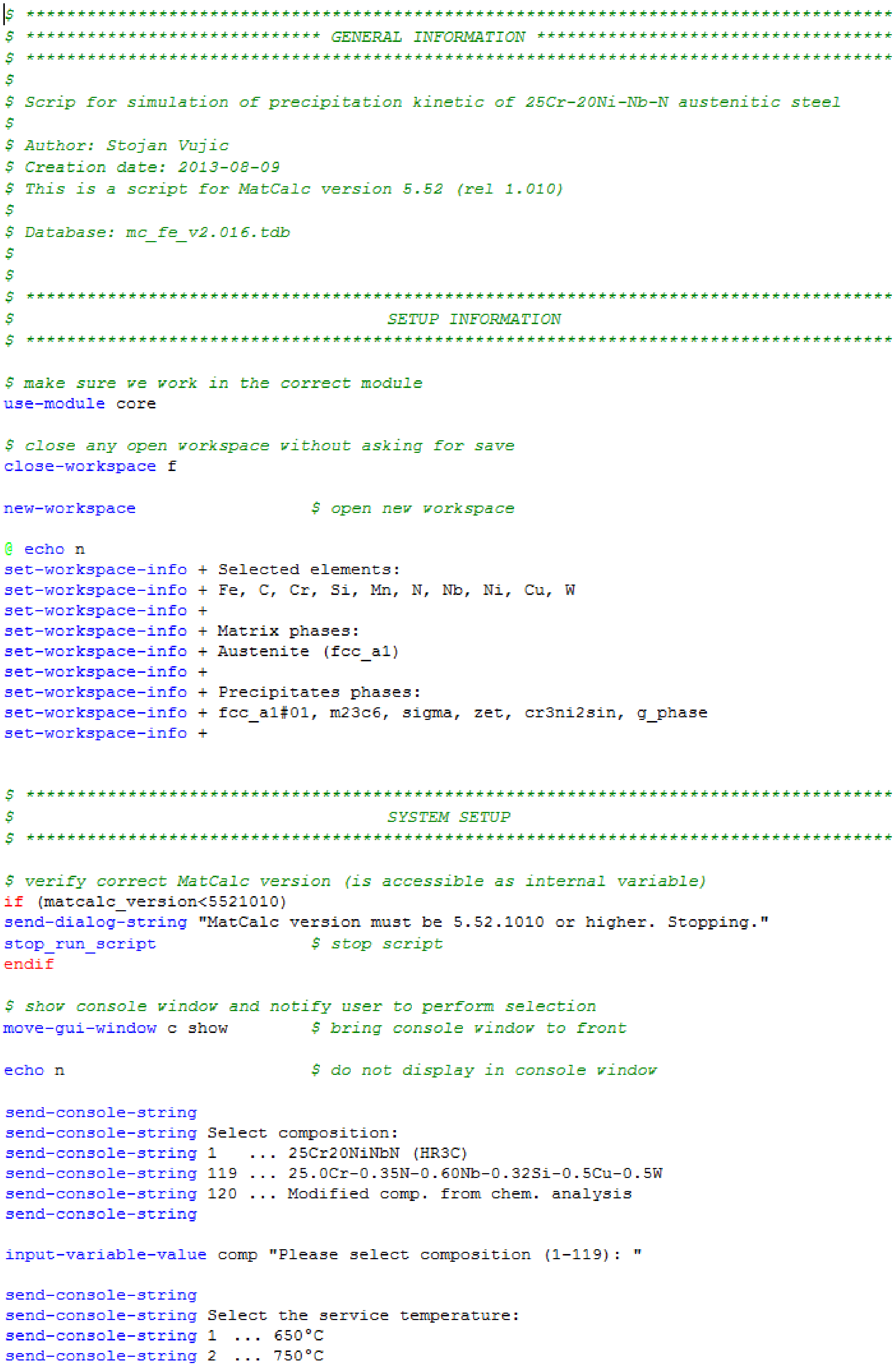

```
$ *************************************************************************************
$ ***************************** GENERAL INFORMATION ***********************************
$ *************************************************************************************
$
$ Scrip for simulation of precipitation kinetic of 25Cr-20Ni-Nb-N austenitic steel
$
$ Author: Stojan Vujic
$ Creation date: 2013-08-09
$ This is a script for MatCalc version 5.52 (rel 1.010)
$
$ Database: mc_fe_v2.016.tdb
$
$
$ *************************************************************************************
$                                     SETUP INFORMATION
$ *************************************************************************************

$ make sure we work in the correct module
use-module core

$ close any open workspace without asking for save
close-workspace f

new-workspace                 $ open new workspace

@ echo n
set-workspace-info + Selected elements:
set-workspace-info + Fe, C, Cr, Si, Mn, N, Nb, Ni, Cu, W
set-workspace-info +
set-workspace-info + Matrix phases:
set-workspace-info + Austenite (fcc_a1)
set-workspace-info +
set-workspace-info + Precipitates phases:
set-workspace-info + fcc_a1#01, m23c6, sigma, zet, cr3ni2sin, g_phase
set-workspace-info +


$ *************************************************************************************
$                                     SYSTEM SETUP
$ *************************************************************************************

$ verify correct MatCalc version (is accessible as internal variable)
if (matcalc_version<5521010)
send-dialog-string "MatCalc version must be 5.52.1010 or higher. Stopping."
stop_run_script               $ stop script
endif

$ show console window and notify user to perform selection
move-gui-window c show        $ bring console window to front

echo n                        $ do not display in console window

send-console-string
send-console-string Select composition:
send-console-string 1   ... 25Cr20NiNbN (HR3C)
send-console-string 119 ... 25.0Cr-0.35N-0.60Nb-0.32Si-0.5Cu-0.5W
send-console-string 120 ... Modified comp. from chem. analysis
send-console-string

input-variable-value comp "Please select composition (1-119): "

send-console-string
send-console-string Select the service temperature:
send-console-string 1  ... 650°C
send-console-string 2  ... 750°C
```

```
send-console-string
input-variable-value servtemp "Please select the calculation (1-2): "
echo y
if (servtemp==1)
    set-variable-value T_s 650
elseif (servtemp==2)
    set-variable-value T_s 750
endif

echo y             $ reset display in console window


$ *************************************************************************************
$                                    GLOBAL VARIABLES
$ *************************************************************************************

set-variable-value ht 5*60               $ 5min heating time to solution temperature
set-variable-value ct 1*60               $ 1min cooling time to room temperature

set-variable-value T_sol 1230            $ selection of solution temperature
set-variable-value time_sol 10*60        $ time for solution annealing

set-variable-value time_ser 100000*3600  $ time for service


$ *************************************************************************************
$                      DATABASES, CHEMICAL COMPOSITION, SELECTED PHASES
$ *************************************************************************************

open-thermo-database mc_fe_v2.016.tdb                $ open thermodynamic database

if (comp==1)
    select-elements C Cr Mn N Nb Ni Si               $ select elements
elseif (comp==119)|(comp==120)
    select-elements C Cr Mn N Nb Ni Si W Cu          $ select elements
endif

select-phases fcc_a1 hcp_a3 m23c6 sigma zet liquid cr3ni2sin g_phase $ select phases

read-thermodyn-database                               $ read thermodynamic database
read-mobility-database mc_fe_v2.005.ddb               $ read diffusion database
read-physical-database PhysData.pdb                   $ read physical database


$ Alloy composition
if (comp==1)
    $ chemical composition by KTH 310NbN
    enter-composition wp C=0,062 Cr=24,7 Si=0,38 Mn=1,2 N=0,182 Nb=0,44 Ni=20,6
elseif (comp==119)
    $ 25%Cr-0.35N-0.6Nb-0.32Si-0.5Cu-0.5W
    enter-composition wp C=0,062 Cr=25,0 Si=0,32 Mn=1,2 N=0,350 Nb=0,60 Ni=20,6
    enter-composition wp W=0.50 Cu=0.50
elseif (comp==120)
    $ Modified composition from chemical analysis
    enter-composition wp C=0,075 Cr=25,27 Si=0,39 Mn=1,17 N=0,34 Nb=0,61 Ni=20,3
    enter-composition wp W=0,46 Cu=0,47
else
    send-dialog-string "selected composition is not available"
    stop-run-script
endif


$ ***************************************************************************************
$                                  CHANGE PHASE STATUS ETC.
$ ***************************************************************************************

change-phase-status fcc_a1#01 f s s               $ suspend fcc_a1#01 phase
```

```
create-new-phase fcc_a1#01 C :Nb%:C,N,VA: NbCN   $ create new phase NbCN


$ ************************************************************************************
$                                    HEAT TREATMENTS
$ ************************************************************************************

$ SOLUTION treatment:
create-heat-treatment solution                           $ create heat treatment

append-ht-segment solution                               $ append segment 0
edit-ht-segment solution . d n austenite                 $ define precipitation domain
edit-ht-segment solution . s 25                          $ define start temperature
edit-ht-segment solution . 3 T_sol ht                    $ Tend + heating time
edit-ht-segment solution . c Heating to solution temperature $ comment

append-ht-segment solution                               $ append segment 1
edit-ht-segment solution . 2 0 time_sol                  $ Tdot + delta_t
edit-ht-segment solution . c Isothermal holding at solution temperature $ comment

append-ht-segment solution                               $ append segment 2
edit-ht-segment solution . 3 25 ct                       $ Tend + cooling time
edit-ht-segment solution . c quenching to room temperature $ comment

$ SERVICE:
create-heat-treatment service                            $ create heat treatment

append-ht-segment service                                $ append segment 0
edit-ht-segment service . d n austenite                  $ define precipitation domain
edit-ht-segment service . s 25                           $ define start temperature
edit-ht-segment service . 3 T_s 30                       $ Tend + delta_t
edit-ht-segment service . c Heating to service temperature $ comment

append-ht-segment service                                $ append segment 1
edit-ht-segment service . 2 0 time_ser                   $ Tdot + delta_t
edit-ht-segment service . c time for service             $ comment


$ ************************************************************************************
$                                 EXPERIMENTAL TABLES
$ ************************************************************************************

$ experimental data
$ r=radii, f=phase fraction, n=number density

$ exp. results for aged specimen at 650°C
$ Mean Radius:
create-global-table 650C_r_Sigma                     $ new table for exp. data
add-table-entry 650C_r_Sigma 1000*3600 520e-09       $ KTH exp. SEM data from table6
add-table-entry 650C_r_Sigma 3000*3600 780e-09       $ KTH exp. SEM data from table6
add-table-entry 650C_r_Sigma 10000*3600 1420e-09     $ KTH exp. SEM data from table6

create-global-table 650C_r_M23C6                     $ new table for exp. data
add-table-entry 650C_r_M23C6 1000*3600 100e-09       $ KTH exp. SEM data from table6
add-table-entry 650C_r_M23C6 3000*3600 190e-09       $ KTH exp. SEM data from table6
add-table-entry 650C_r_M23C6 10000*3600 520e-09      $ KTH exp. SEM data from table6

$ Phase fraction:
create-global-table 650C_f_M23C6                     $ new table for exp. data
add-table-entry 650C_f_M23C6 1000*3600 0.0005        $ KTH exp. from meeting in Essen
add-table-entry 650C_f_M23C6 5000*3600 0.0027        $ KTH exp. from meeting in Essen
add-table-entry 650C_f_M23C6 10000*3600 0.0075       $ KTH exp. from meeting in Essen

create-global-table 650C_f_Sigma                     $ new table for exp. data
add-table-entry 650C_f_Sigma 5000*3600 0.0085        $ KTH exp. from meeting in Essen
```

```
add-table-entry 650C_f_Sigma 10000*3600 0.015       $ KTH exp. from meeting in Essen

$ exp. results for aged specimen at 750°C
$ Mean Radius:
create-global-table 750C_r_Sigma                    $ new table for exp. data
add-table-entry 750C_r_Sigma 1000*3600 865e-09      $ KTH exp. SEM data from table6
add-table-entry 750C_r_Sigma 3000*3600 1860e-09     $ KTH exp. SEM data from table6
add-table-entry 750C_r_Sigma 10000*3600 3545e-09    $ KTH exp. SEM data from table6

create-global-table 750C_r_M23C6                    $ new table for exp. data
add-table-entry 750C_r_M23C6 1000*3600 310e-09      $ KTH exp. SEM data from table6
add-table-entry 750C_r_M23C6 3000*3600 990e-09      $ KTH exp. SEM data from table6
add-table-entry 750C_r_M23C6 10000*3600 1060e-09    $ KTH exp. SEM data from table6

$ Phase fraction:
create-global-table 750C_f_M23C6                    $ new table for exp. data
add-table-entry 750C_f_M23C6 1000*3600 0.007        $ KTH exp. from meeting in Essen
add-table-entry 750C_f_M23C6 5000*3600 0.02         $ KTH exp. from meeting in Essen
add-table-entry 750C_f_M23C6 10000*3600 0.023       $ KTH exp. from meeting in Essen

create-global-table 750C_f_Sigma                    $ new table for exp. data
add-table-entry 750C_f_Sigma 1000*3600 0.01         $ KTH exp. from meeting in Essen
add-table-entry 750C_f_Sigma 5000*3600 0.018        $ KTH exp. from meeting in Essen
add-table-entry 750C_f_Sigma 10000*3600 0.023       $ KTH exp. from meeting in Essen

$ Wp% of Ni, Cr, Fe and Nb in precipitates at 650°C
$ Data is from paper "Long-term creep properties and microstructure of Super304H,
$ TP347HFG and HR3C for advanced USC boilers"
create-global-table 650C_wp_Ni               $ new table for exp. data
add-table-entry 650C_wp_Ni 0.01*3600 0       $ Ni content from paper in wp%
add-table-entry 650C_wp_Ni 300*3600 0        $ Ni content from paper in wp%
add-table-entry 650C_wp_Ni 1000*3600 0.05    $ Ni content from paper in wp%
add-table-entry 650C_wp_Ni 3000*3600 0.1     $ Ni content from paper in wp%
add-table-entry 650C_wp_Ni 10000*3600 0.15   $ Ni content from paper in wp%

create-global-table 650C_wp_Cr               $ new table for exp. data
add-table-entry 650C_wp_Cr 0.01*3600 0.14    $ Cr content from paper in wp%
add-table-entry 650C_wp_Cr 300*3600 0.45     $ Cr content from paper in wp%
add-table-entry 650C_wp_Cr 1000*3600 0.75    $ Cr content from paper in wp%
add-table-entry 650C_wp_Cr 3000*3600 0.97    $ Cr content from paper in wp%
add-table-entry 650C_wp_Cr 10000*3600 1.25   $ Cr content from paper in wp%

create-global-table 650C_wp_Fe               $ new table for exp. data
add-table-entry 650C_wp_Fe 0.01*3600 0.02    $ Fe content from paper in wp%
add-table-entry 650C_wp_Fe 300*3600 0.12     $ Fe content from paper in wp%
add-table-entry 650C_wp_Fe 1000*3600 0.11    $ Fe content from paper in wp%
add-table-entry 650C_wp_Fe 3000*3600 0.1     $ Fe content from paper in wp%
add-table-entry 650C_wp_Fe 10000*3600 0.14   $ Fe content from paper in wp%

create-global-table 650C_wp_Nb               $ new table for exp. data
add-table-entry 650C_wp_Nb 0.01*3600 0.25    $ Nb content from paper in wp%
add-table-entry 650C_wp_Nb 300*3600 0.28     $ Nb content from paper in wp%
add-table-entry 650C_wp_Nb 1000*3600 0.32    $ Nb content from paper in wp%
add-table-entry 650C_wp_Nb 3000*3600 0.42    $ Nb content from paper in wp%
add-table-entry 650C_wp_Nb 10000*3600 0.48   $ Nb content from paper in wp%

$ Wp% of Ni, Cr, Fe and Nb in precipitates at 750°C
$ Data is from paper "Long-term creep properties and microstructure of Super304H,
$ TP347HFG and HR3C for advanced USC boilers"
create-global-table 750C_wp_Ni               $ new table for exp. data
add-table-entry 750C_wp_Ni 0.01*3600 0       $ Ni content from paper in wp%
add-table-entry 750C_wp_Ni 300*3600 0.025    $ Ni content from paper in wp%
add-table-entry 750C_wp_Ni 1000*3600 0.025   $ Ni content from paper in wp%
add-table-entry 750C_wp_Ni 3000*3600 0.05    $ Ni content from paper in wp%
add-table-entry 750C_wp_Ni 10000*3600 0.1    $ Ni content from paper in wp%
```

```
create-global-table 750C_wp_Cr              $ new table for exp. data
add-table-entry 750C_wp_Cr 0.01*3600 0.14   $ Cr content from paper in wp%
add-table-entry 750C_wp_Cr 300*3600 1       $ Cr content from paper in wp%
add-table-entry 750C_wp_Cr 1000*3600 1.08   $ Cr content from paper in wp%
add-table-entry 750C_wp_Cr 3000*3600 1.12   $ Cr content from paper in wp%
add-table-entry 750C_wp_Cr 10000*3600 1     $ Cr content from paper in wp%

create-global-table 750C_wp_Fe              $ new table for exp. data
add-table-entry 750C_wp_Fe 0.01*3600 0.02   $ Fe content from paper in wp%
add-table-entry 750C_wp_Fe 300*3600 0.12    $ Fe content from paper in wp%
add-table-entry 750C_wp_Fe 1000*3600 0.11   $ Fe content from paper in wp%
add-table-entry 750C_wp_Fe 3000*3600 0.1    $ Fe content from paper in wp%
add-table-entry 750C_wp_Fe 10000*3600 0.14  $ Fe content from paper in wp%

create-global-table 750C_wp_Nb              $ new table for exp. data
add-table-entry 750C_wp_Nb 0.01*3600 0.25   $ Nb content from paper in wp%
add-table-entry 750C_wp_Nb 300*3600 0.45    $ Nb content from paper in wp%
add-table-entry 750C_wp_Nb 1000*3600 0.46   $ Nb content from paper in wp%
add-table-entry 750C_wp_Nb 3000*3600 0.47   $ Nb content from paper in wp%
add-table-entry 750C_wp_Nb 10000*3600 0.45  $ Nb content from paper in wp%


$ *************************************************************************************
$                         PRECIPITATION DOMAINS, PRECIPITATES
$ *************************************************************************************

$ ----------------------------- PRECIPITATION DOMAIN ---------------------------------

create-precipitation-domain austenite                $ precipitation domain
set-precipitation-parameter austenite x fcc_a1       $ matrix phase of domain austenite
set-precipitation-parameter austenite t d e 1e12     $ dislocation density (=1e12 m^-2)
set-precipitation-parameter austenite t g 22e-6      $ grain size (22µm)
set-precipitation-parameter austenite t s 2e-6       $ subgain size
$ diffusion function for grain boundaries from MaTcalc 5.61 (rel 0.022)
set-precipitation-parameter austenite S G S Y 7.9e-1*exp(141000/(R*T))  $ substitional
set-precipitation-parameter austenite S G i y 1.5e0*exp(33600/(R*T))     $ interstitial

$ diffusion function for dislocations from MaTcalc 5.61 (rel 0.022)
set-precipitation-parameter austenite S d S Y 6.4e-2*exp(119000/(R*T))  $ substitional
set-precipitation-parameter austenite S d i y 1.0e0*exp(29200/(R*T))     $ interstitial

$ ------------------------ PRECIPITATE PHASES IN AUSTENITE ----------------------------

create-new-phase m23c6 p M23C6.gb                        $ new precipitate phase M23C6
set-precipitation-parameter m23c6_p0 n s g               $ nucl. sites grain bound.
set-precipitation-parameter m23c6_p0 n p y austenite     $ restrict nucleation to aust.
set-precipitation-parameter m23c6_p0 h y 3               $ precipitates shape factor

create-new-phase m23c6 p M23C6.gi                        $ new precipitate phase M23C6
set-precipitation-parameter m23c6_p1 n s x               $ nucl. sites subgrain corner
set-precipitation-parameter m23c6_p1 n p y austenite     $ restrict nucleation to aust.
set-precipitation-parameter m23c6_p1 h y 3               $ precipitates shape factor

create-new-phase sigma p Sigma                           $ new precipitate phase Sigma
set-precipitation-parameter sigma_p0 n s c               $ nucl. sites grain corner
set-precipitation-parameter sigma_p0 n p y austenite     $ restrict nucleation to aust.
set-precipitation-parameter sigma_p0 s m s 3             $ matrix diffusion enhancement
create-global-table ciesi                                $ create table interfacial cor.
add-table-entry ciesi 200 1                              $ no interfacial cor. at 200°C
add-table-entry ciesi 650 1                              $ no interfacial cor. at 200°C
add-table-entry ciesi 700 0.80                           $ interfacial cor. at 700°C
add-table-entry ciesi 750 0.45                           $ interfacial cor. at 750°C
add-table-entry ciesi 850 0.45                           $ interfacial cor. at 850°C
set-precipitation-parameter sigma_p0 i n cie$sigma*ciesi(t$c) $ interfacial cor. is on
```

```
create-new-phase nbcn p Nb(C,N)(prim)                   $ new precipitate phase Nb(C,N)
set-precipitation-parameter nbcn_p0 n s n               $ no nucl. sites for prim. prec.

create-new-phase nbcn p Nb(C,N)                         $ create new precipitate phase
set-precipitation-parameter nbcn_p1 n s d               $ nucl. sites dislocations
set-precipitation-parameter nbcn_p1 n p y austenite     $ restrict nucleation to aust.

create-new-phase zet p Z(prim)                          $ new precipitate phase prim. Z
set-precipitation-parameter zet_p0 n s n                $ no nucl. sites for prim. prec.

create-new-phase zet p Z                                $ new precipitate phase Z
set-precipitation-parameter zet_p1 n s d                $ nucl. sites dislocations
set-precipitation-parameter zet_p1 n p y austenite      $ restrict nucleation to aust.
set-precipitation-parameter zet_p1 h y 3                $ precipitates shape factor

create-new-phase cr3ni2sin p Eta                        $ new precipitate phase Eta
set-precipitation-parameter cr3ni2sin_p0 n s g          $ nucl. sites grain boundary
set-precipitation-parameter cr3ni2sin_p0 n p y austenite$ restrict nucleation to aust.
create-new-phase g_phase p G                             $ new precipitate phase G
set-precipitation-parameter g_phase_p0 n s g             $ nucl. sites grain boundary
set-precipitation-parameter g_phase_p0 n p y austenite   $ restrict nucleation to aust.

$ Import of primary precipitates: Z-phase and Nb(C,N)
if (comp==1)
    import-precipitate-dist zet_p0 Z_prim_1_25Cr20NiNbN.txt
    import-precipitate-dist nbcn_p0 NbCN_prim_1_25Cr20NiNbN.txt
elseif (comp==119)|(comp==120)
    import-precipitate-dist zet_p0 Z_prim_119_25Cr20NiNbN.txt
endif


$ **************************************************************************************
$                             OUTPUT WINDOWS, PLOTS, ETC.
$ **************************************************************************************

$ ------------------------------ Solution Plot ----------------------------------------

$ create one frame displaying the solution part, with exp data and log x-scale
new-gui-window p1                            $ generate new plot: Solution plot

$ Default plot settings
set-gui-window-property . x stepvalue        $ default x-axis variable (time)
set-gui-window-property . s u y              $ use default x-axis for all plots: yes
set-gui-window-property . s y lin            $ default x-axis type linear
set-gui-window-property . s t time / min     $ default x-axis title
set-gui-window-property . s f 1/60           $ scaling factor for [min]
set-gui-window-property . n 2                $ 2 plot columns

$ Plot settings for TEMPERATURE
set-plot-option . s n b t$c                  $ add series: temperature
set-plot-option . s m -1 t$c T               $ define series legend
set-plot-option . a y 1 t temperature / °C   $ y-axis title
set-plot-option . l n                        $ no legend

$ Plot settings for PHASE FRACTION
create-new-plot x .                          $ create new plot: phase fractions
set-plot-option . l a y                      $ replace variable names by kinetic alias
set-plot-option . s n b f_prec$*             $ add all series: phase fractions of prec.
set-plot-option . a y 1 t phase fraction / % $ change y-axis title
set-plot-option . a y 1 f 1*100              $ scaling factor for [%]
set-plot-option . a y 1 y log                $ use logarithmic scale for y-axis
set-plot-option . a y 1 s 1e-8..             $ scale the y-axis from 1e-8..

$ Plot settings plot for MEAN RADII
create-new-plot x .                          $ create new plot: mean radii
```

```
set-plot-option . l a y                      $ replace variable names by kinetic alias
set-plot-option . s n b r_mean$*             $ add all series: mean radii of prec.
set-plot-option . a y 1 t mean radius / nm   $ change y-axis title
set-plot-option . a y 1 y log                $ use logarithmic scale for y-axis
set-plot-option . a y 1 f 1e9                $ scaling factor is 1e9 for [nm]

$ Plot settings for NUMBER DENSITIES
create-new-plot x .                          $ create new plot: number densities
set-plot-option . l a y                      $ replace variable names by kinetic alias
set-plot-option . s n b num_part$*           $ add all series: number densities of prec.
set-plot-option . a y 1 t number density / m<sup>-3</sup>   $ change y-axis title
set-plot-option . a y 1 y log                $ use logarithmic scale for y-axis
set-plot-option . a y 1 s 1..                $ scale the y-axis from 1..

move-gui-window . 20 20 900 950              $ move window to new position and resize
update-gui-window .                          $ update the GUI window

move-gui-window . hide                       $ hide plote


$ --------------------------------- Service Plot --------------------------------------

$ create one frame displaying the service part, with exp data and log x-scale
new-gui-window p1                            $ generate new plot: Service Plot

$ Default plot settings
set-gui-window-property . x stepvalue        $ default x-axis variable (time)
set-gui-window-property . s u y              $ use default x-axis for all plots: yes
set-gui-window-property . s y log            $ default x-axis type logarithmic
set-gui-window-property . s t time / h       $ default x-axis title
set-gui-window-property . s f 1/3600         $ scaling factor for [h]
set-gui-window-property . n 2                $ 2 plot columns
set-gui-window-property . s s 0.001..        $ scale the time-axis (x) from 0.001..

$ Plot settings for TEMPERATURE
set-plot-option . s n b t$c                  $ add series: temperature
set-plot-option . s m -1 t$c T               $ define series legend
set-plot-option . a y 1 t temperature / °C   $ y-axis title
set-plot-option . l n                        $ no legend

$ Plot settings for PHASE FRACTION
create-new-plot x .                          $ create new plot: phase fractions
set-plot-option . l a y                      $ replace variable names by kinetic alias
set-plot-option . s n b f_prec$*             $ add all series: phase fractions of prec.
set-plot-option . a y 1 t phase fraction / % $ change y-axis title
set-plot-option . a y 1 f 1*100              $ scaling factor for [%]
set-plot-option . a y 1 y log                $ use logarithmic scale for y-axis
set-plot-option . a y 1 s 1e-4..             $ scale the y-axis from 1e-4..
if(comp==1)
    if (T_s==650)
        set-plot-option . s n t 650C_f_M23C6        $ add experimental data to plot
        set-plot-option . s m -1 650C_f_M23C6 M23C6 $ rename exp. data
        set-plot-option . s n t 650C_f_Sigma        $ add experimental data to plot
        set-plot-option . s m -1 650C_f_Sigma Sigma  $ rename exp. data
    elseif (T_s==750)
        set-plot-option . s n t 750C_f_M23C6         $ add experimental data to plot
        set-plot-option . s m -1 750C_f_M23C6 M23C6  $ rename exp. data
        set-plot-option . s n t 750C_f_Sigma         $ add experimental data to plot
        set-plot-option . s m -1 750C_f_Sigma Sigma  $ rename exp. data
    endif
endif

$ Plot settings plot for MEAN RADII
create-new-plot x .                          $ create new plot: mean radii
set-plot-option . l a y                      $ replace variable names by kinetic alias
set-plot-option . s n b r_mean$*             $ add all series: mean radii of prec.
```

```
set-plot-option . a y 1 t mean radius / nm   $ change y-axis title
set-plot-option . a y 1 y log                $ use logarithmic scale for y-axis
set-plot-option . a y 1 f 1e9                $ scaling factor is 1e9 for [nm]
set-plot-option . a y 1 s 10..               $ scale the y-axis from 10nm..
if (comp==1)
    if (T_s==750)
        set-plot-option . s n t 750C_r_Sigma            $ add exp. data to plot
        set-plot-option . s m -1 750C_r_Sigma Sigma     $ rename exp. data
        set-plot-option . s n t 750C_r_M23C6            $ add exp. data to plot
        set-plot-option . s m -1 750C_r_M23C6 M23C6     $ rename exp. data
    elseif (T_s==650)
        set-plot-option . s n t 650C_r_Sigma            $ add exp. data to plot
        set-plot-option . s m -1 650C_r_Sigma Sigma     $ rename exp. data
        set-plot-option . s n t 650C_r_M23C6            $ add exp. data to plot
        set-plot-option . s m -1 650C_r_M23C6 M23C6     $ rename exp. data
    endif
endif

$ Plot settings for NUMBER DENSITIES
create-new-plot x .                     $ create new plot: number densities
set-plot-option . l a y                 $ replace all variable names by kinetic alias
set-plot-option . s n b num_part$*      $ add all series: number densities of prec.
set-plot-option . a y 1 t number density / m<sup>-3</sup>  $ change y-axis title
set-plot-option . a y 1 y log           $ use logarithmic scale for y-axis
set-plot-option . a y 1 s 1..           $ scale the y-axis from 1..

move-gui-window . 20 20 900 950         $ move window to new position and resize
update-gui-window .                     $ update the GUI window

move-gui-window . hide                  $ hide plote

$ ------------------------------- Compositions Plot -----------------------------------

$ create one frame displaying the service part, with exp data and log x-scale
new-gui-window p1                       $ generate new plot: Composition plot

$ Default plot settings
set-gui-window-property . x stepvalue   $ default x-axis variable (time)
set-gui-window-property . s u y         $ use default x-axis for all plots: yes
set-gui-window-property . s y log       $ default x-axis type linear
set-gui-window-property . s t time / h  $ default x-axis title
set-gui-window-property . s f 1/3600    $ scaling factor for [h]
set-gui-window-property . n 2           $ 2 plot columns
set-gui-window-property . s s 0.001..   $ scaling from 0.001..

$ Plot settings for Ni content
set-plot-option . a y 1 t Content of Ni / wp%    $ change y-axis title
set-plot-option . a y 1 y lin                    $ use linear scale for y-axis
set-plot-option . s n b x$m23c6_p0$ni$wp*f$m23c6_p0$wp/100  $ content of Ni in m23c6.gb
set-plot-option . s m -1 x$m23c6_p0$ni$wp*f$m23c6_p0$wp/100 M23C6.gb    $rename series
set-plot-option . s n b x$m23c6_p1$ni$wp*f$m23c6_p1$wp/100  $ content of Ni in m23c6.gi
set-plot-option . s m -1 x$m23c6_p1$ni$wp*f$m23c6_p1$wp/100 M23C6.gi    $rename series
set-plot-option . s n b x$sigma_p0$ni$wp*f$sigma_p0$wp/100  $ content of Ni in sigma
set-plot-option . s m -1 x$sigma_p0$ni$wp*f$sigma_p0$wp/100 Sigma       $rename series
set-plot-option . s n b x$cr3ni2sin_p0$ni$wp*f$cr3ni2sin_p0$wp/100 $content of Ni in Eta
set-plot-option . s m -1 x$cr3ni2sin_p0$ni$wp*f$cr3ni2sin_p0$wp/100 Eta $rename series
set-plot-option . s n b x$g_phase_p0$ni$wp*f$g_phase_p0$wp/100  $ content of Ni in G
set-plot-option . s m -1 x$g_phase_p0$ni$wp*f$g_phase_p0$wp/100 G       $rename series
set-plot-option . s n b x$m23c6_p0$ni$wp*f$m23c6_p0$wp/100+x$m23c6_p1$ni$wp*f$m23c6_p1$w
set-plot-option . s m -1 x$m23c6_p0$ni$wp*f$m23c6_p0$wp/100+x$m23c6_p1$ni$wp*f$m23c6_p1$
if (comp==1)
    if (T_s==750)
        set-plot-option . s n t 750C_wp_Ni      $ add exp. data to plot
        set-plot-option . s m -1 750C_wp_Ni Ni  $ rename exp. data
    elseif (T_s==650)
        set-plot-option . s n t 650C_wp_Ni      $ add exp. data to plot
```

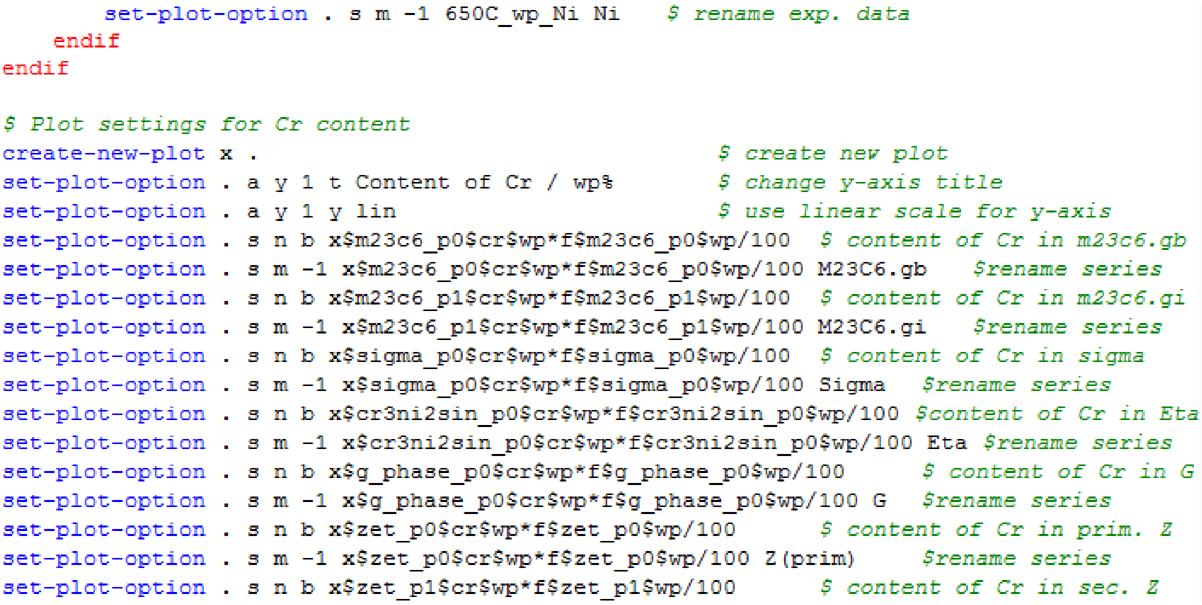

```
        set-plot-option . s m -1 650C_wp_Ni Ni    $ rename exp. data
    endif
endif

$ Plot settings for Cr content
create-new-plot x .                                  $ create new plot
set-plot-option . a y 1 t Content of Cr / wp%        $ change y-axis title
set-plot-option . a y 1 y lin                        $ use linear scale for y-axis
set-plot-option . s n b x$m23c6_p0$cr$wp*f$m23c6_p0$wp/100  $ content of Cr in m23c6.gb
set-plot-option . s m -1 x$m23c6_p0$cr$wp*f$m23c6_p0$wp/100 M23C6.gb    $rename series
set-plot-option . s n b x$m23c6_p1$cr$wp*f$m23c6_p1$wp/100  $ content of Cr in m23c6.gi
set-plot-option . s m -1 x$m23c6_p1$cr$wp*f$m23c6_p1$wp/100 M23C6.gi    $rename series
set-plot-option . s n b x$sigma_p0$cr$wp*f$sigma_p0$wp/100  $ content of Cr in sigma
set-plot-option . s m -1 x$sigma_p0$cr$wp*f$sigma_p0$wp/100 Sigma   $rename series
set-plot-option . s n b x$cr3ni2sin_p0$cr$wp*f$cr3ni2sin_p0$wp/100 $content of Cr in Eta
set-plot-option . s m -1 x$cr3ni2sin_p0$cr$wp*f$cr3ni2sin_p0$wp/100 Eta $rename series
set-plot-option . s n b x$g_phase_p0$cr$wp*f$g_phase_p0$wp/100      $ content of Cr in G
set-plot-option . s m -1 x$g_phase_p0$cr$wp*f$g_phase_p0$wp/100 G   $rename series
set-plot-option . s n b x$zet_p0$cr$wp*f$zet_p0$wp/100      $ content of Cr in prim. Z
set-plot-option . s m -1 x$zet_p0$cr$wp*f$zet_p0$wp/100 Z(prim)     $rename series
set-plot-option . s n b x$zet_p1$cr$wp*f$zet_p1$wp/100      $ content of Cr in sec. Z
```

```
set-plot-option . s m -1 x$zet_p1$cr$wp*f$zet_p1$wp/100 Z    $ rename series
set-plot-option . s n b x$m23c6_p0$cr$wp*f$m23c6_p0$wp/100+x$m23c6_p1$cr$wp*f$m23c6_p1$
set-plot-option . s m -1 x$m23c6_p0$cr$wp*f$m23c6_p0$wp/100+x$m23c6_p1$cr$wp*f$m23c6_p1
if (comp==1)
    if (T_s==750)
        set-plot-option . s n t 750C_wp_Cr       $ add exp. data to plot
        set-plot-option . s m -1 750C_wp_Cr Cr   $ rename exp. data
    elseif (T_s==650)
        set-plot-option . s n t 650C_wp_Cr       $ add exp. data to plot
        set-plot-option . s m -1 650C_wp_Cr Cr   $ rename exp. data
    endif
endif

$ Plot settings for Fe content
create-new-plot x .                                  $ create new plot
set-plot-option . a y 1 t Content of Fe / wp%        $ change y-axis title
set-plot-option . a y 1 y lin                        $ use linear scale for y-axis
set-plot-option . s n b x$m23c6_p0$fe$wp*f$m23c6_p0$wp/100  $ Fe in m23c6.gb
set-plot-option . s m -1 x$m23c6_p0$fe$wp*f$m23c6_p0$wp/100 M23C6.gb    $rename series
set-plot-option . s n b x$m23c6_p1$fe$wp*f$m23c6_p1$wp/100  $ content of Fe in m23c6.gi
set-plot-option . s m -1 x$m23c6_p1$fe$wp*f$m23c6_p1$wp/100 M23C6.gi    $rename series
set-plot-option . s n b x$sigma_p0$fe$wp*f$sigma_p0$wp/100      $ Fe in sigma
set-plot-option . s m -1 x$sigma_p0$fe$wp*f$sigma_p0$wp/100 Sigma   $rename series
set-plot-option . s n b x$cr3ni2sin_p0$fe$wp*f$cr3ni2sin_p0$wp/100 $ Fe in Eta
set-plot-option . s m -1 x$cr3ni2sin_p0$fe$wp*f$cr3ni2sin_p0$wp/100 Eta$rename series
set-plot-option . s n b x$g_phase_p0$fe$wp*f$g_phase_p0$wp/100 $ Fe in G
set-plot-option . s m -1 x$g_phase_p0$fe$wp*f$g_phase_p0$wp/100 G   $rename series
set-plot-option . s n b x$zet_p0$fe$wp*f$zet_p0$wp/100      $ Fe in prim. Z
set-plot-option . s m -1 x$zet_p0$fe$wp*f$zet_p0$wp/100 Z(prim) $rename series
set-plot-option . s n b x$zet_p1$fe$wp*f$zet_p1$wp/100      $ Fe in sec. Z
set-plot-option . s m -1 x$zet_p1$fe$wp*f$zet_p1$wp/100 Z   $rename series
set-plot-option . s n b x$m23c6_p0$fe$wp*f$m23c6_p0$wp/100+x$m23c6_p1$fe$wp*f$m23c6_p1$
set-plot-option . s m -1 x$m23c6_p0$fe$wp*f$m23c6_p0$wp/100+x$m23c6_p1$fe$wp*f$m23c6_p1
if (comp==1)
    if (T_s==750)
        set-plot-option . s n t 750C_wp_Fe       $ add exp. data to plot
        set-plot-option . s m -1 750C_wp_Fe Fe   $ rename exp. data
    elseif (T_s==650)
        set-plot-option . s n t 650C_wp_Fe       $ add exp. data to plot
        set-plot-option . s m -1 650C_wp_Fe Fe   $ rename exp. data
    endif
endif

$ Plot settings for Nb content
create-new-plot x .                                     $ create new plot
```

```
set-plot-option . a y 1 t Content of Nb / wp%           $ change y-axis title
set-plot-option . a y 1 y lin                           $ use linear scale for y-axis
set-plot-option . s n b x$g_phase_p0$nb$wp*f$g_phase_p0$wp/100  $ Nb in G phase
set-plot-option . s m -1 x$g_phase_p0$nb$wp*f$g_phase_p0$wp/100 G  $rename series
set-plot-option . s n b x$zet_p0$nb$wp*f$zet_p0$wp/100          $ Nb in prim. Z
set-plot-option . s m -1 x$zet_p0$nb$wp*f$zet_p0$wp/100 Z(prim) $ rename series
set-plot-option . s n b x$zet_p1$nb$wp*f$zet_p1$wp/100          $ Nb in sec. Z
set-plot-option . s m -1 x$zet_p1$nb$wp*f$zet_p1$wp/100 Z       $ rename series
set-plot-option . s n b x$nbcn_p0$nb$wp*f$nbcn_p0$wp/100    $ Nb in prim. NbCN
set-plot-option . s m -1 x$nbcn_p0$nb$wp*f$nbcn_p0$wp/100 NbCN(prim)    $rename series
set-plot-option . s n b x$nbcn_p1$nb$wp*f$nbcn_p1$wp/100    $ Nb in sec. NbCN
set-plot-option . s m -1 x$nbcn_p1$nb$wp*f$nbcn_p1$wp/100 NbCN  $rename series
set-plot-option . s n b x$g_phase_p0$nb$wp*f$g_phase_p0$wp/100+x$zet_p0$nb$wp*f$zet_p0$
set-plot-option . s m -1 x$g_phase_p0$nb$wp*f$g_phase_p0$wp/100+x$zet_p0$nb$wp*f$zet_p0
if (comp==1)
    if (T_s==750)
        set-plot-option . s n t 750C_wp_Nb       $ add exp. data to plot
        set-plot-option . s m -1 750C_wp_Nb Nb   $ rename exp. data
    elseif (T_s==650)
        set-plot-option . s n t 650C_wp_Nb       $ add exp. data to plot
        set-plot-option . s m -1 650C_wp_Nb Nb   $ rename exp. data
    endif
endif

$ Plot settings for C content
create-new-plot x .                                     $ create new plot
set-plot-option . a y 1 t Content of C / wp%            $ change y-axis title
set-plot-option . a y 1 y lin                           $ use linear scale for y-axis
set-plot-option . s n b x$fcc_a1$c$wp*f$fcc_a1$wp/100   $ content of C in Matrix phase
set-plot-option . s m -1 x$fcc_a1$c$wp*f$fcc_a1$wp/100 Matrix   $rename series
set-plot-option . s n b x$m23c6_p0$c$wp*f$m23c6_p0$wp/100 $ content of C in M23C6.gb
set-plot-option . s m -1 x$m23c6_p0$c$wp*f$m23c6_p0$wp/100 M23C6.gb $rename series
set-plot-option . s n b x$m23c6_p1$c$wp*f$m23c6_p1$wp/100   $ content of C in M23C6.gi
set-plot-option . s m -1 x$m23c6_p1$c$wp*f$m23c6_p1$wp/100 M23C6.gi $rename series
set-plot-option . s n b x$nbcn_p0$c$wp*f$nbcn_p0$wp/100 $ content of C in prim. NbCN
set-plot-option . s m -1 x$nbcn_p0$c$wp*f$nbcn_p0$wp/100 NbCN(prim) $rename series
set-plot-option . s n b x$nbcn_p1$c$wp*f$nbcn_p1$wp/100     $ content of C in sec. NbCN
set-plot-option . s m -1 x$nbcn_p1$c$wp*f$nbcn_p1$wp/100 NbCN   $rename series
set-plot-option . s n b x$cr3ni2sin_p0$c$wp*f$cr3ni2sin_p0$wp/100 $ content of C in Eta
set-plot-option . s m -1 x$cr3ni2sin_p0$c$wp*f$cr3ni2sin_p0$wp/100 Eta  $rename series

$ Plot settings for N content
create-new-plot x .                                     $ create new plot
set-plot-option . a y 1 t Content of N / wp%            $ change y-axis title
set-plot-option . a y 1 y lin                           $ use linear scale for y-axis
set-plot-option . s n b x$fcc_a1$n$wp*f$fcc_a1$wp/100   $ content of N in Matrix phase
set-plot-option . s m -1 x$fcc_a1$n$wp*f$fcc_a1$wp/100 Matrix   $rename series
set-plot-option . s n b x$zet_p0$n$wp*f$zet_p0$wp/100       $ content of N in prim. Z
set-plot-option . s m -1 x$zet_p0$n$wp*f$zet_p0$wp/100 Z(prim)  $ rename series
set-plot-option . s n b x$zet_p1$n$wp*f$zet_p1$wp/100   $ content of N in sec. Z
set-plot-option . s m -1 x$zet_p1$n$wp*f$zet_p1$wp/100 Z    $ rename series
set-plot-option . s n b x$nbcn_p0$n$wp*f$nbcn_p0$wp/100 $ content of N in prim. NbCN
set-plot-option . s m -1 x$nbcn_p0$n$wp*f$nbcn_p0$wp/100 NbCN(prim) $rename series
set-plot-option . s n b x$nbcn_p1$n$wp*f$nbcn_p1$wp/100     $ content of N in sec. NbCN
set-plot-option . s m -1 x$nbcn_p1$n$wp*f$nbcn_p1$wp/100 NbCN   $rename series
set-plot-option . s n b x$cr3ni2sin_p0$n$wp*f$cr3ni2sin_p0$wp/100   $ content of N in Et
set-plot-option . s m -1 x$cr3ni2sin_p0$n$wp*f$cr3ni2sin_p0$wp/100 Eta  $rename series


move-gui-window . 40 30 900 1050     $ move window to new position and resize
update-gui-window .                  $ update the GUI window

move-gui-window . hide               $ hide plote
```

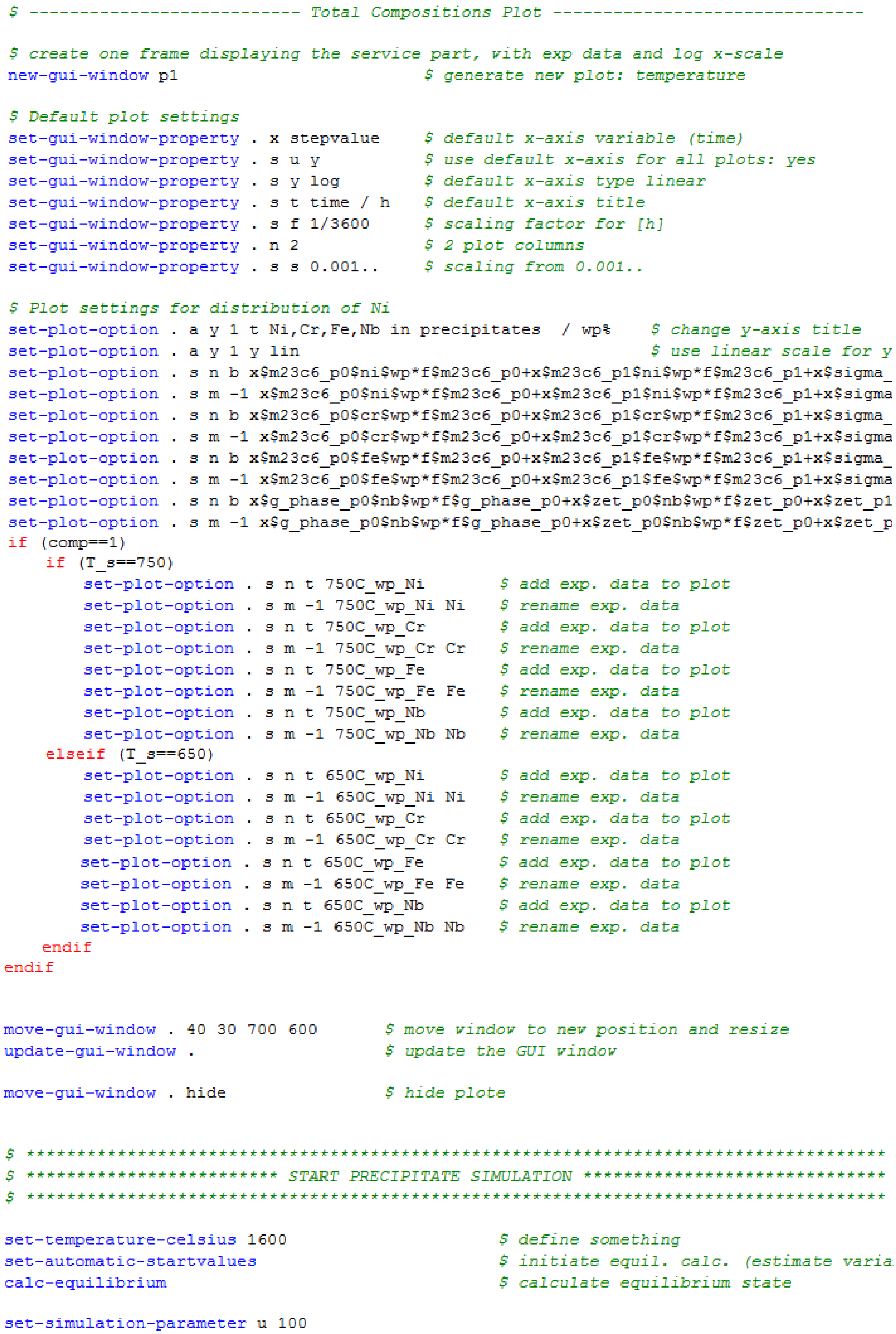

```
$ --------------------------- Total Compositions Plot -------------------------------

$ create one frame displaying the service part, with exp data and log x-scale
new-gui-window p1                        $ generate new plot: temperature

$ Default plot settings
set-gui-window-property . x stepvalue    $ default x-axis variable (time)
set-gui-window-property . s u y          $ use default x-axis for all plots: yes
set-gui-window-property . s y log        $ default x-axis type linear
set-gui-window-property . s t time / h   $ default x-axis title
set-gui-window-property . s f 1/3600     $ scaling factor for [h]
set-gui-window-property . n 2            $ 2 plot columns
set-gui-window-property . s s 0.001..    $ scaling from 0.001..

$ Plot settings for distribution of Ni
set-plot-option . a y 1 t Ni,Cr,Fe,Nb in precipitates  / wp%    $ change y-axis title
set-plot-option . a y 1 y lin                                   $ use linear scale for y
set-plot-option . s n b x$m23c6_p0$ni$wp*f$m23c6_p0+x$m23c6_p1$ni$wp*f$m23c6_p1+x$sigma_
set-plot-option . s m -1 x$m23c6_p0$ni$wp*f$m23c6_p0+x$m23c6_p1$ni$wp*f$m23c6_p1+x$sigma
set-plot-option . s n b x$m23c6_p0$cr$wp*f$m23c6_p0+x$m23c6_p1$cr$wp*f$m23c6_p1+x$sigma_
set-plot-option . s m -1 x$m23c6_p0$cr$wp*f$m23c6_p0+x$m23c6_p1$cr$wp*f$m23c6_p1+x$sigma
set-plot-option . s n b x$m23c6_p0$fe$wp*f$m23c6_p0+x$m23c6_p1$fe$wp*f$m23c6_p1+x$sigma_
set-plot-option . s m -1 x$m23c6_p0$fe$wp*f$m23c6_p0+x$m23c6_p1$fe$wp*f$m23c6_p1+x$sigma
set-plot-option . s n b x$g_phase_p0$nb$wp*f$g_phase_p0+x$zet_p0$nb$wp*f$zet_p0+x$zet_p1
set-plot-option . s m -1 x$g_phase_p0$nb$wp*f$g_phase_p0+x$zet_p0$nb$wp*f$zet_p0+x$zet_p
if (comp==1)
    if (T_s==750)
        set-plot-option . s n t 750C_wp_Ni      $ add exp. data to plot
        set-plot-option . s m -1 750C_wp_Ni Ni  $ rename exp. data
        set-plot-option . s n t 750C_wp_Cr      $ add exp. data to plot
        set-plot-option . s m -1 750C_wp_Cr Cr  $ rename exp. data
        set-plot-option . s n t 750C_wp_Fe      $ add exp. data to plot
        set-plot-option . s m -1 750C_wp_Fe Fe  $ rename exp. data
        set-plot-option . s n t 750C_wp_Nb      $ add exp. data to plot
        set-plot-option . s m -1 750C_wp_Nb Nb  $ rename exp. data
    elseif (T_s==650)
        set-plot-option . s n t 650C_wp_Ni      $ add exp. data to plot
        set-plot-option . s m -1 650C_wp_Ni Ni  $ rename exp. data
        set-plot-option . s n t 650C_wp_Cr      $ add exp. data to plot
        set-plot-option . s m -1 650C_wp_Cr Cr  $ rename exp. data
        set-plot-option . s n t 650C_wp_Fe      $ add exp. data to plot
        set-plot-option . s m -1 650C_wp_Fe Fe  $ rename exp. data
        set-plot-option . s n t 650C_wp_Nb      $ add exp. data to plot
        set-plot-option . s m -1 650C_wp_Nb Nb  $ rename exp. data
    endif
endif


move-gui-window . 40 30 700 600       $ move window to new position and resize
update-gui-window .                   $ update the GUI window

move-gui-window . hide                $ hide plote


$ *************************************************************************************
$ ************************* START PRECIPITATE SIMULATION ******************************
$ *************************************************************************************

set-temperature-celsius 1600                     $ define something
set-automatic-startvalues                        $ initiate equil. calc. (estimate varia
calc-equilibrium                                 $ calculate equilibrium state

set-simulation-parameter u 100
```

```
$ -------------------- START PRECIPITATE SIMULATION PART I-----------------------------

rename-current-buffer solution                   $ rename buffer for heat treatment
set-gui-window-property 3 b solution             $ attach to buffer window ID3

set-simulation-parameter t h solution 10         $ temp. profile from HT, max. T-step
set-simulation-parameter s n                     $ reset start condition for prec. sim.

move-gui-window 3 show                           $ bring plot to front

start-precipitate-simulation                     $ start precipitation simulation

move-gui-window 3 hide                           $ hide the solution annealing plot

$ save state after simulation. Is starting point for next simulation part II
create-calc-state after_solution

$ -------------------- START PRECIPITATE SIMULATION PART II----------------------------

create-calc-buffer service                       $ create buffer for HT
select-calc-buffer service                       $ select calc buffer
set-gui-window-property 4 b service              $ attach to buffer window ID4
set-gui-window-property 5 b service              $ attach to buffer window ID5
set-gui-window-property 6 b service              $ attach to buffer window ID6

set-simulation-parameter t h service 10          $ temp. profile from HT, max. T-step
set-simulation-parameter s l after_solution      $ solt. ann. start condition for prec.
move-gui-window 4 show                           $ bring plot to front

start-precipitate-simulation                     $ let's go with part II

$ save state after simulation.
create-calc-state after_service

update-gui-windows .


$ *************************************************************************************
$                          PRECIPITATE SIMULATION FINISHED
$ *************************************************************************************
```